Control Engineering Series 93

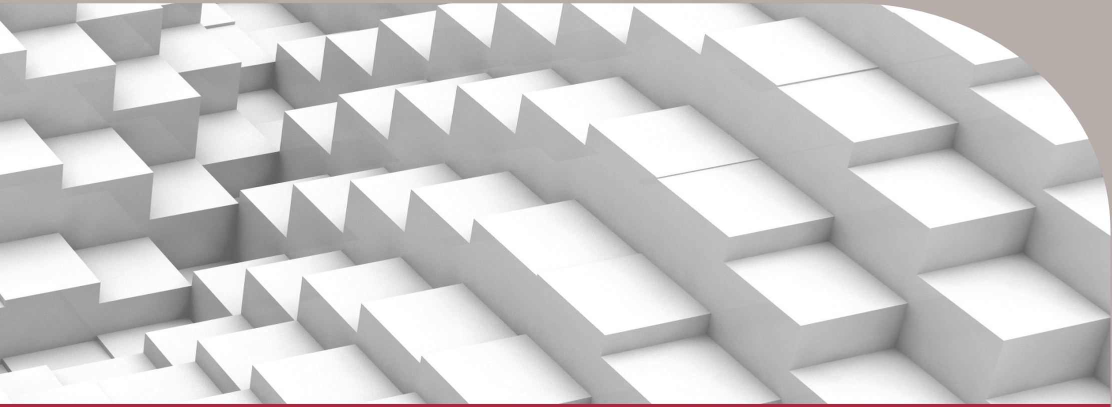

Design and Development of Multi-Lane Smart Electromechanical Actuators

Fawaz Yahya Annaz

IET CONTROL ENGINEERING SERIES 93

Design and Development of Multi-Lane Smart Electromechanical Actuators

Other volumes in this series:

Volume 8	**A history of control engineering, 1800–1930** S. Bennett
Volume 18	**Applied control theory, 2nd edition** J.R. Leigh
Volume 20	**Design of modern control systems** D.J. Bell, P.A. Cook and N. Munro (Editors)
Volume 28	**Robots and automated manufacture** J. Billingsley (Editor)
Volume 33	**Temperature measurement and control** J.R. Leigh
Volume 34	**Singular perturbation methodology in control systems** D.S. Naidu
Volume 35	**Implementation of self-tuning controllers** K. Warwick (Editor)
Volume 37	**Industrial digital control systems, 2nd edition** K. Warwick and D. Rees (Editors)
Volume 39	**Continuous time controller design** R. Balasubramanian
Volume 40	**Deterministic control of uncertain systems** A.S.I. Zinober (Editor)
Volume 41	**Computer control of real-time processes** S. Bennett and G.S. Virk (Editors)
Volume 42	**Digital signal processing: principles, devices and applications** N.B. Jones and J.D.McK. Watson (Editors)
Volume 44	**Knowledge-based systems for industrial control** J. McGhee, M.J. Grimble and A. Mowforth (Editors)
Volume 47	**A history of control engineering, 1930–1956** S. Bennett
Volume 49	**Polynomial methods in optimal control and filtering** K.J. Hunt (Editor)
Volume 50	**Programming industrial control systems using IEC 1131-3** R.W. Lewis
Volume 51	**Advanced robotics and intelligent machines** J.O. Gray and D.G. Caldwell (Editors)
Volume 52	**Adaptive prediction and predictive control** P.P. Kanjilal
Volume 53	**Neural network applications in control** G.W. Irwin, K. Warwick and K.J. Hunt (Editors)
Volume 54	**Control engineering solutions: a practical approach** P. Albertos, R. Strietzel and N. Mort (Editors)
Volume 55	**Genetic algorithms in engineering systems** A.M.S. Zalzala and P.J. Fleming (Editors)
Volume 56	**Symbolic methods in control system analysis and design** N. Munro (Editor)
Volume 57	**Flight control systems** R.W. Pratt (Editor)
Volume 58	**Power-plant control and instrumentation: the control of boilers and HRSG systems** D. Lindsley
Volume 59	**Modelling control systems using IEC 61499** R. Lewis
Volume 60	**People in control: human factors in control room design** J. Noyes and M. Bransby (Editors)
Volume 61	**Nonlinear predictive control: theory and practice** B. Kouvaritakis and M. Cannon (Editors)
Volume 62	**Active sound and vibration control** M.O. Tokhi and S.M. Veres
Volume 63	**Stepping motors, 4th edition** P.P. Acarnley
Volume 65	**Modelling and parameter estimation of dynamic systems** J.R. Raol, G. Girija and J. Singh
Volume 66	**Variable structure systems: from principles to implementation** A. Sabanovic, L. Fridman and S. Spurgeon (Editors)
Volume 67	**Motion vision: design of compact motion sensing solution for autonomous systems** J. Kolodko and L. Vlacic
Volume 68	**Flexible robot manipulators: modelling, simulation and control** M.O. Tokhi and A.K.M. Azad (Editors)
Volume 69	**Advances in unmanned marine vehicles** G. Roberts and R. Sutton (Editors)
Volume 70	**Intelligent control systems using computational intelligence techniques** A. Ruano (Editor)
Volume 71	**Advances in cognitive systems** S. Nefti and J. Gray (Editors)
Volume 72	**Control theory: a guided tour, 3rd edition** J.R. Leigh
Volume 73	**Adaptive sampling with mobile WSN** K. Sreenath, M.F. Mysorewala, D.O. Popa and F.L. Lewis
Volume 74	**Eigenstructure control algorithms: applications to aircraft/rotorcraft handling qualities design** S. Srinathkumar
Volume 75	**Advanced control for constrained processes and systems** F. Garelli, R.J. Mantz and H. De Battista
Volume 76	**Developments in control theory towards glocal control** L. Qiu, J. Chen, T. Iwasaki and H. Fujioka (Editors)
Volume 77	**Further advances in unmanned marine vehicles** G.N. Roberts and R. Sutton (Editors)
Volume 78	**Frequency-domain control design for high-performance systems** J. O'Brien
Volume 81	**Optimal adaptive control and differential games by reinforcement learning principles** D. Vrabie, K. Vamvoudakis and F. Lewis
Volume 84	**Nonlinear and adaptive control systems** Z. Ding
Volume 88	**Distributed control and filtering for industrial systems** M. Mahmoud
Volume 89	**Control-based operating system design** A. Leva, M. Maggio, A.V. Papadopoulos and F. Terraneo
Volume 90	**Application of dimensional analysis in systems modelling and control design** P. Balaguer
Volume 91	**An introduction to fractional control** D. Valério and J. Costa
Volume 92	**Handbook of vehicle suspension control systems** H. Liu, H. Gao and P. Li

Design and Development of Multi-Lane Smart Electromechanical Actuators

Fawaz Yahya Annaz

The Institution of Engineering and Technology

Published by The Institution of Engineering and Technology, London, United Kingdom

The Institution of Engineering and Technology is registered as a Charity in
England & Wales (no. 211014) and Scotland (no. SC038698).

© The Institution of Engineering and Technology 2014

First published 2014

This publication is copyright under the Berne Convention and the Universal Copyright Convention. All rights reserved. Apart from any fair dealing for the purposes of research or private study, or criticism or review, as permitted under the Copyright, Designs and Patents Act 1988, this publication may be reproduced, stored or transmitted, in any form or by any means, only with the prior permission in writing of the publishers, or in the case of reprographic reproduction in accordance with the terms of licences issued by the Copyright Licensing Agency. Enquiries concerning reproduction outside those terms should be sent to the publisher at the undermentioned address:

The Institution of Engineering and Technology
Michael Faraday House
Six Hills Way, Stevenage
Herts, SG1 2AY, United Kingdom

www.theiet.org

While the author and publisher believe that the information and guidance given in this work are correct, all parties must rely upon their own skill and judgement when making use of them. Neither the author nor publisher assumes any liability to anyone for any loss or damage caused by any error or omission in the work, whether such an error or omission is the result of negligence or any other cause. Any and all such liability is disclaimed.

The moral rights of the author to be identified as author of this work have been asserted by him in accordance with the Copyright, Designs and Patents Act 1988.

British Library Cataloguing in Publication Data
A catalogue record for this product is available from the British Library

ISBN 978-1-84919-655-0 (hardback)
ISBN 978-1-84919-656-7 (PDF)

Typeset in India by MPS Limited
Printed in the UK by CPI Group (UK) Ltd, Croydon

Contents

Chapter 1

Introduction

Early aircraft controls were totally manually operated, that is, the forces required to move control surfaces were generated by the pilot and were transmitted by cables and rods. As aerodynamics and airframe technology developed and speeds increased, the forces required to move control surfaces increased, as did the number of surfaces. Thus, to provide the extra power required, hydraulic technology was introduced. The pilot's manual inputs were used to control the flow of hydraulic fluid to cylinders that subsequently moved the surfaces.

With further developments in aerodynamic and airframe technology and the arrival of airborne computers came the need for stability and control augmentation, which led to further developments in electrohydraulic actuation systems. In these systems, the pilot utilises flight control computers to electrically control hydraulic valves that in turn control the fluid flow. The control authority of computers was initially maintained well below that of the pilot to permit overcoming erroneous control inputs.

Today, with the advent of statically unstable aircraft, pilots are only able to control their aircraft with the assistance of complex and fast flight computers. This has led to the fly-by-wire concept, where the flight control surface hydraulic actuators are controlled entirely by electrical inputs. Here, the pilot input is sensed electrically and the mechanical control system is eliminated (i.e. rods or cables are eliminated).

The unavoidable element in the development of flight control systems (to date) has been in hydraulic actuators. This has been the case primarily because of their proven reliability and the lack of alternative technologies. However, the technology to build electromechanically actuated primary flight control systems is now available. Motors developing the required power at the required frequencies are now available with the use of high-energy permanent magnetic materials and compact high-speed electronic circuits. Therefore, development of this technology may mark the end of the hydraulic actuation systems, which are the last major non-electrical elements in the modern-day aircraft. This is considered to be an important step for the development of the future 'all-electric' aircraft. The purpose of the 'all-electric' aircraft concept is the consolidation of all secondary power systems into electric power. By eliminating the hydraulic and pneumatic secondary power systems, the aircraft benefits from improved maintainability and reliability, reduced life cycle costs, improved flight readiness and efficient energy use.

In recent years there has been much interest in the ‘all-electric’ aircraft, and its supporters have emphasised the serious consequences of hydraulic fluid loss on the aircraft safety. Furthermore, they highlighted the weight and space disadvantage of a centralised hydraulic power distribution system, especially when there are large distances between the primary power source and the actuators. Most experts agree that electric surface actuation systems will only show a weight-saving advantage if the hydraulic system is removed completely from the aircraft. There is, therefore, a strong case for the study of all-electric power actuators, their performance and integrity.

An enabling technology that took place in parallel with these developments was the development of brushless dc motors, which are relatively recent additions to electrical drives. The concept of brushless dc motors was first developed in 1964 by the National Aeronautics and Space Administration (NASA). The term ‘brushless’ is used to indicate that the motor is electronically commutated by sensing the rotor position, eliminating the brushes and commutators with the potentially dangerous sparking that is associated with conventional dc motors.

Although, these types of motors were introduced in the early sixties, only recent developments in solid-state devices (for rotor position sensing and controlling armature input power) and rare earth magnetic materials have contributed to their availability and wide spread use, both for aerospace and ground applications. The need for the development of brushless dc motors was urged by some for the advantages they enjoy over the brush-type motors. However, it must be emphasised that brushless dc motors will not totally replace the brush-type motors, since each type has its place in the range of motor applications.

Traditionally more than a channel of operation has been used to meet the stringent integrity requirements for aircraft control surface actuators. In fact, aircraft with powered flying controls would be fitted with at least two independent hydraulic power supplies driving a tandem hydraulic ram.

Fly-by-wire systems pose more difficult problems since they must be designed for failure-survival, thus corresponding designs of surface actuators are commonly found to have up to four lanes of parallel ‘first stage’ hydraulic actuation driving a duplicated or triplicated hydraulic second ‘power stage’.

Although electric power actuation is commonly used for slow-acting aircraft controls such as trim motors, flaps and slats, so far it has found almost no application, except in demonstrator aircraft, for driving primary aircraft controls because of the speed of operation required. However, hydraulic controls have the advantage of high power to weight ratio, thus they can easily achieve high speeds, and are commonly used in fast acting aircraft controls.

Actuator manufacturers currently hold the opinion that purely electric power actuators will eventually be developed to replace electrohydraulic actuators in the next few decades. To make this possible, there is a need to advance various essential areas of technology, including: power electronics, motor technology, thermal design, gearbox design, layout or architecture, control systems, failure monitoring and detection techniques, reliability and integrity.

This book describes design concepts in electromechanical actuators by considering an actuator with four lanes of actuation that has the capability to drive the aerodynamic and inertial loads of an aileron control surface similar to that of the Sea Harrier, with two lanes failed. Each lane of the multi-channel actuator contains its own dedicated microprocessor/s to perform control and comprehensive monitoring tasks. The mathematical models of the actuator (in its lumped and three-phase representations) and the acting loads will be derived from first principles. Furthermore, failure development, detection and isolation methods that are generally applicable to multi-lane electric surface actuators will also be explained.

The overall design has to meet both local actuator and global aircraft system performance requirements. Actuator requirements include: identify the control surface and the loads over the full flight envelope; maximum rotary output; minimum output rate; operation bandwidth; first nuisance disconnect probability; minimum damping of position servo; failure transients envelopes (which will affect the aircraft response). The aircraft system conditions that must be met include: the control surface geometry, aircraft speed range, maximum aileron authority limits at different aircraft speeds, maximum aircraft manoeuvre; maximum allowable bank angle and roll rate following first (and any other permitted following) failures.

The structure in which the design will be presented is highlighted next, starting with Chapter 2 where relevant technologies (to multi-lane electric actuators) will be presented.

Chapter 3 will present and verify basic equivalent circuits for the brushless dc motor.

Chapter 4 will present control system design steps, with the load mathematical modelling across a defined flight envelope.

Alternative methods of output consolidation with associated monitoring methods will be presented first in Chapter 5. A Simulation Graphical Monte Carlo (SGMC) method is then presented to set the thresholds on the Monitoring-Voting Devices (MVDs) within the Fault Detection and Isolation (FDI) System. The general methodology of its implementation to scheduled and unscheduled threshold settings will be presented.

Chapter 6 will present hardware cross monitoring in torque and velocity summing architectures, by considering lumped servo models.

Chapter 7 will present both hardware and digital cross monitoring to the torque summed architecture by considering three-phase servo models and lumped digital models.

Chapters 6 and 7 will present statistical variations in lane disparities for potentiometers, tachometers and motor currents. These are inherent random disparities due to random internal variations in the motor parameters and feedback signals from feedback devices, which were produced from samples of 1500 tests for different aileron deflections and during different flight cases.

Appendix 1 lists simulation tests (from Chapter 6) in hardware cross monitoring.

Appendix 2 lists simulation tests (from Chapter 7) in digital cross monitoring.

Chapter 2

Relevant developments

Over the years, aircraft flight control systems have evolved from being totally manually operated and generated to (what is commonly known today as) wire driven, hence the expression fly by wire. Fly by wire technology is where human or computer generated desired flight controls movements are represented by electronic signals that feed and operate (hydraulic or pneumatic) valves to drive the control surfaces, thus enabling on-board computers to perform functions at frequencies beyond pilot's abilities. With recent developments (in high-energy permanent magnetic materials and compact high-speed electronic circuits) it was made possible to extend this technology to the near future realisable concept of all-electric aircraft.

It is the aim of this chapter to present state of the art developments in electrohydraulic, electromagnetic and electromechanical actuators that led the way and influenced actuation designs for the future all-electric aircraft development.

2.1 The all-electric aircraft concept

The purpose of the all-electric aircraft concept is the consolidation of all secondary power systems into electric power. By eliminating the hydraulic and pneumatic secondary power systems, the aircraft benefits from improved maintainability, reduced life cycle costs, improved flight readiness and efficient energy use. This prompted numerous studies into electromechanical primary flight control actuation, which is considered a major milestone in the development of the all-electric aircraft, and led to the development of the electromechanical actuator systems, survivability, vulnerability and fault tolerance test programmes that addressed problems and benefits of the concept in the next generation fighters [1].

With advances in rare earth magnetic materials, solid-state power switching devices and high voltage dc power control, electromechanical actuator systems were made possible. However, concerns over the safety of flight mission reliability and combat survivability will have a major impact on the flight control hardware and architecture chosen for future aircraft. Retaining undiminished performance after failures places an enormous burden on the flight control system, and this capability is attained only at considerable cost and complexity. To meet these demands requires investigation into electromechanical actuator systems' survivability and reliability [1].

Electromechanical actuators have advantages over hydraulic actuators, not because they are better actuators in a conventional comparison sense, but because of the changes they allow in the total secondary power system of the aircraft, which means less weight, no hydraulic fluid leakage and consequently a reduction in fire hazards, less complexity and cheaper installation and maintenance costs [2].

Studies by the authors in [3] showed the need to reduce the susceptibility (in US Air Force aircraft) to hydraulic fluid-related fires. They tabulated hydraulic fluid-related fire mishaps over the period 1965–1983 and found that:

- Over 1970–1975, 90 hydraulic fluid-related fire mishaps mounted a total cost estimate of $100 million. Significant reduction was noted over the period 1976–1979, which rose again over the period 1980–1983.
- Over the period 1965–1979, 37 per cent of the hydraulic fluid fires were in cargo aircraft.

To increase aircraft survivability, the report recommended:

- The development of a truly non-flammable hydraulic fluid (which increases the weight).
- Urged further development in seals and equipment compatible with both high pressure and non-flammable fluids.

The study concluded that future aircraft losses (due to inadequate maintenance procedures or on-board equipment and system failures) must be reduced, which is an indirect request to investigate alternatives to hydraulic systems for the future aircraft.

The above studies pointed out that electromechanical actuators have more benefits when compared with hydraulic actuators. Although hydraulic actuator systems possess high force/weight ratio and high reliability, hydraulic systems still suffer from pressure transients, leakages, fire hazards, survivability in battle field scenario, and high installation and maintenance costs. However, the studies also showed that hydraulic actuators were more reliable than electromechanical actuator systems, due to the high probability of mechanical gearbox failure. In fact, acceptance of electromechanical actuators for primary flight control surface applications will undoubtedly rely on the acceptance of the gears in the mechanical transmission [1].

Holmdahl [4] described a single-channel electromechanical actuator that was designed by Boeing and was installed on the inboard spoilers of the NASA-owned Quiet Short-Haul Research Aircraft, which was completed in June 1982 and has undergone flight tests since then. The units were designed to fit the installation space and to replace a hydraulic actuator. The electromechanical actuator comprised of a samarium-cobalt permanent-magnet motor manufactured by Inland Motors of Radford\Virginia and a gear-ballscrew assembly (designed by Plessy Dynamics, Hillside, New Jersey). Holmdahl reported that the electromechanical actuator performance and response matched that of the original hydraulic actuator on the inboard spoiler and that of the outboard spoiler. The report also listed the further payoffs that this system offered, such as energy conservation, life cycle cost, operational readiness/ dispatch reliability, reduction in aircraft weight, reduction in system development and test efforts, improved survivability and the consolidation of energy/power sources into one electrical system. Furthermore, the report also emphasised the need for further investigations in performance after failure, tolerance and isolation, in order to achieve the above payoffs. It raised the importance of correct architecture (velocity versus torque/force summing) implementation and stated that a mix of the two types will be required in most aircraft applications. However, the choice between the two summing techniques is to a great extent, dependent upon failure considerations and failure mode characteristics. One consideration is that a velocity-summed actuator tends to fail open, zero output torque, leaving the control surface unrestrained. Whereas a torque-summed actuator tends to fail locked at the point of failure. Therefore, a surface such as a rudder, stabiliser or a canard that is flutter-prone tends toward torque summing, whereas spoilers tend to be candidates for velocity summing.

The reliability and redundancy study in the Holmdahl report revealed that the primary concern about the reliability of electromechanical actuators is the probability of a jam or structural failure in the gearbox section. A requirement that was established early in the Grumman programme, which stated that the electromechanical actuator systems reliability should be at least equal to that of the dual-tandem hydraulic actuator, so that, the probability of a critical failure be no greater than 10E-4 per flight hour [5]. The author also suggested that a fail-operational/fail-safe requirement would usually be acceptable in flight-critical applications, thus, the likely configuration of an electromechanical actuation systems would be *a four-motor design that meets full performance requirements with three motors operating and has a degraded performance (get home capability) with two motors operating.*

2.2 Electromechanical actuator development

This section describes key published programmes that gave basic design comparisons between electromechanical and hydraulic multi-lane actuators.

One of such programmes is the Lockheed-Georgia and Sundstrand Corporation teamed together with the USAF Flight Dynamics Laboratory. The programme was started in 1982 to develop flight worthy primary flight control electromechanical actuator hardware, evaluate its impact on flight control system design and demonstrate its capabilities in flight [6–9]. The programme described a *dual-motor driving a single ball screw through a torque summing gearbox electromechanical actuator* (Figure 2.1). The aircraft chosen to demonstrate the actuator was the C-141, and the surface to be controlled was the left-hand aileron. The actuator was intended to replace the existing hydraulic actuator on the aileron.

The controller was housed in the cargo bay of the aircraft with cabling to the actuator running along the inside of the wing’s trailing edge. The controller was to perform the functions of motor control, actuator position control, cross-channel equalisation and failure detection. The primary control input to the controller was the position error signal, which was generated by the mechanical feedback linkage and sensed by a Rotary Variable Differential Transformer (RVDT). The controller

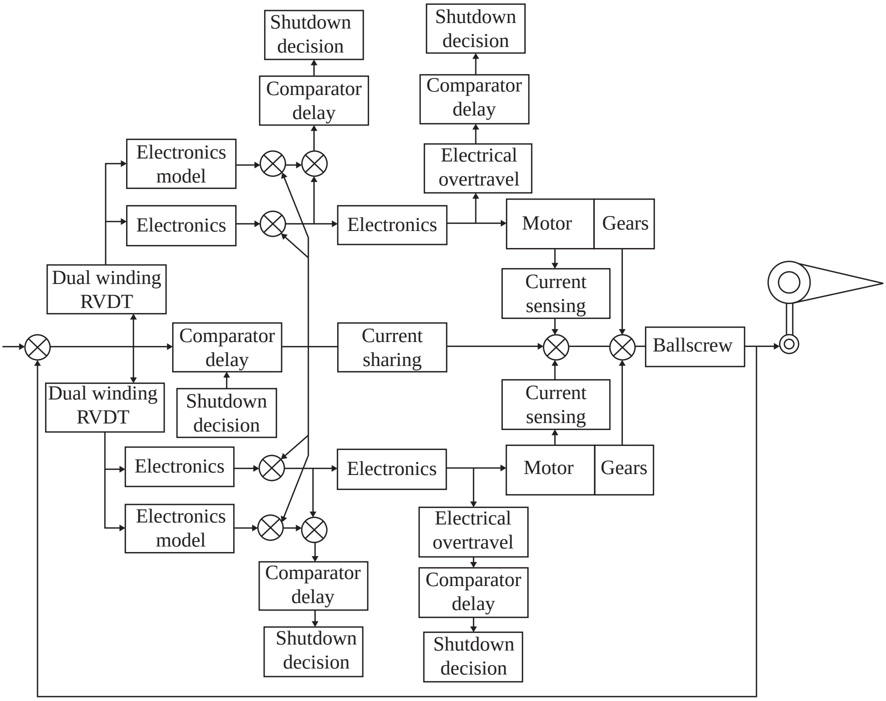

Figure 2.1 Block diagram of the electromechanical actuator developed by Lockheed-Georgia, Sundstrand Corporation and USAF Flight Dynamics Laboratory

drove the motor such as to maintain the position error signal as near to zero as possible. The voltage to the motor was controlled by pulse width modulating an internal 270 V dc power supply. The resultant average voltage was switched by six-switch inverter to the three-phase motor stator windings. The inverter switching sequence was determined by sensing the rotor position. For each rotor position, a unique switch sequence was selected from a custom programmable memory.

To minimise the force fight between the two motors, the controller equalised the current to each motor by regulating the output voltage. The current to each motor was monitored, and the difference between them connected to each motor's control loop so as to reduce that difference. The authority of this equalisation was minimised to reduce the impact of any component failure in its circuit. The controller performs several fault management functions, and all the actuator position sensors (including the motor commutation resolver) were monitored for failure. The operation of the control electronics was monitored by comparing the actual control parameters with those of a model that is incorporated into each channel. The balance between each motor was also monitored, so that if currents were to differ beyond a pre-set limit, the failed channel is shut down. The actuator was also monitored for over-speeding and over-travel, and when a failure was detected, the faulty channel was isolated and the cockpit enunciators were illuminated. Furthermore, the input power, bridge voltages and the temperature were monitored to provide an additional level of servo protection.

Thompson [8] and [9] shared reporting the success of the Lockheed-Georgia flight tests and reported that the electromechanical actuator operation was smooth and trouble free with no electromagnetic interference problems. It was also reported that there were no thermal problems and that the actuator ran a few degrees cooler than the hydraulic actuator in the other wing. Furthermore, power consumption during extensive system exercises was considerably less than expected, and the actuator drew a maximum current of 12.5 A. Moreover, the aircraft performance was identical to that of a standard C-141, and the pilot comments were 100 per cent favourable, indicating that the electric system performance was identical to its hydraulic counterpart.

The Sundstrand programme tests also reported that (in 1986) the C-141 underwent six sorties of 9–12 h duration flight tests [9]. In these tests, the electromechanical actuator system was operated in both dual- and single-channel modes throughout 9,000–41,000 ft and 80–390 kts flight envelopes. It was also reported that the controller had operated successfully after detecting a sensor failure that led to a shutdown of the faulty channel.

The other interesting programme that addressed electromechanical actuation and servo power conditioners was that conducted by Virginia Polytechnic [10–12]. The studies presented the development of a discrete time model to simulate a samarium cobalt type permanent magnet brushless dc motor. The model was developed as part of an overall discrete time analysis of the dynamic performance of electromechanical actuators. This was conducted as part of a prototype development, built for NASA Johnson Space Centre as a prospective alternative to the hydraulic actuator used in the shuttle orbiter applications. The mathematical modelling included the interaction between the machine and its transistorised power conditioner unit, where excellent correlations were reported between the numerical simulation and the actual hardware experimental tests.

2.3 Electromagnetically summed actuators

Another unique and very interesting programme was reported by Pond and Wyllie [13]. The authors described a magnetic torque summed electromechanical actuator that comprised of a rare earth permanent magnet brushless motor with quad redundant windings. Despite the reported encountered problems, the design was a brave and interesting attempted to increase reliability by removing the gearbox assembly.

2.4 Electrohydraulic actuators

Multi-lane actuators were also investigated by Dowty Aerospace [14]. The author compared the application of Electro-Hydraulic-Servo-Valves (EHSV) actuator with

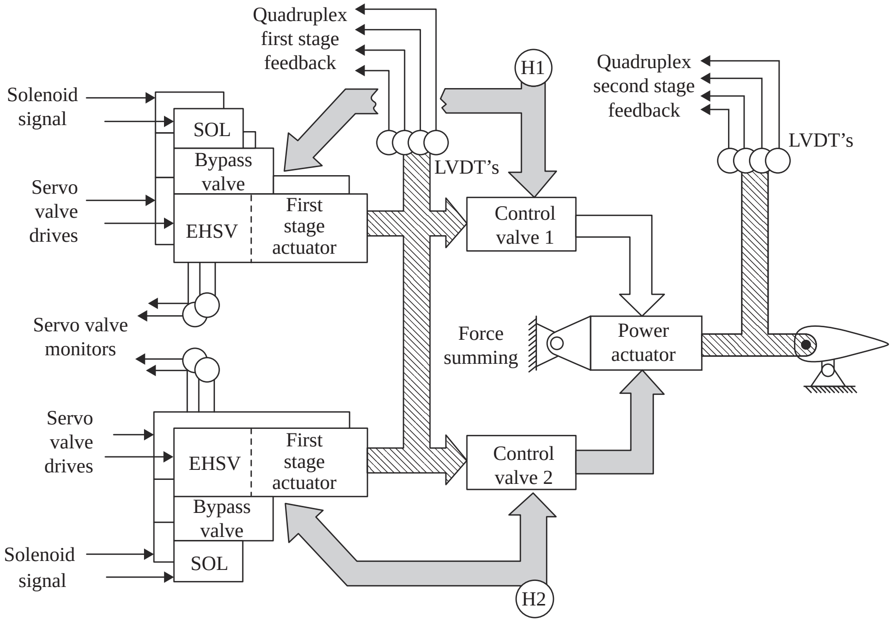

Figure 2.2 The BAe EAP actuator flow diagram, Dowty Aerospace, Wolverhampton

Direct Drive Valves (DDVs) actuation systems. Although an Electro-Hydraulic actuator system was described, architecture and the redundancy concepts remain of interest to state of the art actuators development. The programme investigated the Experimental Aircraft Project Actuator (shown in Figure 2.2), which was controlled by four computers, with each computer taking the error between demanded and measured positions to signal an EHSV. The actuator position was measured from four LVDTs within the actuator. The actuator operated from two hydraulic systems to provide redundancy, where each hydraulic system is associated with two EHSVs. This arrangement gives basic survivability of continued operation after one electrical and one hydraulic failure or two electric failures.

Each EHSV controlled a miniature actuator, and the group of the four actuators drove a tandem main control valve with local position control loop. The survival rule quoted previously means that the system has to continue to function on a single electrohydraulic channel, detecting and rejecting failures at the EHSV level, thus adding considerable complexity. The position of the EHSV spool position is measured by an LVDT and the measurement is compared against a valve computer model. In the event of error, a signal is generated to switch off a fail-safe solenoid valve, thus blocking the EHSV outputs and putting the failed valve actuator into a bypass condition so that it imposes no further constraint on the operation of the good lane.

The author then described the DDV actuator, which is much simpler (Figure 2.3). In this configuration the computer signals are flux summed at a single linear motor which directly drove the tandem main control valve. Again a position loop is closed

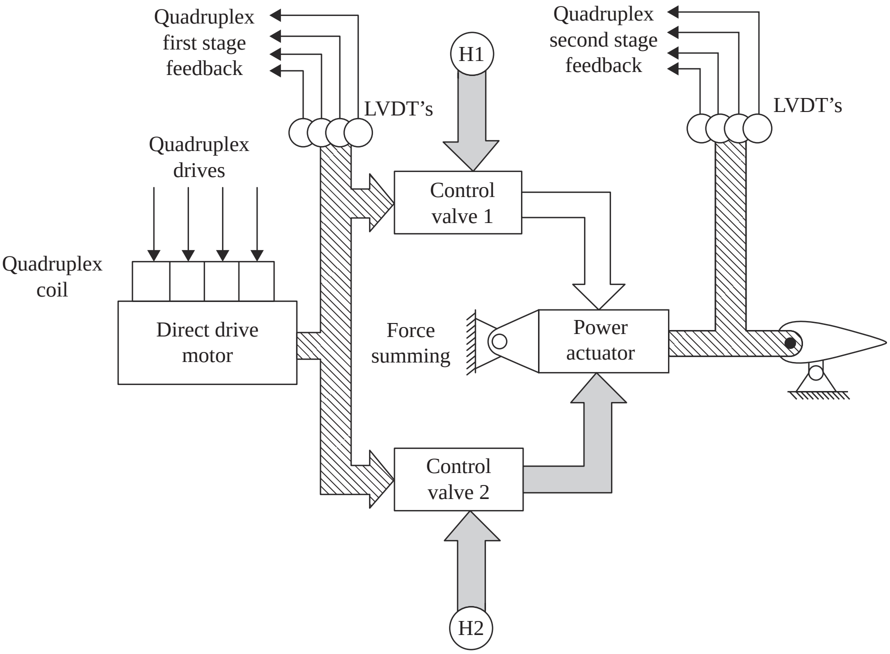

Figure 2.3 The EFA DDV actuator flow diagram, Dowty Aerospace, Wolverhampton

by four LVDTs. In this case the loss of a hydraulic supply does not impact the number of electrical lanes. Here, monitoring was achieved by measuring individual motor currents and comparing them to expected values.

Finally, the author described a simpler solution to the variation to the EAP solution, that is, the development of EHSVs with an integral bypass mode which is automatically selected after failure. This gives the benefit of the use of four separate control devices which give a better ballistic survivability when compared to DDV actuators. Despite this, the author favoured the implementation of DDVs for the significant benefits they offer for multiplex actuators and better reliability for simplex actuators. However, size works against DDV actuators, hence the author emphasised on the need for further investigations in their development, so that this technology would be even more widely applicable.

Figure 2.4 shows the electrohydraulic system of the B-2 advanced technology bomber. In this system, the four aircraft computers compute and generate commands to the actuator (in response to sensor inputs and guidance commands) and perform fault detection and isolation as well as provide control communications with the remaining avionics system [15]. The Flight Control Actuation System (FCAS) contains the flight control actuators and a quadruplex Actuator Remote Terminals (ARTs). The ARTs are distributed on the airframe so that a set of four redundant ARTs operated on each side of the aircraft. Each ART contains loop closure electronics for all flight control actuators on its own side of the airframe.

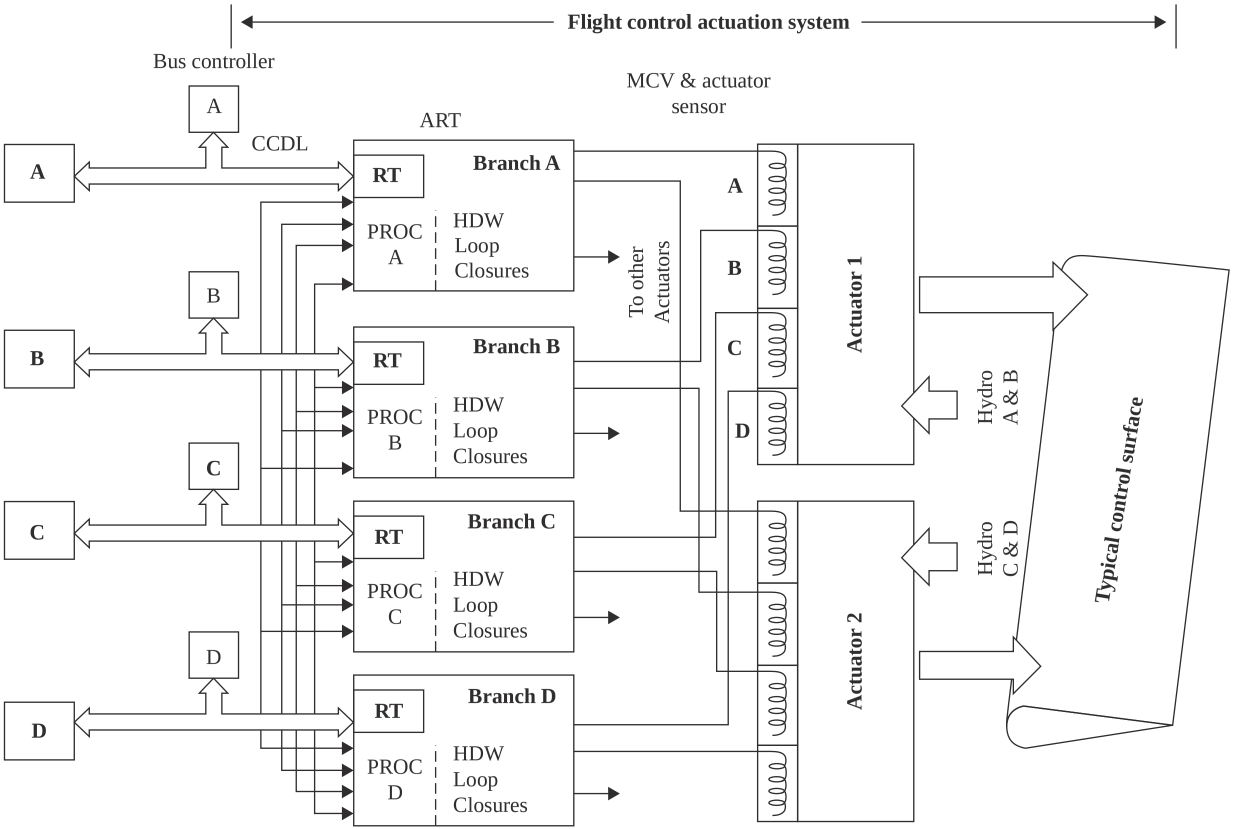

Figure 2.4   The B-2 flight control actuation system architecture block diagram

The actuator of each of the 11 primary flight control surfaces contains a Direct Drive Servo-Valve, a single piston and numerous quadraplex transducers.

Two hydraulic systems powered each actuator, with a mode control switch valve to select one of the three (primary, alternate and bypass) operating modes. At least two identical actuators drive each control surface and if there were sufficient failures to cause an actuator to bypass, the other actuator will continue to control the surface, albeit with reduced hinge moment capability. The hydraulic system is designed so that each of the four independent systems is available to every flight critical surface.

The FCAS has the capability to detect failures and reconfigure, utilising judicious monitors to detect failures. Each ART has numerous monitors that continuously measure the health of central ART functions, such as power supply voltages, central processing functions and dozens of other monitors. When a failure is detected, the offending ART is disabled. Monitors that detect failures within individual branches employ cross-channel comparison, comparing a local signal with the voted value of that signal from all branches (transmitted via a cross-channel data link). If the difference between the local signal and the voted value is greater than a predetermined threshold for longer than a programmed interval, then the signal is declared failed and its branch is shut down. The voter excludes failed signals (in the voting process) for the remainder of the flight, unless the failed signal is cleared.

2.5 The book approach

This book is concerned with the development of a smart electromechanical actuator that utilises brushless dc motors. Two architectures will be presented, the velocity- and torque summed architectures. Two motor models will be used in the designs, one is based on the McCormick and Electro-craft lumped model, and the other is the three-phase Taft model [16–19]. These two models will be used to address the designs issues; however, other more complex models are also available in the literature for the reader, such as those in [9, 10, 11, 20, 21].

Initially, the McCormick model is implemented for its simplicity to initially examine the actuator, and the effect of any lane disparities due to internal parameter variation and external transducer fluctuations for both velocity and torque summing architectures. The three-phase Taft model is then implemented to examine the torque ripple effect on lanes disparity.

While the three-phase model is used in hardware cross monitoring, the lumped and the three-phase models will be used in digital cross monitoring. A Monte Carlo Method will be utilised to evaluate scheduled and unscheduled threshold values, so that the system will have a maximum false alarm rate of 1.0E-4. Designs will be assessed by examining the effect of failure transients on the actuator and its impact on the aircraft response.

It is the aim of this book that the reader develops clear design strategy in high integrity systems.

Chapter 3

Modelling the brushless dc motor

Motors used for space applications have to meet certain special requirements, such as high reliability and very long (seven to ten years) unattended operational life under hard vacuum. They have to operate over a wide temperature range and should be capable of withstanding space radiation during operational life, vibration and shocks during launch and out gassing of the materials used. Also, they should have low power consumption and obviously minimum weight and volume. These requirements impose constraints on lubrication, bearings and materials used, therefore, the concept of a non-contacting system is preferred, hence, brushless dc motors were first developed in 1964 by NASA [22]. The term brushless is used to indicate that the motors are electrically commutated by sensing the rotor position, thus eliminating the brushes and commutator that are found in the conventional dc motors. Although they were introduced in the early sixties, only recent developments (in solid-state devices and rare earth magnetic materials) have contributed to the availability and wide spread of their use, both for aerospace and ground applications.

The need for their development was due to some of the advantages they enjoy over the brush-type motors, however, it must be emphasised that the brushless dc motors will not in all likelihood completely replace the brush-type motors, since each type has its place in the range of motor applications. Brushless dc motors enjoy advantages that are traditionally associated with the conventional dc motors, such as better efficiency, response time and linearity. They also enjoy the following additional advantages:

1. There are no brushes to wear or limit rotational speed. The wear factor may be important in applications that require high reliability for the military/aerospace markets or in situations where the motor installation makes it extremely difficult to replace brushes. Similarly, the absence of commutator bars precludes the problem of the commutator bar oxidation; therefore, brushless dc motors can sit idle for years with no loss of performance. Also, there are environments where brush arcing is very hazardous such as fuel pumps, grinders of materials that produce explosive dust, or spraying with flammable materials. Moreover, unlike the brush-type (where sliding contact against the commutation bars limits the maximum practical speeds of the brush-type motors), the brushless-type speeds is limited by the commutation electronics; therefore, motors with speeds up to 80,000 RPM have been built. Furthermore, the elimination of brushes also eliminates certain forms of radio frequency interference (RFI).

2. The winding configuration of a brushless dc motor allows the windings to be more effectively cooled. The stator may be cooled by conduction through mounting flange that is equipped with cooling fins or may have a water or cooling jacket.
3. High energy product magnet materials, such as samarium cobalt or Neodymium-Iron-Boron compounds, allow for a smaller rotor diameter than in conventional brush-type motor. This means lower inertia, faster acceleration and an enhanced control system.

However, the disadvantage in using brushless dc motors is the increase in the complexity of the drive circuits which means a definite increase in cost. Although the reliability of the brushless dc motor itself is higher than that of the brush type, the reliability of the drive electronics may be reduced due to the increase in the overall system complexity.

A brushless dc motor has the same physical laws that govern the conventional brush-type dc motor, but the primary difference is the inverse relationship of the rotating and stationary elements. The conventional dc motor has a stationary magnetic field and a rotating armature, while the brushless dc motor has a rotating permanent magnet assembly and a stationary armature winding, as shown in Figure 3.1. Commutation of electric current in the stationary armature is done by switching on the appropriate windings (by solid-state amplifiers) as a function of rotor position. Hence, brushless dc motors are also known as electronically commutated motors [17, 22].

There are a variety of devices, such as optical, inductive and capacitive transducers, magnetoresistors and Hall Effect generators for rotor position sensing [17, 22]. The optical arrangement consists of a disk attached to the rotor, an optical source and a photosensitive device. The light reflected by the rotating disk falls on the photosensitive device to generate the switching signal. Generally, inductive-type sensors are not used because they require complex circuits for excitation and demodulation. Also, the moving magnetic field may inhibit self-starting capability.

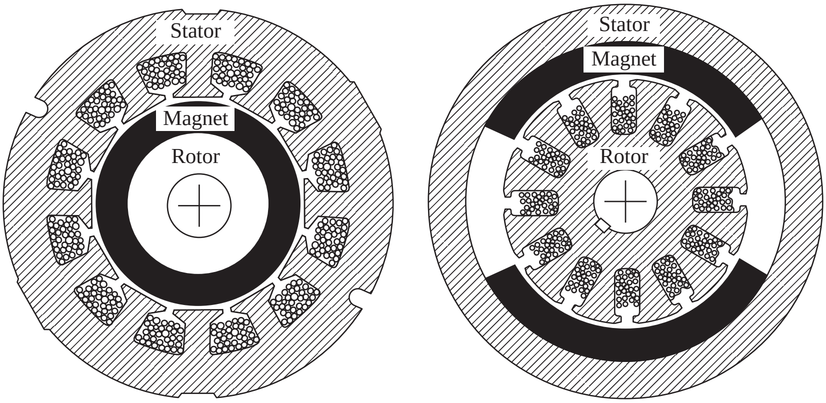

Figure 3.1 Cut-away view of brushless and conventional dc motor assemblies

The capacitive transducers also require complex circuits and hence are not suitable. Magnetoresistors do not have polarised output. The Hall Effect generator develops a polarised voltage depending on the control current and magnetic field passing through it. The unique property of polarised output means that only two sensors are required. The Indium and Antimony Hall effect semiconductor devices are very small in size and have higher sensitivity. As Hall Effect sensors have high reliability, low power consumption and don't require additional rotating disk and complex circuitry, they are widely used.

The following analysis was developed by the authors in [16, 17, 23]. This knowledge will be used in the development of the brushless dc motor lumped mathematical model in the actuator.

3.1 The lumped mathematical model

3.1.1 *Elementary magnetics*

A current carrying wire placed in a magnetic field (with the current flow perpendicular to the direction of the field) will cause a force to be exerted between the field producing element (permanent magnet, in this case) and the wire. This force is a cross product of the field strength, the wire length and the current in the wire.

$$\overline{F} = \overline{I} \times \overline{L}_w \times \overline{B}$$

where $\overline{F}$	Force vector
$\overline{I}$	Current vector
$\overline{B}$	Flux density vector
$\overline{L}_w$	Displacement vector in the direction of the current I

The direction of the force depends on the orientation of the magnetic field and the direction of the current in the wire. If the wire is disconnected from the current source and either it or the field was moved in a direction perpendicular to the other, a voltage may be measured across the ends of the wire. The magnitude of the voltage, $\overline{E}$, depends on the velocity, $\overline{v}_\omega$, with which the wire is moved through the field, or

$$E = B \times \overline{L}_\omega \times \overline{v}_\omega$$

Therefore, the force on the conductor in the magnetic field can be controlled by changes in $\overline{B}$, $\overline{L}_w$ or $\overline{I}$. In motor design, these are affected by the permanent magnetic material circuit design $\overline{B}$, the length and number of active conductors $\overline{L}_w$ and the total current $\overline{I}$. Similarly, the generated voltage is controlled by changes in $\overline{B}$, $\overline{L}_w$ and the rotor speed $\overline{\omega}_m$.

The above knowledge may be applied by considering the toroidally wound two-pole brushless dc motor shown in Figure 3.2. The conductors are shown wrapped around the stator. $\overline{L}_w$ from the previous discussion is the length of the active conductors (number of turns times the length L_w), the $\overline{B}$ is the magnetic flux density in the magnetic circuit, which is comprised of the North and the South

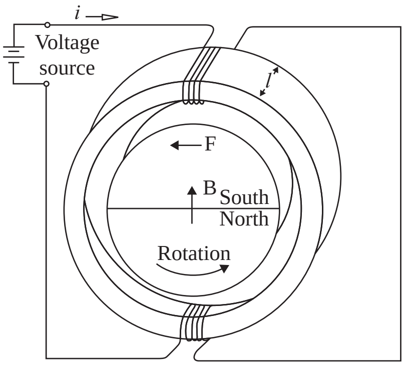

Figure 3.2 Two pole brushless dc motor

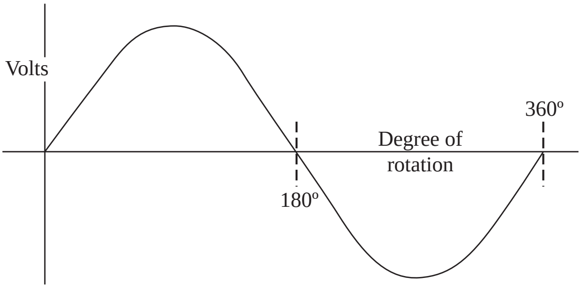

Figure 3.3 Terminal voltage applied

permanent magnets and the toroidal core. If current is applied to the conductors then $\overline{\mathrm{F}}$ is imparted tangentially to the rotor and torque results in the direction of the arrow. If the current source is removed and the rotor was to be allowed to rotate, an alternating voltage will appear across the terminals as shown in Figure 3.3. The alternating voltage results from the change in magnetic polarity as the rotor turns, where each coil sees alternately a North and then a South Pole. The amplitude and frequency of the voltage are dependent on the speed of rotation.

3.1.2 Commutation and the back emf waveform

One problem with the above design is that there is no way to make the motor rotate for a complete revolution. That is, as the current is applied in the direction shown in Figure 3.2, the motor will rotate to a point where the torques from the North and South fields are balanced, and no amount of current in the winding will cause torque. Thus the developed torque obtained for a given current is not constant as the rotor position is varied between two points where the field is balanced. However, intuition indicates that the amount of torque available for a given current should increase to some maximum at a midway between the two points where the fields are balanced. Therefore, to make the motor rotate through a complete revolution, we need to commutate the current in the windings as a function of rotor position. This means changing the direction of current in the coil at the proper time. In the brush-type motors this is done by the arrangements of brushes and commutation bars. For brushless dc motors, electronic switches and rotor position sensors are used.

Figure 3.4 schematically shows a typical brushless motor wound with three phases and the voltages seen between the phases (when the motor was driven as a generator at constant speed). The motor is wound to provide overlapping, sinusoidal three-phase voltages, electrically spaced by 120°. The North/South balance for each winding occurs where the voltages go through zero and reverse polarity. It is the method and type of winding as well as the geometric and physical characteristics of the rotor and stator that create the sinusoidal shape of the terminal voltage, the back emf (BEMF) of the motor. The torque produced by a motor with a given winding and physical geometry is directly related to the voltage it produces

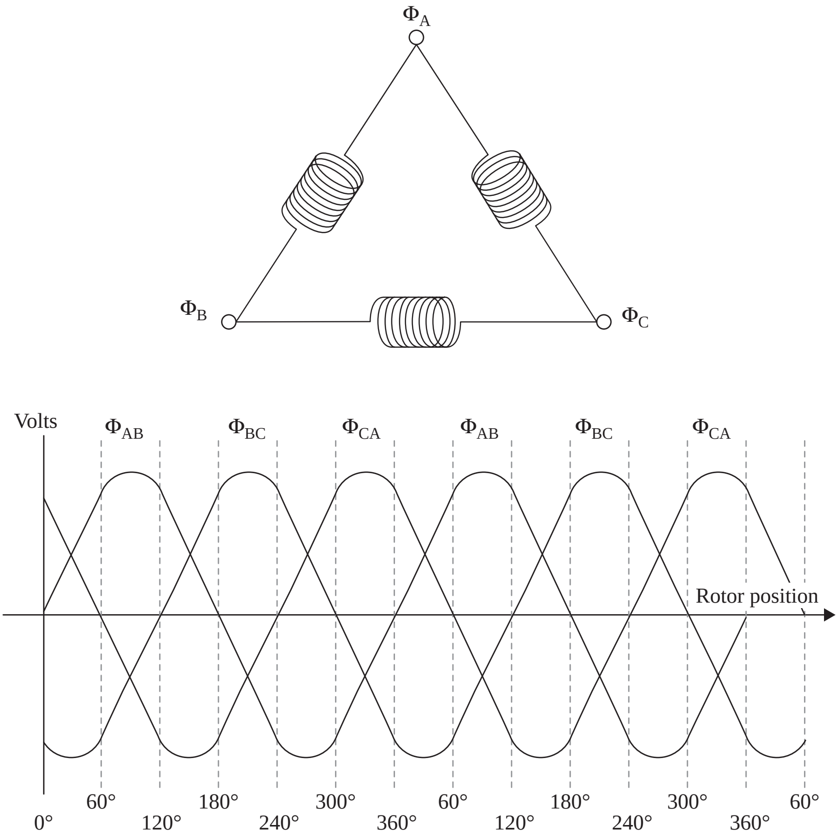

Figure 3.4 Typical three-phase brushless dc motor and the voltages between its phases

when the rotor is externally driven, or when the motor is used as a generator. In fact, the motor torque constant, K_T, and the motor voltage or BEMF constant, K_E, are equal when expressed in Nm/A and V/rad/s respectively.

This applies not only to the motor constants, but also to the wave shape throughout the commutation cycle. In other words, if the BEMF waveforms are viewed as a function of rotor position on an oscilloscope (when a constant current is applied to the motor), the torque as a function of rotor position will vary in a similar manner. Therefore, there is a logical way to decide when to commutate a brushless motor. In the discussion above it was found that commutating at the zero crossing of the BEMF waveform is not a good place to start since there is no resultant torque no matter how much current is injected into the phase. Also, it was found that peak torque for a running motor is achieved at the peak of the BEMF waveform. Hence if the motor is to run smoothly between commutation cycles, then the commutation zone should take place at the points of the centre of the peak BEMF waveform, as shown in Figure 3.5. This will provide equal sharing of motor phases in the process of producing torque, but will introduce variations of 50 per cent in K_T [16, 17].

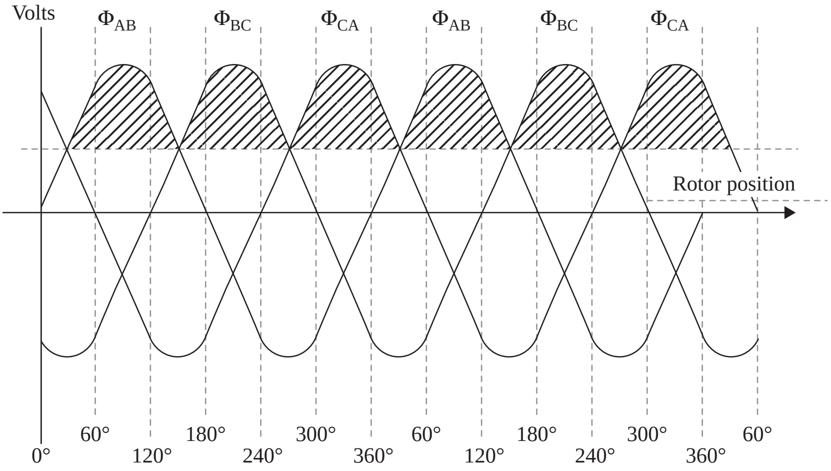

Torque ripple as a function of rotor position with constant current

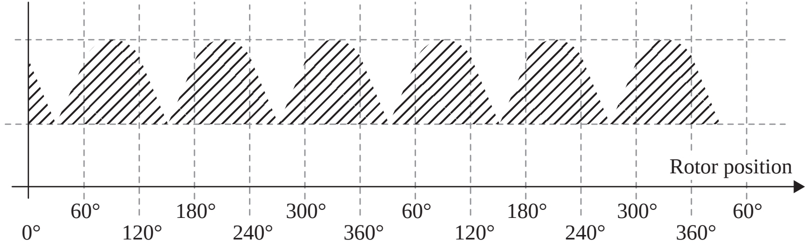

Figure 3.5 Torque ripple as a function of rotor position with constant current input and commutations at the positive half of the BEMF

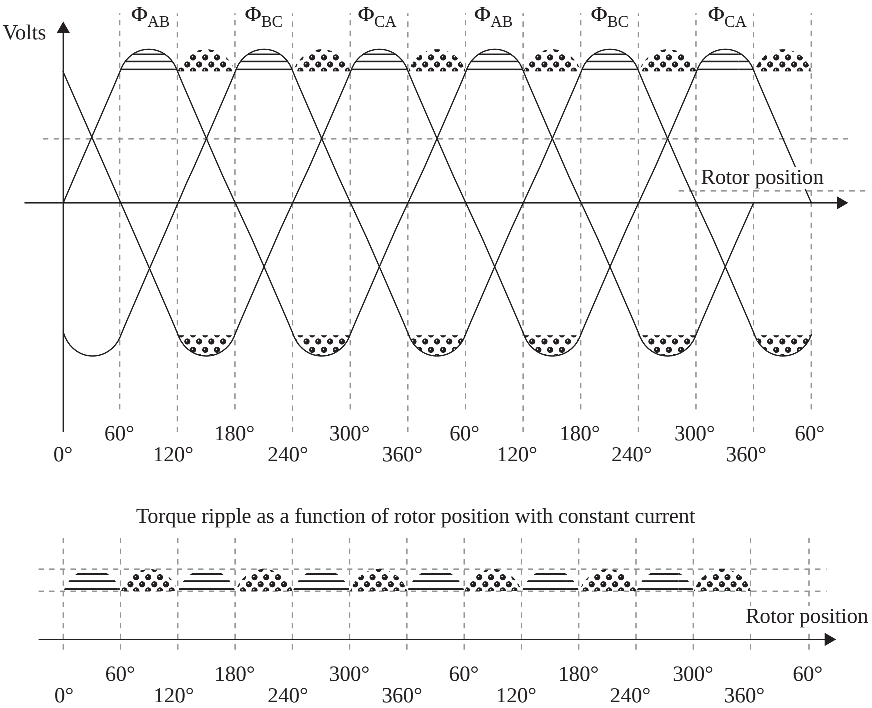

Figure 3.6 Commutation at the positive and negative halves of the BEMF

This might be considered acceptable in some applications such as ventilators and pumps. To improve this variation of torque during commutation, or the torque ripple, commutation frequency is doubled by using the negative and the positive half of the BEMF, as shown in Figure 3.6. This will yield a 13 per cent ripple. For a three-phase motor, this is considered to be the best that can be achieved when considering the BEMF waveform.

Further improvements to reduce the torque ripple may be achieved. One way is to increase the number of phases of the motor, thus increasing the number of commutation cycles per revolution. This means using smaller and smaller portions of the peaks of the BEMF waveform and thereby limiting the torque ripple excursion. This method is similar to that of increasing the number of commutation bars of the brush-type motor. The penalty in applying this to brushless dc motors is the increased number of transistor switches and commutation frequency.

A second method, and one that is more common, is to modify the shape of the BEMF waveform so that it is more trapezoidal (i.e. flat during the period of commutation), as shown in Figure 3.7. The ripple of this type of motor is much less than a motor with a sinusoidal BEMF waveform. In practice, the BEMF waveform cannot be made precisely flat due to the armature reaction, but torque ripple of 5–6 percent is achievable.

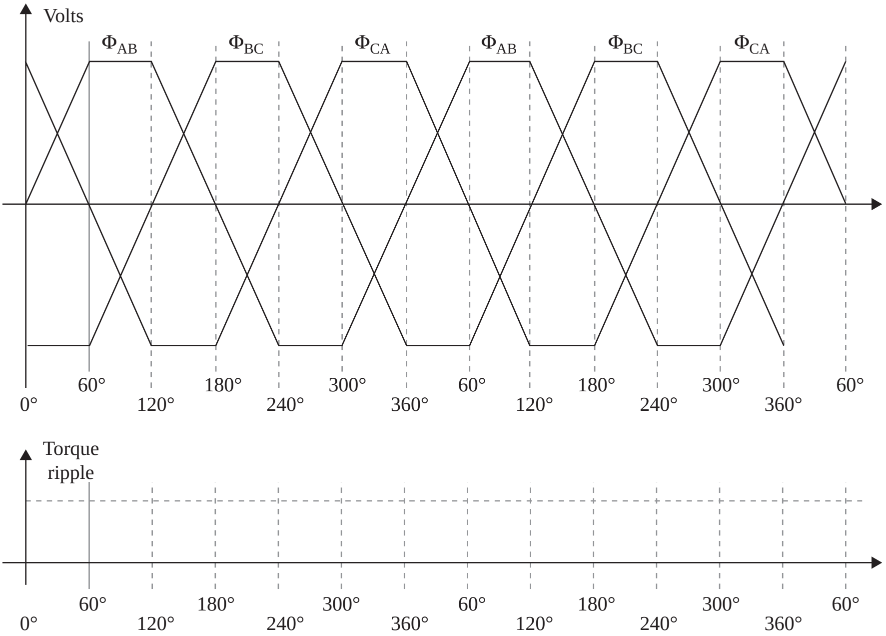

Figure 3.7 Commutation with trapezoidal waveform

3.1.3 Model development

The lumped model is a simplified mathematical representation, thus it is very useful in examining designs at the early stages. It is possible to assume that the brushless dc motor has the same mathematical model of that of the brush type if the following is assumed [16, 17]:

- Commutations are properly implemented using rotor position sensors and semiconductor switches, so that the brushless dc motor is commutated to follow the trapezoidal BEMF waveform.
- The values of K_T and K_E were assumed to be constant during commutation.
- Losses in semiconductor switches were assumed to be minimum and are neglected.

Thus, the brushless dc motor may be represented by the equivalent circuit shown in Figure 3.8. From this circuit the mathematical model may be derived as follows:

$$V = I * R + L\frac{dI}{dt} + K_E * \omega \tag{3.1}$$

where R Resistance of a phase winding
L Inductance of a phase winding

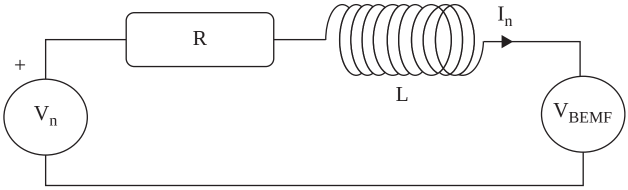

Figure 3.8 The brushless dc motor lumped equivalent circuit

V	Terminal voltage
K_E	Voltage constant of a phase winding over the conduction angle induced back EMF
I	Total of phase currents
ω	Motor shaft angular velocity

The above relationships hold well for the common brushless motor structures, although there are lower order effects due to mutual inductance between windings, overlapping conduction angles and unequal rise and fall times of current due to differing charge and discharge paths. The dynamic equation for the brushless dc motor when coupled to a load is given by

$$K_T * I = (J_m + J_L) * \frac{\partial \omega}{\partial t} + D * \omega + T_f + T_L \qquad (3.2)$$

where K_T	Torque constant of the motor winding
J_m	Motor moment of inertia
J_L	Load moment of inertia
D	Viscous damping coefficient
T_f	Friction torque
T_L	Load torque

In brushless dc motors T_f is small, usually only due to bearing drag, the viscous damping coefficient is also very small, and both items can usually be ignored in dynamic performance calculations.

Equations 3.1 and 3.2 may be rewritten as follows:

$$\dot{I} = \frac{1}{L}[V - I * R - K_E * \omega] \qquad (3.3)$$

$$\dot{\omega} = \frac{T_o}{(J_m + J_L)} \qquad (3.4)$$

where $T_o = K_T * I - T_L \quad$ (Net Torque)

Equations 3.3 and 3.4 represent the lumped mathematical model of the brushless dc motor, which doesn't exhibit any torque ripple effects behaviour.

Simulation tests show that the motor has the following angular speed to input voltage transfer function:

$$\frac{\omega}{V} = \frac{1}{K_e} * \frac{{\omega_{sn}}^2}{s^2 + \frac{R}{L}s + {\omega_{sn}}^2} \tag{3.5}$$

$$\text{where } \omega_{sn} = \sqrt{\frac{K_t\ K_e}{J_m * L}} \quad \text{(servo undamped natural frequency)} \tag{3.6}$$

$$\zeta_s = \frac{R}{2}\sqrt{\frac{J_m}{L\ K_e\ K_t}} \quad \text{(damping coefficient)} \tag{3.7}$$

and J_m being the motor inertia

To evaluate the transient response, the natural frequency and the damping of the motor, the parameters J_m, K_T, K_E, R and L for the Inland motor model A3000-50 were substituted [23].

$$\omega_{sn} = \sqrt{\frac{1 * 1}{4.5\text{E-4} * 17.7\text{E-3}}} = 354.33\ s^{-1},$$

$$\text{and} \qquad \zeta_s = \frac{7.2}{2}\sqrt{\frac{4.5\text{E-4}}{17.7\text{E-3} * 1 * 1}} = 0.574$$

The system has a time constant of $1/\omega_{sn}$ s or L/R s, T $\approx$ 2.5 E-3 (s) [23, 24].

Figure 3.9 is the speed–time transient response plot to a 100 V step input supply voltage. The overshoot in the response could be explained by the low value of ζ_s calculated above, which is related to the low inertia of the rotor. Also from the same plot, it can be seen that the motor has a steady state no-load speed of approximately

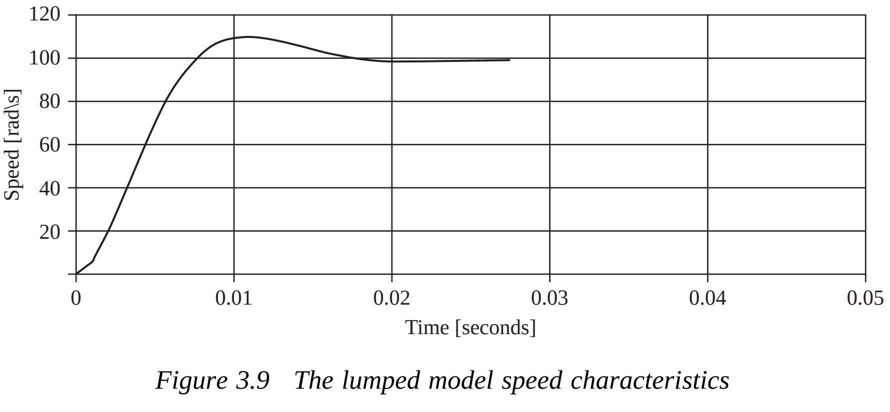

Figure 3.9 The lumped model speed characteristics

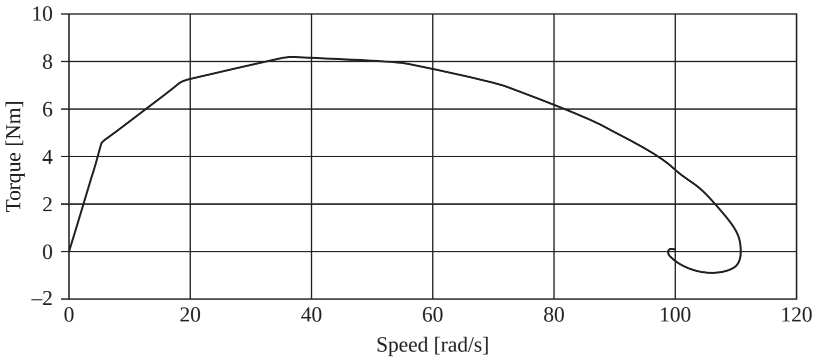

Figure 3.10 The lumped model torque-speed characteristics

100 rad/s, which matches manufacturer's data [23]. The Torque/Speed characteristics in Figure 3.10 are also the Current/Speed as $K_T = 1$. The figure shows that the peak current value is 8.0 A which is less than the peak permitted value of 14.7 A. The tail curl in the plot is due to the low rotor inertia. This model does not exhibit any torque ripple effects, but is considered adequate for the purpose of examining the different methods of consolidation of the lanes in the multi-lane actuator.

3.2 The three-phase mathematical model

3.2.1 Windings configuration

The brushless dc motor can be connected to electronic drive in one of several different configurations. The two most common configurations are the Delta and Wye, where nodes can be connected to supply, ground, or open circuited. It is possible to apply positive or negative supply voltages to the nodes causing larger currents to flow, thus requiring considerably more complex drives.

The authors in [18, 19] derived the torque-speed curves for a brushless motor with various possible drive arrangements or circuit interconnections. The analysis assumes that the motor is operating at a constant speed with negligible effects (due to sinusoidal terms that occur in the BEMF and in torque expressions). The analysis also assumes the phases to be mutually coupled, with sinusoidal current waveforms during torque delivery at constant speed. This is nearly always true for motors whose torque-angle and back emf-angle curves are nearly sinusoidal as was discussed earlier. Many brushless dc motors have trapezoidal torque-angle curves (TACs), however, the trapezoidal assumption is only an approximation and these torque-angle curves take a flattened sinusoidal form with the peak of the sine wave somewhat truncated, but the torque-angle curves and the back emf-angle curves will still have a nearly sinusoidal shape. This analysis, while it neglects harmonics, should provide accurate results even with motors having trapezoidal torque-angle curves [18, 19].

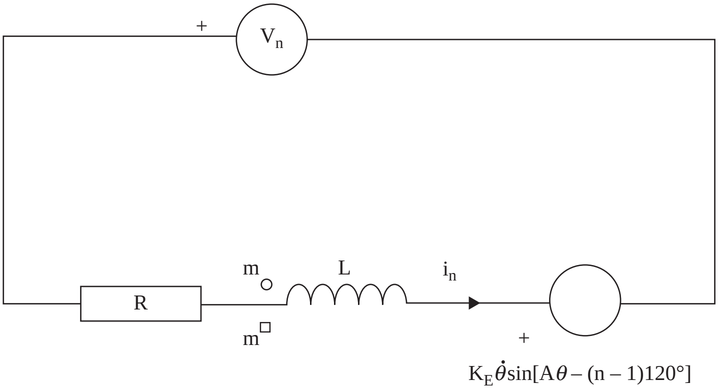

Figure 3.11 Phase electrical equivalent circuit

3.2.2 The equivalent circuit

To develop the above analysis, it is necessary to first consider each of the stator phase ideal element circuits. The phase circuit of a typical phase is shown in Figure 3.11. The phase has a resistance, inductance and BEMF source whose magnitude depends on the speed of the motor, and is a sinusoidal function of rotor angle and the phase angle associated with the mechanical location of the phase. Each of the phase circuits is mutually coupled to the other phases. The magnitude of this mutual coupling is denoted by m_o, a dot convention consisting of a square and circle denotes polarity. In each phase, the direction of current flow will be assumed to have a voltage across it whose positive terminal is located as shown in Figure 3.11. With this type of designation it is possible to develop an electrical equation for each phase to the voltage across the phase as shown in equation 3.8:

$$V_n = R * I_n + L\frac{\partial I_n}{\partial t} + m\frac{\partial}{\partial t}\sum_{p\neq n}^{3} I_p + K_E\ \dot{\theta}\sin(A\theta - (n-1)120) \tag{3.8}$$

where V_n Phase voltage, $n = 1$, 2 or 3
I_n Phase current, $n = 1$, 2 or 3
I_p Phase in mutually coupled phases, where $P = 1$, 2 or 3, and $P \neq n$
m Mutual inductance
θ Motor shaft mechanical angular displacement
$\dot{\theta}$ Motor shaft mechanical angular speed
A Number of pole pairs

This equation allows one to express the current through any phase in terms of the currents through the other phases and the voltage applied to the phase. The basic equation can then be combined with the ideal torque equation (equation 3.9), where the total developed motor torque is equal to the sum of the torques contributed by each of the phases.

$$T = \sum_{n}^{3} K_T I_n \sin(A\theta - (n-1)120^\circ) \tag{3.9}$$

where K_T Motor torque constant
T Total developed torque

3.2.3 The commutation states

Figure 3.12 shows the two basic types of Delta and Wye motor phase interconnections. With either type, it is possible to reverse currents in the phases without having to reverse supply voltages. It can be shown that when commutating a three-phase brushless motor, unless one can reverse the currents through the phases it is possible to produce only 120° apart torque-angle curves, and therefore the torque ripple is large. Whereas if one can reverse the current through the phases it is possible to produce torque-angle curves which are 60° apart, and thereby greatly reducing the torque ripple. Any commutation strategy controls the voltages at the nodes a, b or c. Therefore, by changing the voltages at the nodes to shift from one torque-angle curve to another, one may minimise the ripple at low speeds for a given phase interconnection circuit. This can be illustrated by examining commutation strategies for either of the two phase interconnection schemes shown in Figure 3.12.

A commutation strategy is simply a sequence of voltages applied to the nodes to produce nearly constant torques of given polarities with minimum ripple. It is possible to explore various control strategies by assuming different nodes potentials. As there are three nodes with three node states, there are 33 possible states. At low speeds (when the BEMF is insignificant), phase currents will result in torque-angle curves. Taft and Gauthier listed all the 27 possible combinations of voltage that might be applied to the motor nodes in Delta or Wye configurations. In each

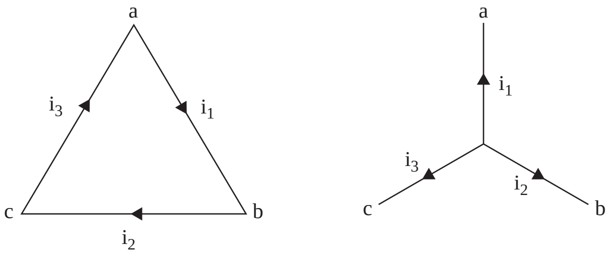

Figure 3.12 Delta and Wye phase connections

configuration, two groups of six commutation steps do emerge, where useful TACs are achieved. Other groups do not induce useful currents to produce TACs. Here, we will be concerned with the Delta configuration only.

Table 3.1 lists all the possible 27 combinations, with all the possible node voltages and resulting stall phase currents within TACs. The phase currents column clearly shows that there are only two sets of six commutation states (States$|_{4,2,6,5,7,3}$ and States$|_{18,16,17,21,20,19}$) that produce phase currents with 60° TACs. The other 15 states produce no currents in any of the phases. Figure 3.13 shows the positive torque developed, following the excitation Sates$|_{4,2,6,5,7,3}$ at electrical torque angles $A\theta^\circ = 30^\circ$, 90°, 150°, 210°, 270° and 330°. Clearly, unidirectional torque development is possible, simply by sensing the rotor angle and changing from one excitation to another, thus negative torques are developed following the commutation States$|_{4,3,7,5,6,2}$ [18, 19].

Table 3.1 Delta commutation states, currents and torques

State	**Node voltages to ground**			**Steady state currents**			**Torque-angle curve**
	a	**b**	**c**	**I1**	**I2**	**I3**	**T(Aθ) = T∠Aθ**
1	V_s	V_s	V_s	0	0	0	0
2	V_s	V_s	g	0	Vs/R	−Vs/R	$\sqrt{3}K_T V_S/R\angle 90^\circ$
3	V_s	g	V_s	Vs/R	−Vs/R	0	$\sqrt{3}K_T V_S/R\angle 330^\circ$
4	V_s	g	g	Vs/R	0	−Vs/R	$\sqrt{3}K_T V_S/R\angle 30^\circ$
5	g	V_s	V_s	−Vs/R	0	Vs/R	$\sqrt{3}K_T V_S/R\angle 210^\circ$
6	g	V_s	g	−Vs/R	Vs/R	0	$\sqrt{3}K_T V_S/R\angle 150^\circ$
7	g	g	V_s	0	−Vs/R	Vs/R	$\sqrt{3}K_T V_S/R\angle 270^\circ$
8	g	g	g	0	0	0	0
9	V_s	V_s	0	0	0	0	0
10	V_s	0	V_s	0	0	0	0
11	V_s	0	0	0	0	0	0
12	0	V_s	V_s	0	0	0	0
13	0	V_s	0	0	0	0	0
14	0	0	V_s	0	0	0	0
15	0	0	0	0	0	0	0
16	V_s	0	g	Vs/2R	Vs/2R	−Vs/R	$3k_T V_S/2R\angle 60^\circ$
17	0	V_s	g	−Vs/2R	Vs/R	−Vs/2R	$3k_T V_S/2R\angle 120^\circ$
18	V_s	g	0	Vs/R	−Vs/2R	−Vs/2R	$3k_T V_S/2R\angle 0^\circ$
19	0	g	V_s	Vs/2R	−Vs/R	Vs/2R	$3k_T V_S/2R\angle 300^\circ$
20	g	0	V_s	−Vs/2R	−Vs/2R	Vs/R	$3k_T V_S/2R\angle 240^\circ$
21	g	V_s	0	−Vs/R	Vs/2R	Vs/2R	$3k_T V_S/2R\angle 180^\circ$
22	0	0	g	0	0	0	0
23	0	g	0	0	0	0	0
24	0	g	g	0	0	0	0
25	g	0	0	0	0	0	0
26	g	0	g	0	0	0	0
27	g	g	0	0	0	0	0

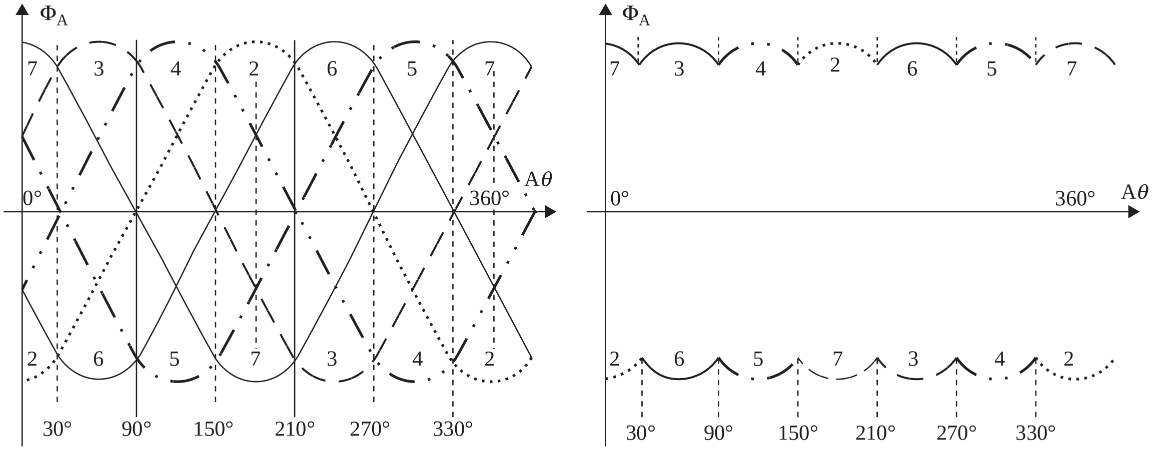

(a) (b)

Figure 3.13 Delta node closed low speed commutated TACs

3.2.4 The delta node closed model

In this section a closed node delta configured model will be developed, and its transient characteristics will be examined. The electrical equation 3.8 may be expanded so that the derivative of each phase current is expressed in terms of the other two-phase currents:

$$\dot{\mathrm{I}}_1 = \frac{1}{\mathrm{L}}\left[\mathrm{F}_1 - 2\mathrm{m}\left(\frac{\mathrm{F}_4 - \mathrm{F}_5}{2\mathrm{m} + \mathrm{L}}\right) - \mathrm{m}\left(\frac{\mathrm{F}_2 - \mathrm{F}_3}{\mathrm{m} - \mathrm{L}}\right)\right] \tag{3.10}$$

$$\dot{\mathrm{I}}_2 = \frac{\mathrm{F}_4 - \mathrm{F}_5}{2\mathrm{m} + \mathrm{L}} \tag{3.11}$$

$$\dot{\mathrm{I}}_3 = \frac{\mathrm{F}_2 - \mathrm{F}_3}{\mathrm{m} - \mathrm{L}} + \frac{\mathrm{F}_4 - \mathrm{F}_5}{2\mathrm{m} + \mathrm{L}} \tag{3.12}$$

where I_1, I_2, and I_3 are the currents in phases 1, 2 and 3 respectively
V_1, V_2, and V_3 are the voltage drops across 1, 2 and 3 respectively
$F_1 = V_1 - I_1R - BE_1$
$F_2 = V_2 - I_2R - BE_2$
$F_3 = V_3 - I_3R - BE_3$
$F_4 = (mF_1 - LF_2)/(m - L)$
$F_5 = m(F_2 - F_3)/(m - L)$

The ideal total torque developed by a lane equals the sum of the individual phase torques (equation 3.9). As mentioned in the previous section, if the motor were to be driven in closed node configuration, then the node voltages have to be switched using the first set of states shown in Table 3.1, where positive torques are achieved through $\mathrm{States}|_{4,2,6,5,7,3}$ and negative torques are achieved through $\mathrm{States}|_{3,7,5,6,2,4}$.

To clarify this positive and negative switching sequence, the voltages on the nodes and the electrical angle ranges at which each state should be maintained are listed in Table 3.2 below. The node voltages are set to Vn_{+ve} or Vn_{-ve} which is a terminology used only to determine whether the nodes are set at the same voltage

Table 3.2 Closed node and phase voltages in delta configuration

State sequence	Node voltages			Phase voltages			Electrical angles
	a	b	c	V_1	V_2	V_3	
7	Vn_{+ve}	Vn_{-ve}	Vn_{+ve}	0.0	−100.0	100.0	$330° \leq A\theta \leq 30°$
3	Vn_{+ve}	Vn_{-ve}	Vn_{-ve}	100.0	−100.0	0.0	$30° \leq A\theta \leq 90°$
4	Vn_{+ve}	Vn_{+ve}	Vn_{-ve}	100.0	0.0	−100.0	$90° \leq A\theta \leq 150°$
2	Vn_{-ve}	Vn_{+ve}	Vn_{-ve}	0.0	100.0	−100.0	$150° \leq A\theta \leq 210°$
6	Vn_{-ve}	Vn_{+ve}	Vn_{+ve}	−100.0	100.0	0.0	$210° \leq A\theta \leq 270°$
5	Vn_{-ve}	Vn_{-ve}	Vn_{+ve}	−100.0	0.0	100.0	$270° \leq A\theta \leq 330°$

level or not. Both Vn_{+ve} or Vn_{-ve} could take values of 100.0 or 0.0 V depending on the desired output torque. Therefore, for positive torque Vn_{+ve} or Vn_{-ve} will always be set to 100.0 and 0.0 V respectively; and to achieve negative torque, Vn_{+ve} or Vn_{-ve} are set to 0.0 and 100.0 V respectively. From this it becomes clear that the switching sequences for negative torque is exactly the same sequence as that for positive torque with the node voltages are reversed.

From the above analysis, the voltage drops across each phase (V_1, V_2 and V_3) may be calculated and substituted in equations 3.10–3.12, where V_1, V_2 or V_3 could have values of 0.0, −100.0 and 100.0 V. For example, Table 3.2 lists the phase voltages for a positive torque development switching sequence, thus to achieve negative torque, the signs of the voltages are reversed. Once the currents and the torques are evaluated, the motor dynamics can be simulated using the following mechanical equation:

$$\dot{\omega} = \frac{T_o}{(J_m + J_L)} \tag{3.13}$$

3.2.5 The electronic drives

There are several drive chips that are specially designed to commutate brushless dc motors. The MC33035 is an example of such integrated circuits, where it provides all the required functions to operate a brushless dc motor [25]. Shown in Figure 3.14, the IC is constructed with Bipolar Analogue technology and it offers a high degree of performance and ruggedness in hostile environments, which is an essential requirement for this particular application. It contains a rotor position decoder for proper commutation sequencing, a temperature compensated reference capable of supplying sensor power, a frequency programmable sawtooth oscillator, a fully accessible error amplifier, a pulse width modulator comparator, three open collector top drive outputs and three high current totem pole bottom driver outputs ideally suited for driving power MOSFETs. Furthermore, it includes protective features such as undervoltage lockout, cycle-by-cycle current limiting with a selectable time delayed latched shutdown mode, internal thermal shutdown and a unique fault output that can easily be interfaced to a microprocessor controller. Typical motor control functions include open-loop speed control, forward or reverse rotation, run enable and dynamic braking. In addition, the MC33035 has a 60°/120° select pin, which configures the rotor position decoder for either 60° or 120° electrical phasing inputs.

Some of the above operational functions performed by this integrated circuit will be taken into account in the modelling and control derivation to examine the actuator response to hardware failures. PWM will not be considered due to the increase in the required simulation time. Thermal shutdown will not be considered, however, variation in phase currents above a certain threshold will be considered. The chip will be assumed to switch the phases at 60° electrical phasing inputs, and closed loop control is achieved by assuming potentiometers and tachometers to

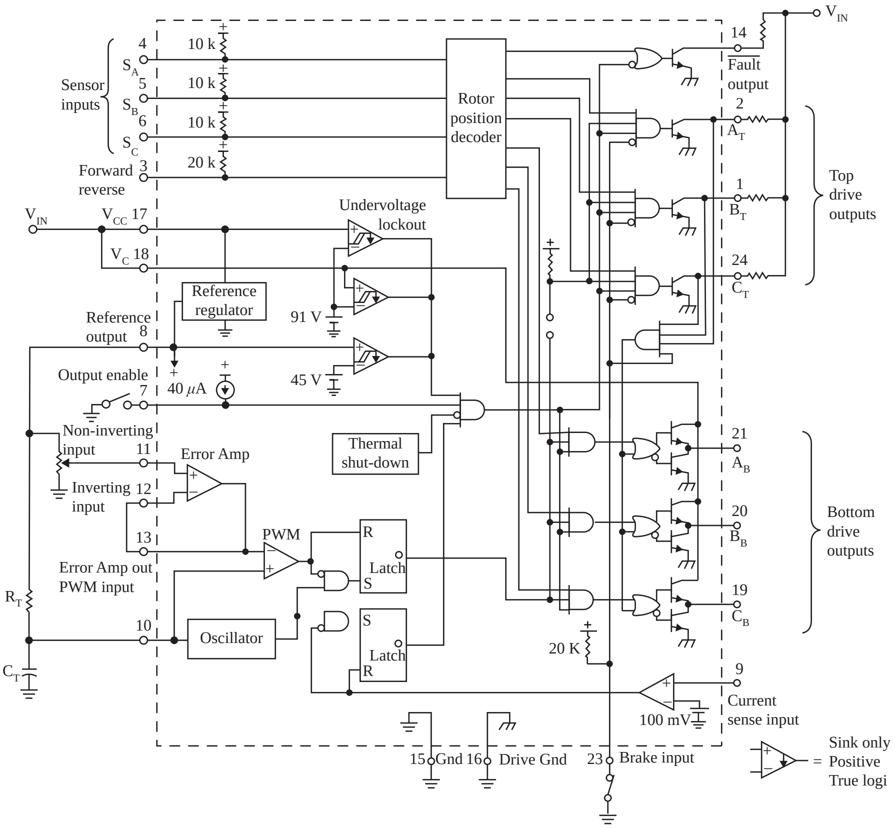

Figure 3.14 The MC33035 block diagram

provide rate and position feedback signals. The driving transistors connected to the phases were assumed to act as perfect switches.

3.2.6 *The transient response*

The model of the brushless dc motor described by equations 3.10–3.13 was simulated to investigate the transient behaviour of the motor. The mutual inductance between the phases was assumed to be very low (close to zero). This assumption introduced slight degradation in performance. In fact Taft and Gauthier recommended high values of mutual inductance to improve the performance [18]. The velocity transient responses with low and high mutual inductance (0 and 4 Henrys) are shown in Figure 3.15, with clear improvement in performance. Figure 3.16 describes the phase currents transient waveforms with the motor driving its own inertia. Figure 3.17 describes the voltages and the BEMF developed across the phases over one electrical cycle at steady state. The figure clearly shows how the

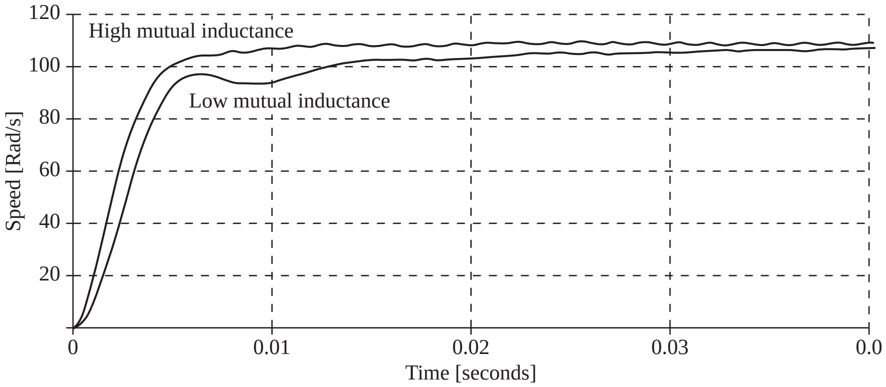

Figure 3.15 Velocity transient response for low and high mutual inductance

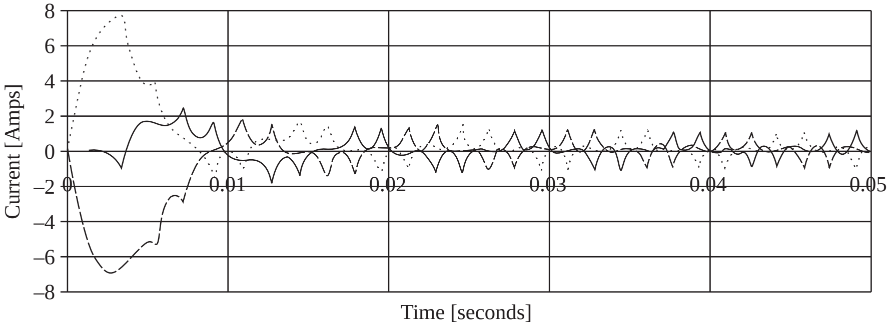

Figure 3.16 Current transient response

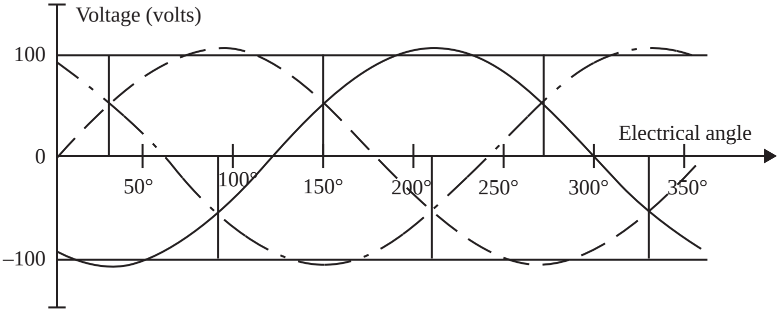

Figure 3.17 Phases voltages and BEMFs

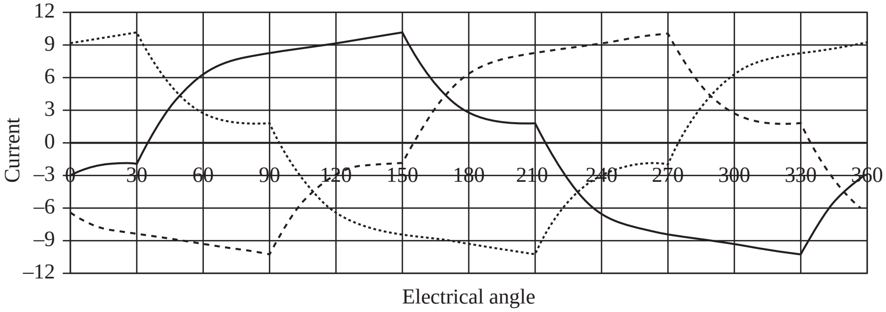

Figure 3.18 Current transient response

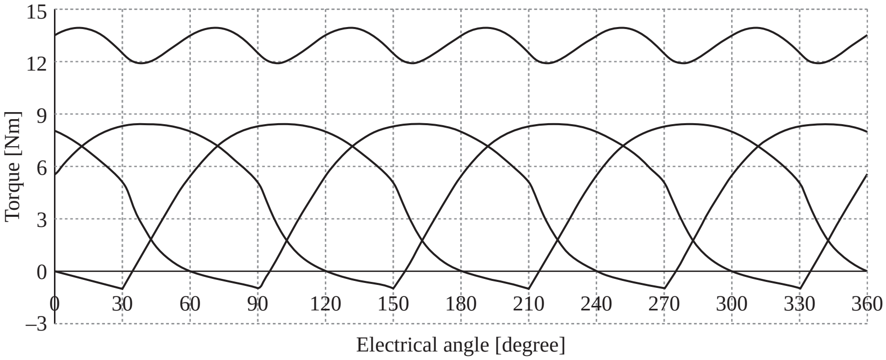

Figure 3.19 Transient phase and total torques

supply voltages across the phases are regulated between +100.0 and −100.0 V, approximately, depending on the rotor electrical angle as was discusses earlier. It also shows that the generated BEMFs are varying sinusoidally, in phase with the supply voltage between 100.0 and −100.0 V.

Figure 3.18 shows the steady state phase currents waveforms of a motor driving a constant load torque of 13 Nm. Figure 3.19 shows the developed phase torques due to such currents and the resultant torque which ripples around the constant load torque value. The last two figures show that commutation was carried out at the electrical angles: 30°, 90°, 150°, 210°, 270° and 330°. Figures 3.15–3.19 verify the validity of this model and clearly describe the motor in much greater detail when compared to the earlier presented lumped models.

Chapter 4
Control design

This chapter is dedicated to outline the control system design of the multi-lane electromechanical actuator. The development process is repetitive and has to be modified as new elements are included or more sophisticated models are considered at different stages of the design. This chapter presents an overview of how this is achieved, by considering lumped and three-phase servo models driving inertial and aerodynamic loads.

4.1 The lumped model

The closed loop block diagram of a single lane actuator with unity position feedback is shown in Figure 4.1. The brushless dc motor is represented by its lumped model and is coupled to the moving surface via a gearbox to overcome the inertial and aerodynamic loads. The inertial load is represented by a surface with a 0.128 Kg m^2 moment of inertia. The aerodynamic load model consists of a steady and a variable component. The steady component is constant during each flight case and depends on the angle of incidence, which is assumed not to exceed a maximum value of 15° and it is related to the aircraft speed and load factor. The variable component varies according to the aileron deflection and is at its peak at the maximum authority limit.

The drive voltage was applied through a power amplifier to the terminals of the motor with maximum voltage supply of ±100 V, which is shown as the nonlinear signum element in the forward path. This will be included once the characteristic equation poles are determined. Position and rate feedback will be included at a later stage along with proportional and integral actions to minimise steady state errors.

Cogging, friction damping, inertia of gearbox and thermal effects on the motor parameter variation were not taken into account, and zero backlash was assumed.

4.1.1 Unity feedback system

To explain the effect of the different components on the system behaviour, parameters such as gearbox ratio and forward gain were examined in a single lane with unity position feedback. With reference to Figure 4.1 and assuming that the system is operating in the linear region, the forward and closed loop transfer functions may be derived from electrical and mechanical motor equations.

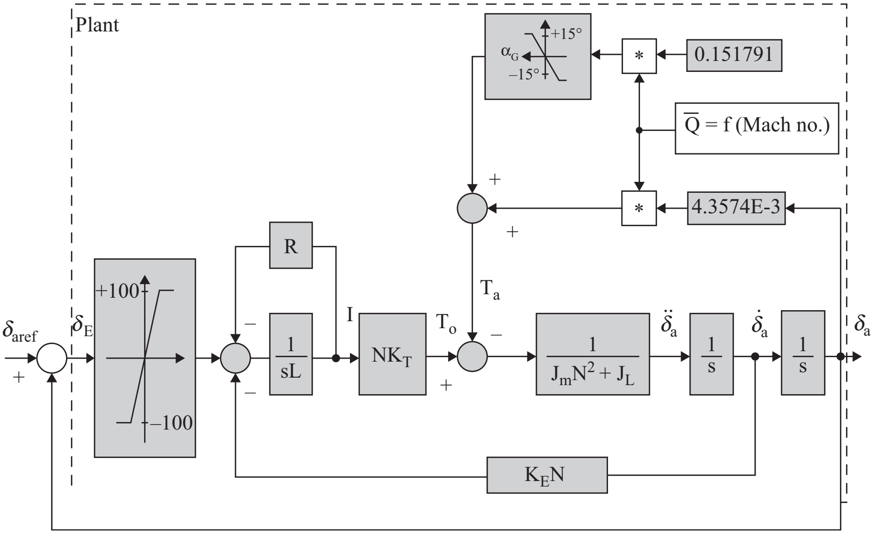

Figure 4.1 Single-lane closed-loop block diagram

The electrical equation of the motor is given by

$$\dot{I} = \frac{1}{L}[V - IR - K_E\omega_n] \tag{4.1}$$

The mechanical equation that relates the motor to the load is given by

$$T_m = K_T I \tag{4.2}$$

$$\ddot{\delta}_a = \frac{N\,T_m - T_L}{J_L + N^2 J_m} \tag{4.3}$$

where

$\ddot{\delta}_a$ is the angular acceleration of the load
T_m is the developed torque by the motor
J_m is the moment of inertia of the motor
J_L is the inertial load
T_L is the load torque
ω_m is the motor speed
N is the gear ratio, $N > 1$

For optimum acceleration, N is given by

$$N = \frac{T_L}{T_{mp}}\left[1 + \sqrt{1 + \frac{J_L T_{mp}{}^2}{J_m T_L{}^2}}\right] \text{ for optimum acceleration} \tag{4.4}$$

Taking Laplace transform of equations 4.1, 4.2 and 4.3 gives

$$I(s) = \frac{V(s) - K_E\omega_m(s)}{R + sL} \tag{4.5}$$

$$s\dot{\delta}_a(s) = \frac{N\,T_m(s) - T_L(s)}{J_L + N^2J_m} \tag{4.6}$$

Substituting for I(s) in (4.6) gives

$$T_m(s) = K_T\frac{V(s) - K_E\omega_m(s)}{R + sL} \tag{4.7}$$

Substituting the expression of $T_m(s)$ into equation 4.6 and rearranging gives

$$\dot{\delta}_a(s)\left\{sJ_{eq} + \frac{C_1}{R + sL}\right\} = -T_L + \frac{C_2}{R + sL}V(s) \tag{4.8}$$

where

$J_{eq} = [J_L + N^2J_m]$
$C_1 = N^2K_TK_E$
$C_2 = NK_T$

4.1.2 Ground test

A ground test means that all external aerodynamic loads are zero (i.e. $T_L = 0$) and the actuator has to overcome the inertial load of the aileron. This condition modifies the forward transfer function to

$$\frac{\delta_a}{V}(s) = \frac{1}{NK_E}\cdot\frac{C_3}{s^3 + s^2\dfrac{R}{L} + sC_3} \tag{4.9}$$

where

$$C_3 = N^2K_TK_E/[(J_L + N^2J_m)L]$$

Thus, a unity feedback system has the following closed loop transfer function:

$$\frac{\delta_a}{\delta_{aref}}(s) = \frac{\dfrac{C_3}{NK_E}}{s^3 + s^2\dfrac{R}{L} + sC_3 + \dfrac{C_3}{NK_E}} \tag{4.10}$$

This is a third order system, which may be written in the following general form [26]:

$$\frac{\delta_a}{\delta_{aref}}(s) = \frac{\dfrac{C_3}{NK_E}}{(s^2 + 2\zeta\omega_n s + \omega_n{}^2)(s + p)} \tag{4.11}$$

$$\frac{\delta_a}{\delta_{aref}}(s) = \frac{\dfrac{C_3}{NK_E}}{s^3 + s^2(2\zeta\omega_n + p) + s(\omega_n{}^2 + 2\zeta\omega_n p) + \omega_n{}^2p} \tag{4.12}$$

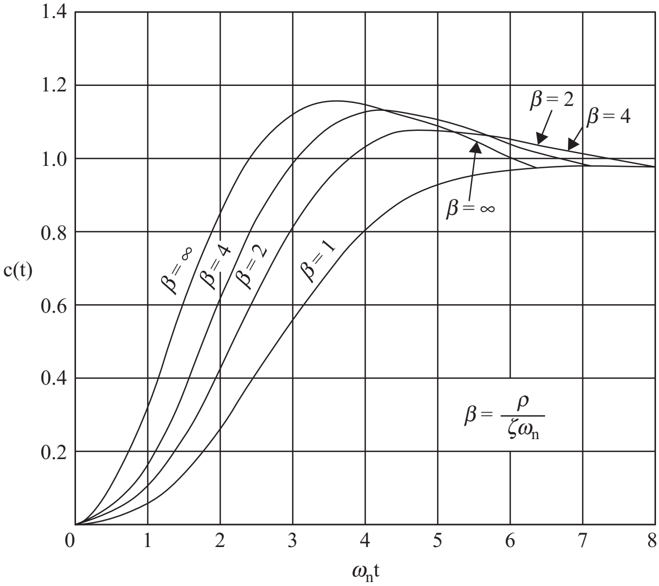

Figure 4.2 Unit step response of the third order system

$$\left[\frac{\delta_a}{\delta_{aref}}(s)=\frac{{\omega_n}^2 p}{(s^2+2\zeta\omega_n s+{\omega_n}^2)(s+p)},\zeta=0.5\right]$$

The effect of the pole $s=-p$ is that of reducing the maximum overshoot and increasing the settling time. Mathematical manipulation will lead to the ratio β. Figure 4.2 shows a family of curves for $\zeta=0.5$.

$$\beta=\frac{P}{\zeta\omega_n} \tag{4.13}$$

If the real pole in the 3rd order system is located to the right of the complex-conjugate poles, then there is a tendency for sluggish response, and the system will behave as an over damped system [26].

4.2 Initial design

The open loop poles of the lumped model may be found from equation 4.9, with $N=1$, $J_L=0$, $J_m=4.5\times10^{-4}$ Kgm^2, $L=1.7\times10^{-3}$ H, $R=7.2\ \Omega$ and $C_3=(N^2K_TK_E)/[(J_L+N^2J_m)L]$. Different loading scenarios may be considered.

4.2.1 Four motors driving own inertia (without gearbox)

The poles are $s=0$ and $s=-204\pm290i$.

4.2.2 Motors driving inertial load via gearbox

The open loop poles may be found from equation 4.14 with $N = 64$, $J_L = 0.126$ Kgm^2 and $J_m = 4.5 \times 10^{-4}$. The poles are $s = 0$ and $s = -204 \pm 286i$.

4.2.3 Actuator driving inertial and aerodynamic loads via gearbox

The Forward Loop Transfer Function (FLTF) of the actuator and the δ_a dependent aerodynamic component is given by

$$\frac{\delta_a}{V} = \frac{\lambda_{ol}}{s^3 + s^2\lambda_{o2} + s\lambda_{o3} + \lambda_{o4}} \tag{4.14}$$

where

$$\begin{aligned}
\lambda_{o1} &= MAG * N * K_t / J_o \pi L \\
\lambda_{o2} &= R/L \\
\lambda_{o3} &= [180 * L * CON + \pi * MAG * N^2 * K_t * K_e]/J_o \pi L \\
\lambda_{o4} &= 180 * R * CON/J_o \pi L \\
CON &= 4.3574E\text{-}3 * \overline{Q} \\
J_o &= J_L + N^2 J_m
\end{aligned}$$

Thus, $J_o|_{4\ \mathrm{motors}} = 7.5008$ Kg m^2, $J_o|_{3\ \mathrm{motors}} = 5.6576$ Kg m^2 and $J_o|_{2\ \mathrm{motors}} = 3.8144$ Kg m^2.

At the maximum authority limits, the coefficients of the numerator and denominator in equation 4.14 and the roots are as shown in Table 4.1, where very small shift in the positions of the open loop poles can be seen. This is due to the high gear ratio employed.

Table 4.1 Forward loop transfer function coefficients

	FLTFC	**Low aircraft speed**			**High aircraft speed**		
		4 motors	**3 motors**	**2 motors**	**4 motors**	**3 motors**	**2 motors**
Parameters	λ_{o1}	614	610	604	614	610	604
	λ_{o2}	407	407	407	407	407	407
	λ_{o3}	123500	122833	121520	126360	126624	127144
	λ_{o4}	38056	50459	74859	1201299	1592712	2362316
Roots	Real	−0.03	−0.01	−0.01	−0.17	−0.22	−0.33
	Complex	−204 ± 287i	−204 ± 285i	−203 ± 283i	−203 ± 291i	−203 ± 292i	−203 ± 293i
	Gain	614	610	604	614	610	604
	ζ	0.58	0.58	0.58	0.57	0.57	0.57
	ω_n	352	350	348	355	356	356

4.2.4 Inclusion of velocity feedback

Although the actuator has sufficient damping, inclusion of velocity feedback is essential to the design to provide damping adjustments when the non-linearities are considered. To demonstrate this, let's consider the low aircraft speed with the maximum authority limit at $\delta_a = 18^o$, $\delta_a|_{18^o,m=0.2}$.

The OLTF poles are positioned at $s = -0.03$ and $s = -204 \pm 287i$.

The locus for this particular flight case is shown in Figure 4.3. This loci is to be modified to pass through a dominant pole, S_{DP}, by introducing velocity feedback (Figures 4.4 and 4.5). S_{DP} is chosen so that the undamped natural frequency at this pole is unchanged, $\omega_n = 352$, with slight drop in value of ζ, $0.58 \rightarrow 0.5$.

$$\therefore S_{DP} = -176 \pm 305i$$

Following the introduction of velocity feedback, the OLTF is modified to $(K_d s + G)\lambda_{o1}/s^3 + s^2\lambda_{o2} + s\lambda_{o3} + \lambda_{o4}$, where the Zero was found to be located at $s = -352$, which is the ratio of $G/K_d = 352$, if G and K_d are approximately 50 and 0.14.

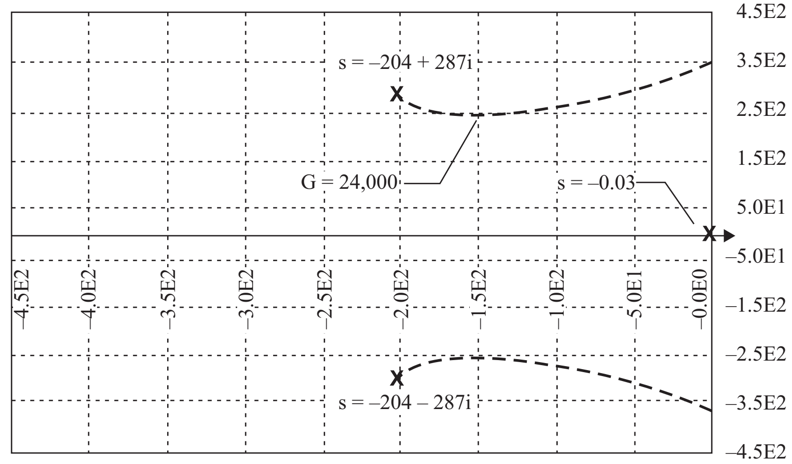

Figure 4.3 $\delta_a|_{18^o,m=0.2}$ *Open Loop Root Locus*

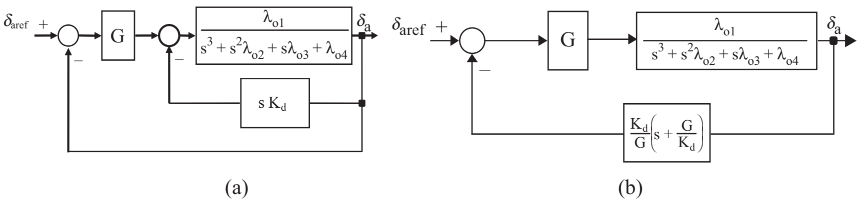

(a) (b)

Figure 4.4 Closed loop block diagram with velocity feedback

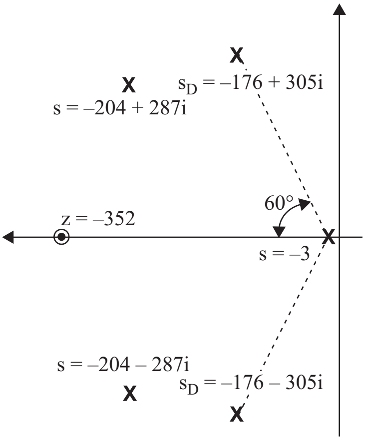

Figure 4.5 Root locus diagram

4.2.5 The integral controller

$$E(s) = \lim_{s\to 0}\left[s\frac{\delta_{aref}(s)}{1+K_p}\right] = \lim_{s\to 0}\left[s\frac{\delta_{aref}(s)}{1+G(s)H(s)}\right]$$

$$E_{ss} = \frac{\delta_{aref}{}^{o}}{1+\frac{G\lambda_{o1}}{\lambda_{o4}}} = \frac{\delta_{aref}{}^{o}\lambda_{o4}}{\lambda_{o4}+G\lambda_{o1}}$$

$$\begin{array}{llllll} \text{For} & K_p \approx 0.8, & E_{ss} \approx 10^{o} & \delta_a|_{18^{o},m=0.2} & \text{and} & G = 50 \\ \text{For} & K_p \approx 0.026, & E_{ss} \approx 1.95^{o} & \delta_a|_{2^{o},m=1.0} & \text{and} & G = 50 \end{array}$$

The value of E_{ss} will be much higher when the steady component of the aerodynamic load is included. Hence, the integral action inclusion is considered essential. To achieve this, a lag filter of the form $s + a_{lag}/s + b_{lag}$ is added in the forward path (where $a_{lag} > b_{lag}$). The pole was assumed to be at $s = -0.01$ and the desired value of $E_{ss} \leq 1.95^{o}|_{K_p=1800}$ for low aircraft speed. Thus the position of the zero may be calculated as follows:

$$K_p = 0.8 * \lim_{s\to 0}\lfloor s + a_{lag}/s + b_{lag}\rfloor$$

$$\therefore\ a_{lag} = -22.5$$

This filter has a very little effect on the general response. In fact it has a magnitude and angle contribution of 1° and 3°. Since $b_{lag}\langle\langle a_{lag}$, the lag filter may be approximated by the proportional and integral actions $G + a_{lag}/s$.

These calculated parameters are initial estimates, and are likely to be modified to achieve acceptable performance for all modes. In the aircraft application, it is important to include the load torque model to examine a realistic performance, especially under failure conditions.

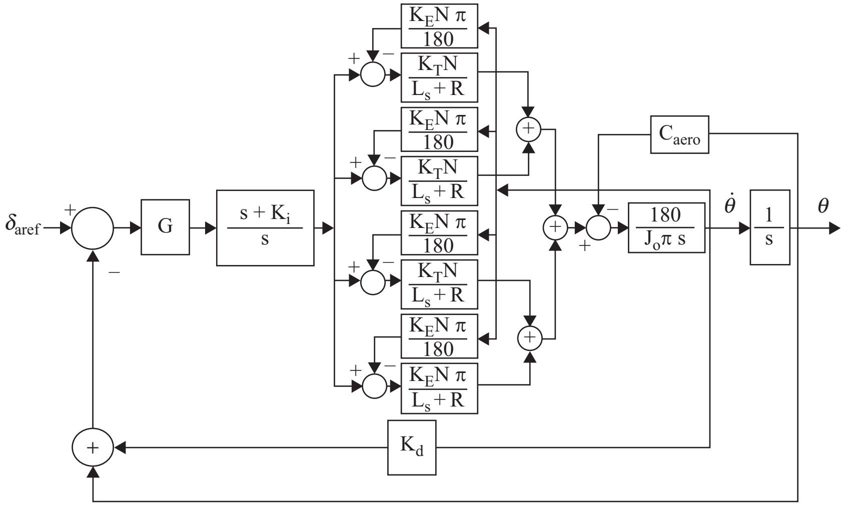

Figure 4.6 Linearized closed loop block diagram of the multi-lane actuator

4.3 Design modification

Figure 4.6 is the closed loop block diagram of the multi-lane actuator in its torque-summed architecture, with proportional plus integral (PI) action (to minimise any steady state errors) and velocity feedback to adjust the damping. The values of the controller parameters and gear ratio were constantly modified from the baseline root locus design to meet the performance requirements in both frequency and time domains. The presence of the integral action makes it possible to reduce the gearbox ratio (64:1 in this particular design), hence increasing the bandwidth. Naturally, the gearbox ratio should be selected so that the actuator is capable of driving external loads after two failures.

The values of the proportional (G), integral (K_i) and velocity feedback (K_d) gains were adjusted so that adequate closed loop performance is achieved for all flight cases with acceptable damping, following channel isolation after failures. The CLTF of the block diagram of Figure 4.6 is given by

$$\left[\frac{\delta_a}{\delta_{aref}}(s) = \frac{\lambda_5(s+K_i)}{(\lambda_1 s^4 + \lambda_2 s^3 + \lambda_3 s^2 + (\lambda_4 + \lambda_5)s + \lambda_5 s K_i)}\right]$$

where

$\lambda_1 = L.\,\pi.\,J_0$
$\lambda_2 = R.\,\pi.\,J_0$
$\lambda_3 = 180.\,N.\,MAG.\,G.\,K_d + 180.\,CON.\,L + N^2.\,\pi.\,Mag$
$\lambda_4 = 180.\,CON.\,R + 180.\,N.\,MAG.\,G..K_i.\,K_d$
$\lambda_5 = 180.\,N.\,MAG.\,G$
$J_0 = MAG.\,J_m.\,N^2 + J_L$
$CON = \overline{Q}.\,4.3574E - 3$
J_m = motor inertia
G = forward gain
N = gearbox ratio
R = motor resistance
L = motor inductane
J_L = load inertia
MAG = number of lanes in operation

Table 4.2 Low speed closed loop roots with nominal controller coefficients

Four lanes		Three lanes		Two lanes	
Poles	**Zero**	**Poles**	**Zero**	**Poles**	**Zero**
$-191 \pm 744i$, -17 & -7	-20	$-191 \pm 743i$, -18 & -6	-20	$-190 \pm 739i$, -20 & -6	-20

Table 4.3 High speed closed loop roots with four lanes operational

	Poles	Zero	ω_n	ξ
Nominal	$-191 \pm 744i$, -17 and -7	-20	769	0.25
2 K_d	$-192 \pm 1014i$, -19 and -3	-40	1032	0.19
0.5 K_d	$-190 \pm 563i$, -13 and -4	-10	594 & 14	0.3 & 0.95
2 K_i	$-183 \pm 743i$, -33 and -7	-20	765	0.24
0.5 K_i	$-196 \pm 745i$, -10 and -6	-20	771	0.25
2 G	$-191 \pm 1014i$, -18 and -7	-20	10131	0.185
0.5 G	$-193 \pm 564i$, -15 and -6	-20	596	0.32

The poles and zeros with nominal controller coefficients (before and after failures) are listed in Table 4.2, where it is evident that reduction in driving force (following failures) has little effect on the general system characteristics (ω_n & ξ); however, the slight shift in dominant poles reduces the speed response.

In applications where there are variations in operating conditions and system parameters, it is necessary to perform sensitivity analysis to examine the effect of parameters variation on the system dynamics and response. In this particular application, there is variation in flight conditions and the number of lanes in operation; therefore, it is necessary to perform sensitivity analysis to examine the effect of varying G, K_i and K_d on the system dynamics. Here, the system performance with nominal design values was compared against the performance when parameters were halved and doubled. Table 4.3 lists the closed loop poles, zeros, ω_n and ξ for the different conditions. Figures 4.7–4.9 show the shift in the poles position as the coefficients were varied. It follows that:

- **Natural Frequency, ω_n:** increases as the values of either G or K_d is doubled and decreases as their values are halved. Variation in K_i has very little effect on ω_n.
- **Damping coefficient, ξ:** increases as the values of either G or K_d is halved and decreases as their values are doubled. Variation in K_i has very little effect on ω_n.
- **Dominant roots:** slightly changed with changes in G and K_i, however, the response is clearly affected when K_d is changed, as shown in Figures 4.10–4.12.

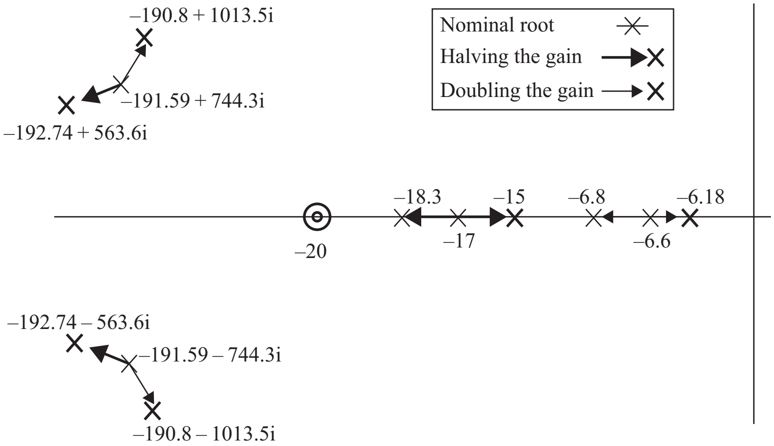

Figure 4.7 Poles shift due to forward gain variation

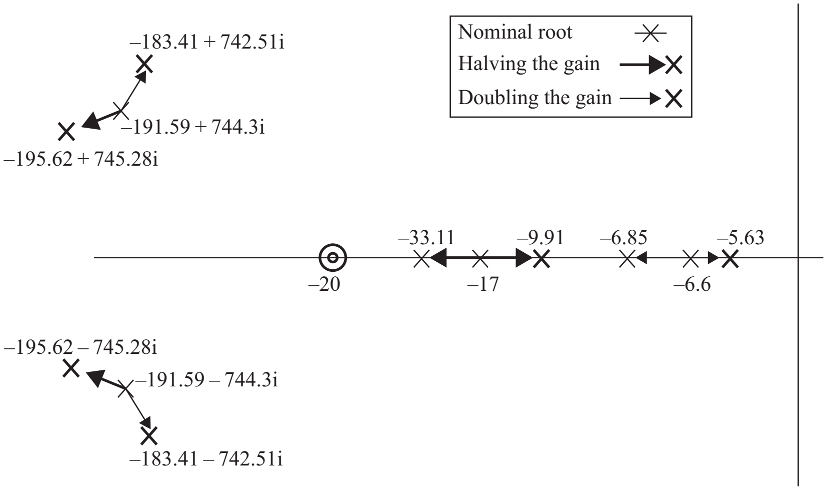

Figure 4.8 Poles shift due to integral coefficient variation

Figures 4.13 and 4.14 show the step response to the maximum authority limits for low and high aircraft speeds. The actuator was assumed to drive the full inertial and aerodynamic loads. Clearly, the current design is rugged and position control is achieved in all cases with approximately zero steady state error.

4.4 Advanced design stage

In the advanced design stages more accurate three-phase motor models should be considered. Step and frequency response tests should be repeated for various operating conditions. The actuator response to three-phase and lumped models for

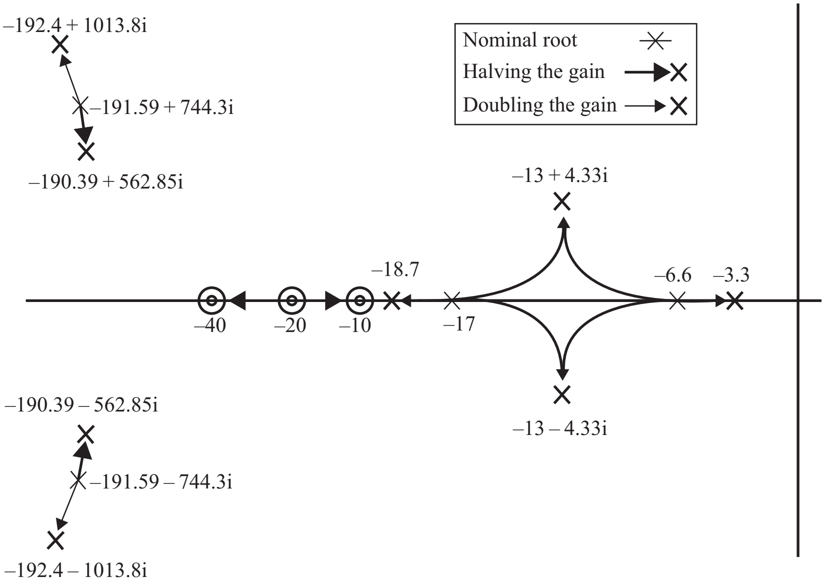

Figure 4.9 Poles shift due to velocity feedback coefficient variation

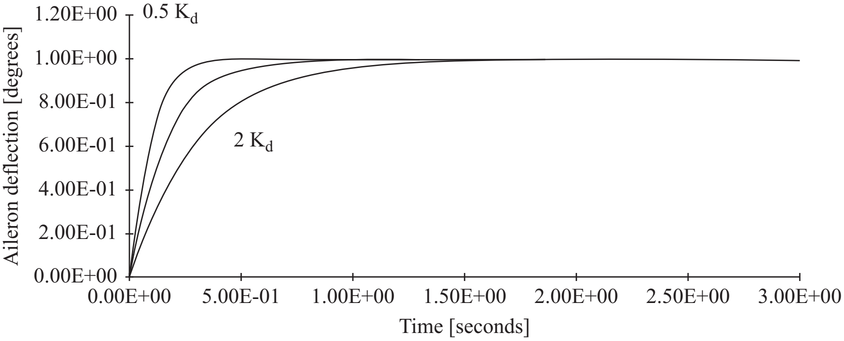

Figure 4.10 Effect of varying velocity feedback gain

different flight cases are shown in Figures 4.15–4.18. The actuator was assumed to have four lanes driving inertial and aerodynamic loads.

In addition to time domain tests, it is important to conduct frequency domain tests that cover all flight envelopes. The importance of such tests becomes more evident as the inertial loads become more dominant at higher frequencies. In fact, the loads can be as high as four or five times that of the aerodynamic load.

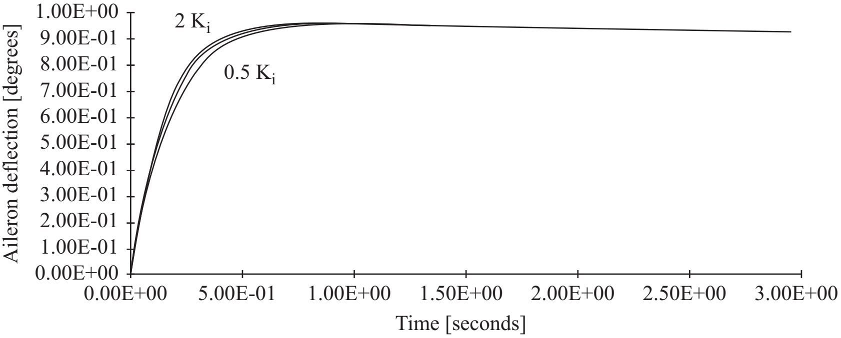

Figure 4.11 Effect of varying integral gain

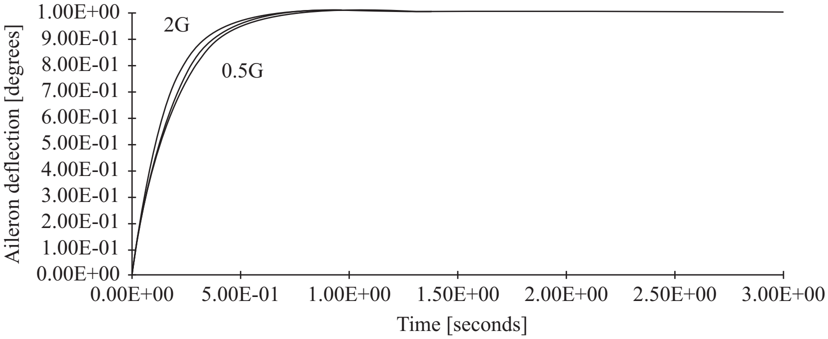

Figure 4.12 Effect of varying forward gain

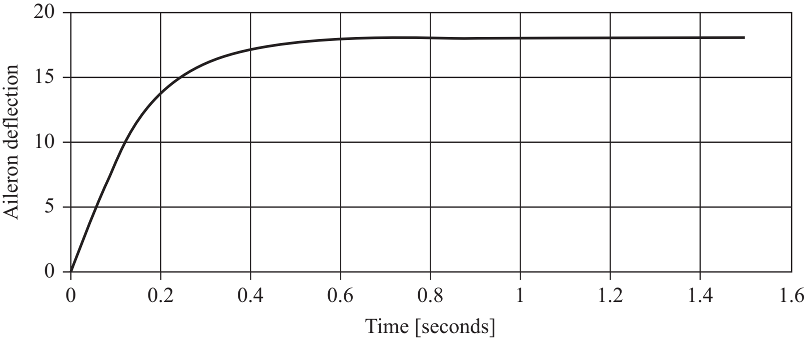

Figure 4.13 Maximum authority limit response at low aircraft speed

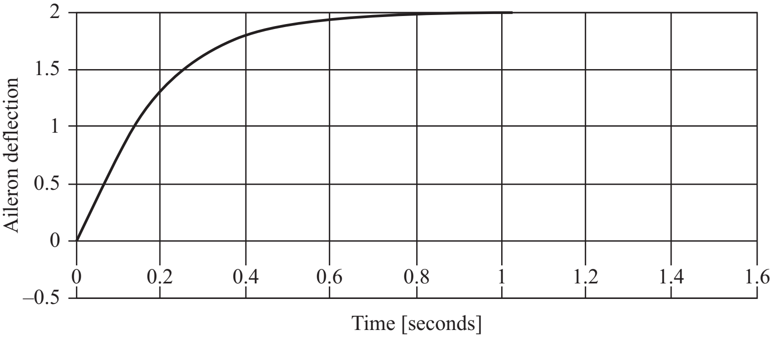

Figure 4.14 Maximum authority limit response at high aircraft speed

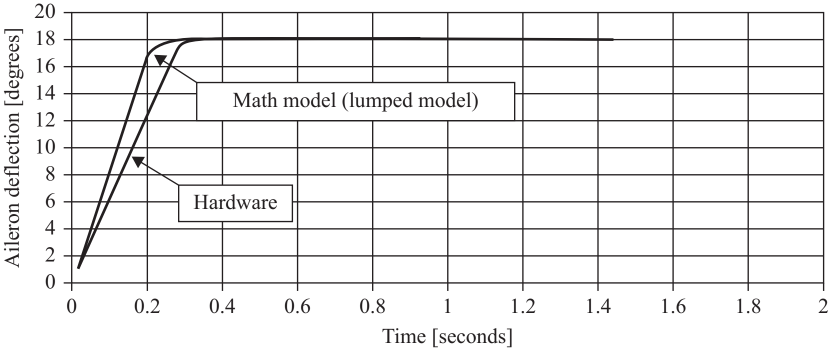

Figure 4.15 Low speed, large aileron deflection, step response

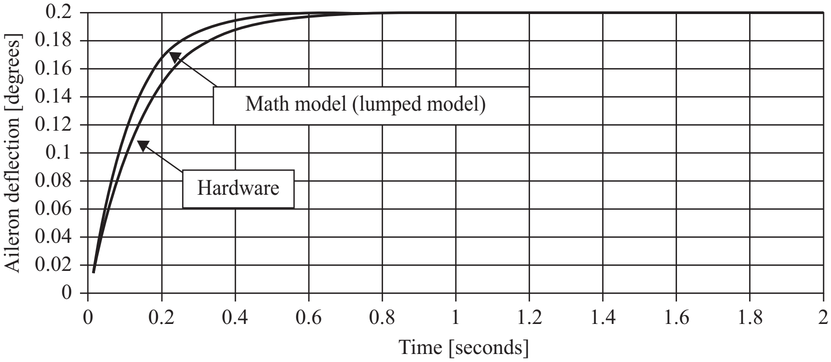

Figure 4.16 Low speed, small aileron deflection, step response

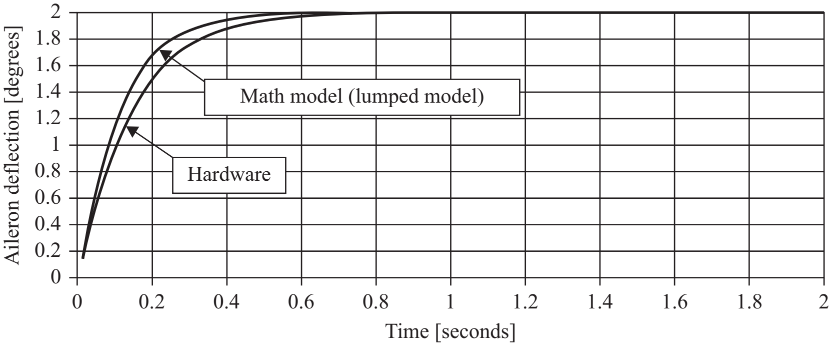

Figure 4.17 High speed, large aileron deflection, step response

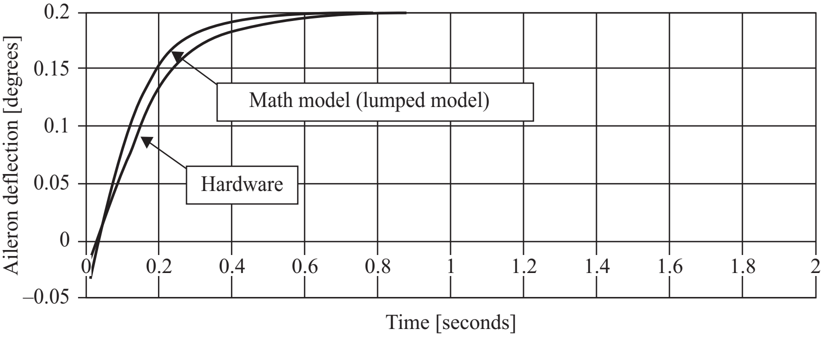

Figure 4.18 High speed, all aileron deflection, step response

4.5 The loads model

The actuator has to move a control surface similar to that of Figure 4.19. The control surface is assumed to have a mass m_a centred at distant L_a from the hinge. In this section comparison between inertial and aerodynamic loading will be conducted.

4.5.1 Inertial load contribution

The torque generated by the actuator to overcome the surface inertial torque is given by

$$T_r = J_a \ddot{\delta}_a \tag{4.15}$$

Thus, if the surface were to move sinusoidally, the anticipated torque required is given by

$$\text{Inertial Torque} = -J_a \delta_{ao} \hat{\omega}^2 \sin \hat{\omega} t \tag{4.16}$$

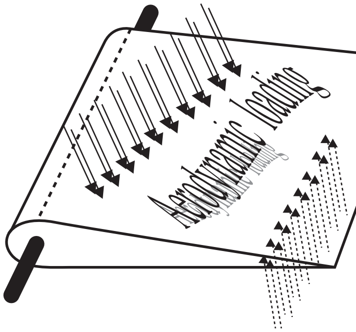

Figure 4.19 Aircraft control surface

where

δ_a is the surface angular deflection, degrees
$\ddot{\delta}_a$ is the surface angular acceleration, deg/s^2
δ_{ao} is the maximum authority limit, 18° at low aircraft speed and 2° at high aircraft speed
$\hat{\omega}$ is the maximum operating frequency$|_{\text{with 8 Hz initial bandwidth}}$

Here, the control surface was assumed to have a mass $m_a = 5$ Kg centred at a distant $L_a = 0.16$ m from the hinge. Thus, the surface inertia $J_a = m_a L_a^2 = 0.128$ Kgm^2. The anticipated peak inertial loads may be calculated using equation 4.16. To demonstrate the design, here, the actuator was assumed to drive the load at maximum frequencies of 8 Hz.

4.5.2 *The aerodynamic loading*

The aerodynamic torque load at the hinge is expressed as

$$H = \left(\frac{1}{2}\rho v^2\right) * \left(\overline{\overline{C}}_f\right)^2 * (S_f) * (C_H) \tag{4.17}$$

where

ρ is the air density
$\underline{v}$ is the aircraft speed
$\overline{\overline{C}}_f$ is the aileron chord
S_f is the aileron span
C_H is the hinge moment coefficient

The terms $\overline{\overline{C}}_f$ and S_f are constants obtained from the control surface geometry. Thus the dynamic pressure model for different aircraft speeds may be calculated using the curve fit polynomial shown in Figure 4.20 and is expressed in equation 4.18.

$$\overline{Q}(M) = \frac{1}{2}\rho v^2 = AM^5 + BM^4 + CM^3 + DM^2 + EM + F \tag{4.18}$$

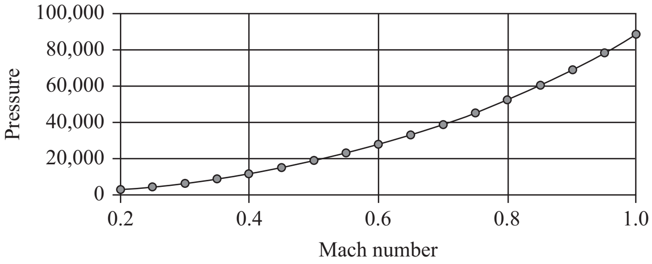

Figure 4.20 Pressure versus Mach number

where

$A = 0.6952 \times 10^4$
$B = 0.6796 \times 10^4$
$C = 0.8069 \times 10^4$
$D = 6.6305 \times 10^4$
$E = 0.0655 \times 10^4$
$F = -0.0051 \times 10^4$
Mach Number $0.2 \leq M \leq 1.0$

The hinge moment has a contribution from the steady wing lift (due to wing incidence) and from the control surface deflection. The hinge moment coefficient C_H is expressed as

$$C_H = b_1\alpha + b_2\delta_a \tag{4.19}$$

where

α is the angle of incidence of the wing
δ_a is the aileron deflection
b_l & b_2 are constants to be evaluated

Therefore, for a given angle of incidence, C_H is expressed in terms of two components, a steady component that depends on the aircraft speed and a variable component, which is a function of δ_a. The Hinge Moment H is given

$$H = \overline{Q}(M) \quad [0.151791 \quad \alpha_G + 4.3574 \times 10^{-3}\delta_a] \tag{4.20}$$

Here, the following assumptions were made:

- $c_f = 0.27c$, Aspect Ratio = 3.42, $C_L = 5094.6336/\overline{Q}(M)$, $\alpha = 1286.524/\overline{Q}(M)$, $b_1 = 0.55$, $b_2 = 0.9/57$, $\overline{\overline{C}}_f = 0.56$, and $S_f = 0.88$,
- $\delta_{a_{max}}$ and M have the linear relationship in Figure 4.21 that assumes 18° full aileron deflection at low speeds and a limited 2° at high aircraft speed. Thus, an aileron authority limit may be expressed mathematically as

$$\delta_{a_{max}} = -20M + 22 \tag{4.21}$$

- α was assumed to vary with speed, depending on the steady g-force the aircraft is experiencing, however, the incremental g-force was assumed to have the

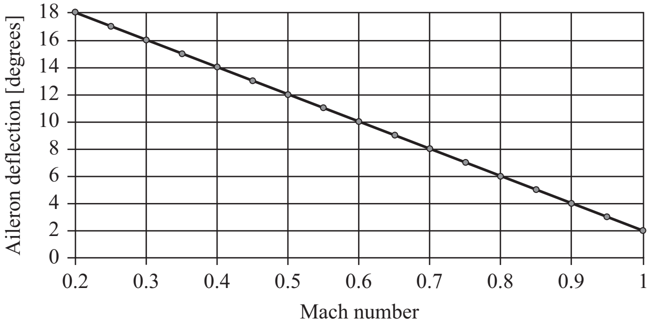

Figure 4.21 Maximum aileron deflection/Mach number

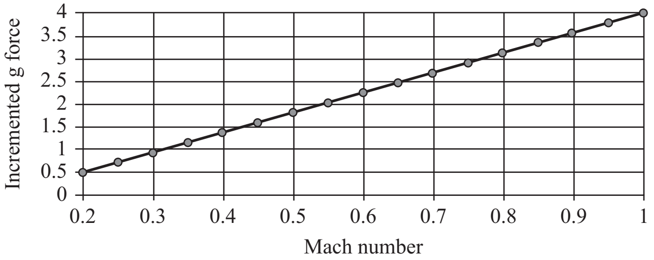

Figure 4.22 Incremental g-force vs aircraft speed

trend shown in Figure 4.22, with a maximum incremental load factor range 0.48 to 4, thus the incremental factor n_g is given by

$$n_g = 4.4M - 0.4 \tag{4.22}$$

$$\alpha_G = \alpha(1 + n_g) \text{ [radians]} \tag{4.23}$$

where α is the angle of incidence at 1g, and $\alpha_G \leq 15°$.

4.5.3 Mathematical model equations

From the discussion above the mathematical equations that describe the load model at maximum aircraft manoeuvre conditions may be summarised below as follows:

$$\text{Inertial Torque} = J_a\ddot{\delta}_a$$

$$H = \overline{Q}(M)[0.151791 \quad \alpha_G + 4.3574 \times 10^{-3}\delta_a]$$

$$\delta_{a_{max}} = -20M + 22$$

$$n_g = 4.4M - 0.4$$

$$\alpha_G = \alpha(1 + n_g)$$

$$\overline{Q}(M) = A\,M^5 + B\,M^4 + C\,M^3 + D\,M^2 + E\,M + F \tag{4.24}$$

$$\alpha = 1286.524/\overline{Q}(M) \tag{4.25}$$

$$C_H = 0.55\alpha_G + 0.9\delta_a/57 \tag{4.26}$$

The actuator must be designed to drive the load adequately after two failures.

4.5.4 Simulated load torques

Table 4.4 lists the assumed relationship between M, $\frac{1}{2}\rho v^2$, δ_a, g-force and (static and variable components) aerodynamic load. The variable component is a function of aileron deflection, the steady component is a function of the wing angle of incidence, and both components depend on the aircraft speed only and are independent of aileron movement frequency. In this study, the maximum variable component was found to occur at $M = 0.8$, but this does not mean that it is the highest loading case.

Tables 4.5 and 4.6 list the peak inertial and resultant loads respectively. The inertial loads were found to vary between 10 and 5821 Nm, depending on the aircraft speed and aileron sinusoidal frequency. The variable component acts with or against the inertial load depending on the aileron direction of motion. The steady component is constant over the two aileron surfaces. Therefore, in one direction it will be assisting the inertial load (opposing the variable component) and in the other direction it will be opposing the inertial load (assisting the variable component). Clearly, the resultant load depends on the inertial and variable

Table 4.4 Relations between M, $\overline{\mathrm{Q}}(\mathrm{M})$, δ_a *and g-force and aerodynamic loads*

Mach number	$\overline{\mathbf{Q}}$**(M)**	δ_a	**G-force**	**Aerodynamic components**	
				Variable	**Steady**
0.20	2811	18.0	0.48	219	112
0.30	6402	16.0	0.92	444	254
0.40	11582	14.0	1.36	703	460
0.50	18503	12.0	1.80	963	547
0.60	27375	10.0	2.24	1187	633
0.70	38465	8.00	2.68	1334	719
0.80	52102	6.00	3.12	1355	805
0.90	68692	4.00	3.56	1191	890
1.00	88727	2.00	4.00	769	976

Table 4.5 Inertial loading

Frequency	**Mach number**								
	0.2	**0.3**	**0.4**	**0.5**	**0.6**	**0.7**	**0.8**	**0.9**	**1.0**
1	91	81	71	61	51	40	30	20	10
2	364	323	283	243	202	162	121	81	40
3	819	728	637	546	455	364	273	182	91
4	1455	1294	1132	970	808	647	485	323	162
5	2274	2021	1769	1516	1263	1011	758	505	253
6	3274	2911	2547	2183	1819	1455	1091	728	364
7	4457	3962	3467	2971	2476	1981	1486	990	495
8	5821	5174	4527	3881	3234	2587	1940	1294	647

Table 4.6 Resultant loading

Frequency	Mach number								
	0.2	**0.3**	**0.4**	**0.5**	**0.6**	**0.7**	**0.8**	**0.9**	**1.0**
1	240	618	1092	1449	1769	2012	2129	2061	1735
2	256	375	880	1267	1617	1891	2038	2001	1705
3	711	538	526	964	1365	1689	1887	1900	1655
4	1348	1104	889	554	1011	1406	1674	1758	1584
5	2166	1832	1526	1100	709	1042	1402	1576	1493
6	3167	2721	2304	1767	1265	840	1068	1354	1382
7	4349	3772	3224	2556	1922	1366	935	1091	1250
8	5713	4984	4285	3465	2680	1972	1390	993	1099

component values, and it acts in the direction of the one that has greater value. Table 4.6 tabulates these torques and shows that a maximum loading condition occurs when the aileron is driven at 8 Hz with amplitudes of $\delta_a = \pm 18^\circ$ during low aircraft speeds. The resultant torque at this point is 5713 Nm, thus the actuator should be designed so that each lane drives a load of 2856 Nm.

4.6 Gearbox ratio selection

A gearbox may be thought of as a torque transformer, therefore, a reduction gearbox type with its input shaft driven at high speed and low torque produces low speed and high torque at its output shaft, and vice versa. The choice of gear ratio depends on output load, and if the load is constant, then choosing the gear ratio is simply achieved by matching the load torque T_L to the rated continuous motor torque T_{mc}, i.e. $N = T_L/T_{mc}$. If, however, the load is dynamically changing with specific profile of speed or position as a function of time, the gear ratio choice is more complicated and will fall in one of several categories [26]. Here, the load nature is that of an accelerated inertia with fixed load torque.

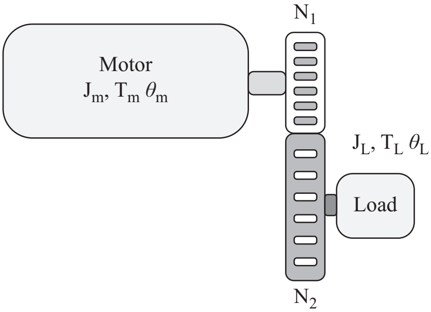

Figure 4.23 Motor-load coupling via a gearbox

With reference to Figure 4.23, and assuming that a motor (with inertia J_m) is rotated by angle θ_m producing a torque T_m, so that it rotates a load (inertia J_L) by angle θ_L via a gearbox (ratio $N = N_1/N_2$), the load acceleration is given by

$$\ddot{\theta}_L = \frac{NT_m - N^2T_L}{J_m + N^2J_L} \tag{4.27}$$

where

$\ddot{\theta}_L$ is the load acceleration, $T_L \neq 0$
J_L and J_m are the load and motor inertia
T_m and T_L are the motor and load torques

Chapter 5

Architecture consolidation

Fly-by-wire systems pose difficult problems as they have to be designed to survive failures. This includes aircraft control surface actuators, which are commonly found to have up to four lanes of parallel first stage hydraulic actuation system that drives a duplicated or triplicated hydraulic second power stage. For electromechanical actuators to be accepted alternatives, they should be designed so that they meet the current safety requirements and performance of current hydraulic actuators.

This chapter introduces methods in achieving high integrity in the design of electric actuators, such as:

- Output consolidation in multi-lane actuators.
- Fault Detection and Fault Isolation (FDI) system with embedded monitoring devices that conduct fault monitoring, voting, detection and isolation.
- Two consolidation architectures and their associated FDI systems, namely, torque and velocity summing.
- A Simulation Graphical Monte Carlo (SGMC) method as a threshold setting technique.
- Lumped and three-phase lane models.

5.1 Architecture consolidation

The reliability and redundancy study in [4] states that the likely acceptable architecture configuration of a multi-lane electromechanical actuator would be quadruplex (four motor) design. The actuator is to retain performance following the first failure and has a degraded performance (get home capability) following the second failure (i.e. with two motors operating).

Possible outputs consolidation methods can be either in uniform or combined summing architectures. Uniform summing utilises one summing type throughout the multiple stages of summing, however, combined summing utilises more than one type of summing throughout the multiple summing stages. Here, uniform summing will be considered only. Figure 5.1 shows the basic types of velocity and torque summing in mechanical and electromechanical systems. Each type of architecture has its advantages and disadvantages and hence the utilisation of one technique or another depends on the application and the system response to failures.

5.1.1 Velocity summing

In this architecture, the output position is the average of the individual lanes displacements contributions. The basic concept of this configuration is illustrated using the two-lane hydraulic actuator shown in Figure 5.1. Here, the output position at any time, P(t), is the average of the two lanes displacements $P_1(t)$ and $P_2(t)$. In the multi-lane actuator, this could be achieved by summing the lanes to a common output shaft via a differential gearbox.

This architecture has the advantage of eliminating any force fight between the contributing lanes. When one lane fails (it stops completely or it speeds up or down), the remaining lanes will compensate for the failure accordingly (accelerating or decelerating) to maintain a constant speed at the output. Position or speed compensation by the other lanes will continue until the failure is detected and the faulty lane is identified. Once the faulty lane is identified, it is isolated by switching off the drive currents and brakes are activated to lock the faulty lane. The disadvantage of this architecture is the possibility of gradual speed run away, where a lane fails at a slow rate.

5.1.2 Torque summing (torque-torque summing)

The output torque is the algebraic sum of the individual-lane torques. This configuration is similar to that of the two-lane hydraulic actuator shown in Figure 5.1, where the output shaft torque T(t) is the sum of the two torques $T_1(t)$ and $T_2(t)$.

In the multi-lane electromechanical actuator, the lanes are locked together via a gearbox to a common output shaft. Although this technique has the advantage of eliminating the problem of gradual speed run away, it has the disadvantage of the possibility of force fighting between mismatched lanes. This effect could be minimised to a large extent by providing a common input driving signal to the lanes. This signal is usually the average value of the individual motors signals.

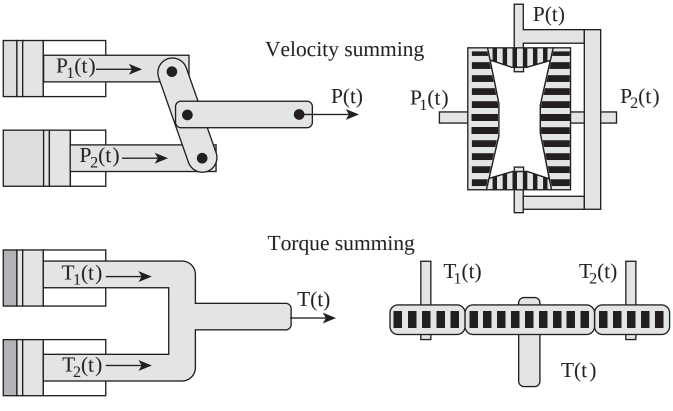

(a) Hydraulic **(b) Mechanical**

Figure 5.1 Basic types of architecture consolidation

In this architecture, it is essential to include clutches to mechanically disconnect faulty lanes, once a failure is detected and the faulty lane is isolated, otherwise the faulty lane will appear as an inertial load to the other lanes.

5.1.3 Combined summing

Other possible architectures are to use different architecture at different stages, where the system has the advantages and the disadvantages of both velocity and torque summing. Therefore, combined architectures should include both brakes and clutches to ensure complete isolation of faulty lanes.

5.2 Fault detection and fault isolation (FDI) system

The FDI system plays an important part in safety critical applications such as electromechanical actuation system in military aircraft, where failures result in failure transients affecting the aircraft motion. In the multi-lane actuator, the FDI system has the basic function of registering and identifying abnormal condition, thus it is the inclusion of this system that will make the actuator smart. The effectiveness of a FDI system could be assessed by examining its detection promptness, sensitivity to incipient faults and the rate of false alarms, missed fault detection and incorrect fault identification [27].

A binary response is normally desired, where the detection system declares whether a component has failed or not. An intermediate declaration of perhaps is not useful to correct or eliminate a fault. Imposed faults that induce no response from the detection system are termed as missed detections, which may be acceptable for inconsequential faults. An example of such a fault could well be a very small bias on the signal from a relatively unimportant sensor. It would, on the other hand, be quite unacceptable if the fault had a serious impact on the operation of the monitored system. Not all faults occur suddenly or persist; when they do occur, therefore, slow developing or small faults (incipient faults) due to drift in instrumentation or intermittent faults can be assessed in a different way. Assuming that a fault is detected successfully, the issue of promptness may be of vital importance in some systems, where it is desirable to detect small or slowly developing (incipient) faults. This is important in fault detection schemes intended to enhance maintenance operations in plants for early detection of worn equipment. Here, promptness in detection is secondary in importance to sensitivity. In other systems, sensitivity and promptness may both be required. Thus, this clearly leads to more complex detection schemes, possibly requiring both hardware and analytical redundancy.

False alarms are generally indicative of poor performance in a fault detection scheme, and even a small false alarm rate is unacceptable because it quickly leads to a lack of confidence in the detection system. However, a detection system that has an acceptable false alarm rate during normal operation might register a false alarm when the monitored plant undergoes an unusual excursion, and this might be acceptable in some applications. In other applications small faults may be so serious that it is preferable to react to false alarms (replacing unfailed components) than to suffer deteriorated performance from an undetected (though small) fault. Compromises in detection system design among false alarm rate, sensitivity to incipient faults and promptness in detection are difficult to make because they require extensive knowledge of the working environment and an explicit understanding of the vital performance criteria of the monitored system.

Another malfunction that is closely related to both false alarms and missed detections is the incorrect identification of a failed component. In this case, the detection system correctly registers that a fault has occurred but incorrectly identifies the failed component. The reconfiguration system that proceeds to compensate for the wrong fault could produce consequences as serious as a missed detection.

5.2.1 FDI system requirements in the multi-lane actuator

In the multi-lane actuator, failures will introduce failure transients that will result in an aircraft roll rate response and hence a change in the bank angle. To minimise the roll disturbance, the dedicated FDI system should have the capability of promptly detecting and isolating failed components or lane. Also, the FDI system should be designed so that false alarm rates are minimal. Failure detection promptness, failure isolation and the rate of false alarms are functions of the thresholds on the Monitoring Voting Averaging Devices (MVADs). As will be explained later on, in this particular application the thresholds depend on lanes disparities and flight condition, where the first are due to the inherent random variations in parameters and random fluctuation in transducer readings.

5.2.2 The monitoring voting averaging device (MVADs)

There are many different approaches to monitoring in multi-lane systems to detect failures, and many ways in which signals or values are outputted to the next stage of the system. The simplest approach to monitoring is cross monitoring, where paired lanes are compared and logic is used to decide on the failed lane. Output consolidation can be implemented by simple averaging, master–slave equalisation, median selection or other related schemes. Here, an initial simple design will implement cross monitoring and lane averaging.

The monitoring, voting and averaging tasks can be separated: monitoring is a combination of mathematical and logical functions, voting is purely logical and averaging is purely mathematical. In both architectures, these devices monitor position and velocity feedback sensors, motor currents, as well as, inputs to drive chips. These devices provide output average feedback and control signals.

Figure 5.2 is a block diagram of the proposed MVAD, with four inputs. Regardless of the source of the input signals, each MVAD will perform the same tasks. If the input signals are S_1, S_2, S_3 and S_4, then the MVAD first calculates the difference between all the signals, producing D_{12}, D_{13}, D_{14}, D_{23}, D_{24} and D_{34}, where, $D_{12} = S_1 - S_2$, $D_{13} = S_1 - S_3$, $D_{14} = S_1 - S_4$, $D_{23} = S_2 - S_3$, $D_{24} = S_2 - S_4$ and $D_{34} = S_3 - S_4$.

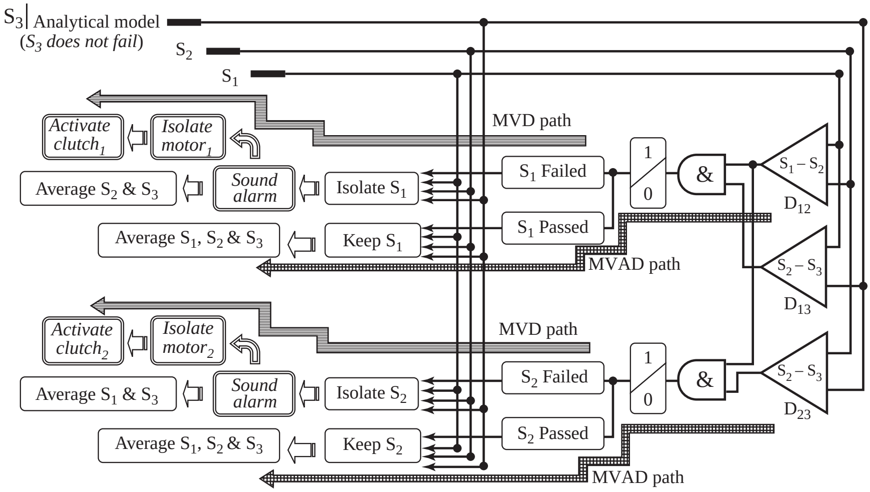

Figure 5.2 Block diagram of the MVAD scheme implemented in the FDI system

These differences are compared against predefined thresholds. If their values were to exceed the threshold then the common input signal will be identified as a failed signal. For example, if the signal S_1 were to be declared as a failing signal, then D_{12}, D_{13} and D_{14} have to exceed the predefined threshold value. Similarly, if S_3 were to be declared as failing signal, then D_{13}, D_{23} and D_{34} have to exceed the predefined threshold value.

In some designs the differences may be smoothed to reduce the effects of noise while in others a delay (of a few computing cycles) is allowed before the failure is permanently identified. This was not implemented in the current design, and failures were intentionally introduced and allowed to grow in a ramp fashion to explore the worst failure effects, except for motor failures, which were introduced suddenly to the system.

Once the channels have been scanned for failures, two actions take place. The first isolates the source of the failed signal. If the source is a potentiometer or a tachometer, then the failed component is isolated, however, if the failure is due to a motor failure, then the entire channel is isolated and the clutches or brakes are activated. The second action evaluates position and rate feedback signal, by taking the average of the active signals. For example, if S_1 suddenly develops an error and differed from the other signals by Δ_{S_1}, other signals decreases by Δ_S accordingly, so that a constant average signal S_{Avg} is maintained to keep a closed loop situation constant. Thus

$$S_{Avg} = [(S_1 \pm \Delta_{S_1}) + (S_2 \mp \Delta_S) + (S_3 \mp \Delta_S) + (S_4 \mp \Delta_S)]/4 \tag{5.1}$$

$$\text{Since} \quad S_{Avg} \text{ remains constant, therefore, } \Delta_{S_1} = \Delta_S/3 \tag{5.2}$$

Equation 5.2 reveals that the other signals reduce their values by one-third the magnitude of the failure. In general if $\Delta_{S_{pq}}$ is an error signal (where p and q are lane numbers between 1 and 4, and $p \neq q$), and S_{TD} is the threshold value, then there will be an alarm if $\Delta_{S_{pq}} > S_{TD}$. The MVAD modelling should also take into account changes in inertial load distributions following channels isolation.

5.3 Architecture consolidation

In the previous sections the different possible configurations of lane consolidation along with the FDI system were described. This section will describe the two architecture configurations of velocity summing and torque summing, along the associated FDI system.

5.3.1 Velocity summing architecture

Figure 5.3 shows the velocity summed architecture, where the outputs of the individual lanes are summed via a differential gearbox. The figure illustrates the location of the MVADs used in this architecture. With reference to Figures 5.2 and 5.3, the following practical observations are made:

- Here, it is assumed that all potentiometers are mounted on the common output shaft, therefore, they measure the actuator output angular displacement. Unlike the torque summing, in this architecture, the position of these devices is crucial, as placement before the summing differential gearbox would results in individual lanes angular displacement measurements. Position feedback to the control system is the average value of active potentiometers readings.
- Similarly, tachometers are also mounted on the individual-lane shafts, thus their measurements represent the angular speeds of individual lanes. On one hand, the motors built in tachometers can be used and there will be no need to implement extra tachometers. However, on the other hand, there will be an immediate reduction in speed feedback signals redundancy once a lane is isolated.
- The average values of the measured angular positions and speeds provide position and velocity feedback to the control system, and represent the position and speed of the common output shaft.
- Failures in any of the potentiometer or tachometer feedback sensors will result in isolation of that particular measuring device, and feedback signals will be the average of the remaining active sensors.
- Motors (and their drives) are also monitored by the MVAD, where a failure will result in the isolation of the entire affected lane and the activation of the brake to avoid speed compensation by the other lanes. This could be explained by considering the case where a lane failure was not possible to be isolated. One possibility is that the failed lane will be driven at full speed in a direction similar to that of the remaining lanes. This will result in speed reduction of the remaining lanes and may be even direction reversal to maintain control. However, if the failure resulted in driving the motor full speed and in an

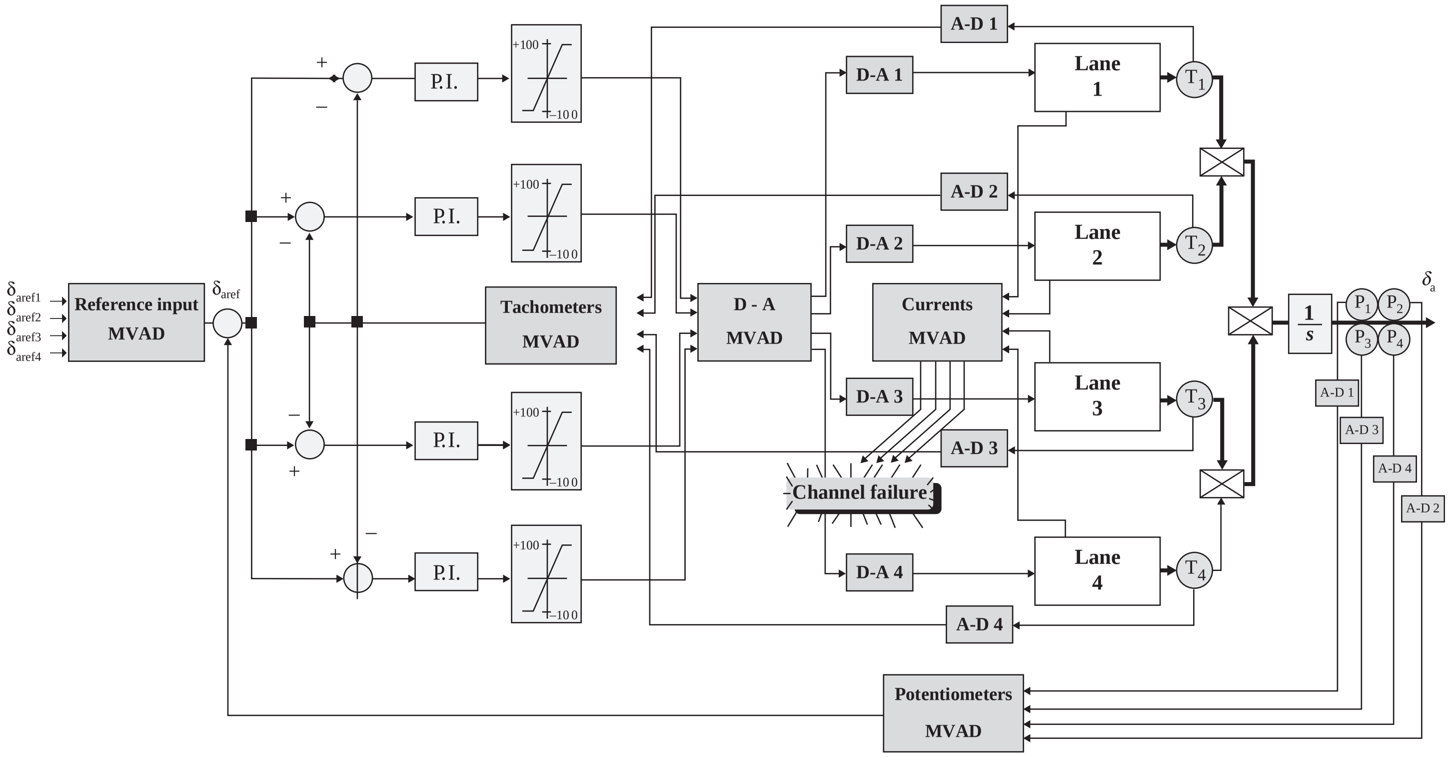

Figure 5.3 Velocity summing architecture

opposite direction to the remaining lanes, then these lanes will have to run faster to maintain control. As mentioned above, lane isolation will result in an accompanying loss of built in feedback sensors.
- Lanes equalisation may be implemented by providing a common driving signal to the motors.

5.3.2 Torque summing architecture

Figure 5.4 shows the torque summed architecture, where the outputs of the individual lanes are locked together via a torque summing gearbox. The figure illustrates the location of the MVADs used in this architecture. With reference to Figures 5.2 and 5.4, the following practical observations are made:

- It is assumed that all potentiometers and tachometers are to be mounted on the common output shaft, thus, their readings represent measurements of the actuator angular displacement and velocity. In this design the readings provide the feedback signals in the control system, which is the average value of the active measurements.
- Since individual and output shafts are locked together, it is irrelevant where the feedback sensors are placed. Although, built-in motors encoders provide better signals, there will be a measurement loss following lane isolation. In this particular design this limitation is eliminated as external encoders were placed on the common output shaft.
- Failure logic ensures that failures in any of the feedback sensors would result in isolation of that particular sensor. The utilised feedback signals are the averages of measurements provided by the remaining active sensors.
- The motors are also monitored by the MVAD, and once excessive currents are detected, the entire affected lane is isolated and a clutch (in the active path) will be activated, otherwise the isolated motor will appear as an external inertial load to the other active lanes. Also, a back-driven failed motor will act as a generator and would result in heat generation when a load is connected across it.
- To minimise force fight between mismatched lanes, lanes equalisation is essential in this architecture, thus a common signal feeds the motor drives, as shown in Figure 5.4.

5.3.3 Initial simulation results

When considering feedback transducers failures, step or hard-over failures will be detected quickly and will not result in any significant transients. However, slow ramp failures allow the presence of output disturbance for some time before the thresholds are crossed.

Here, in both architectures, failures in feedback transducers were introduced at time $t = 2$ s (after the actuator has responded to a step input command equivalent to the maximum authority limit of 18° at low aircraft speed). The failures were allowed to grow in a ramp fashion and the readings of failed component, the

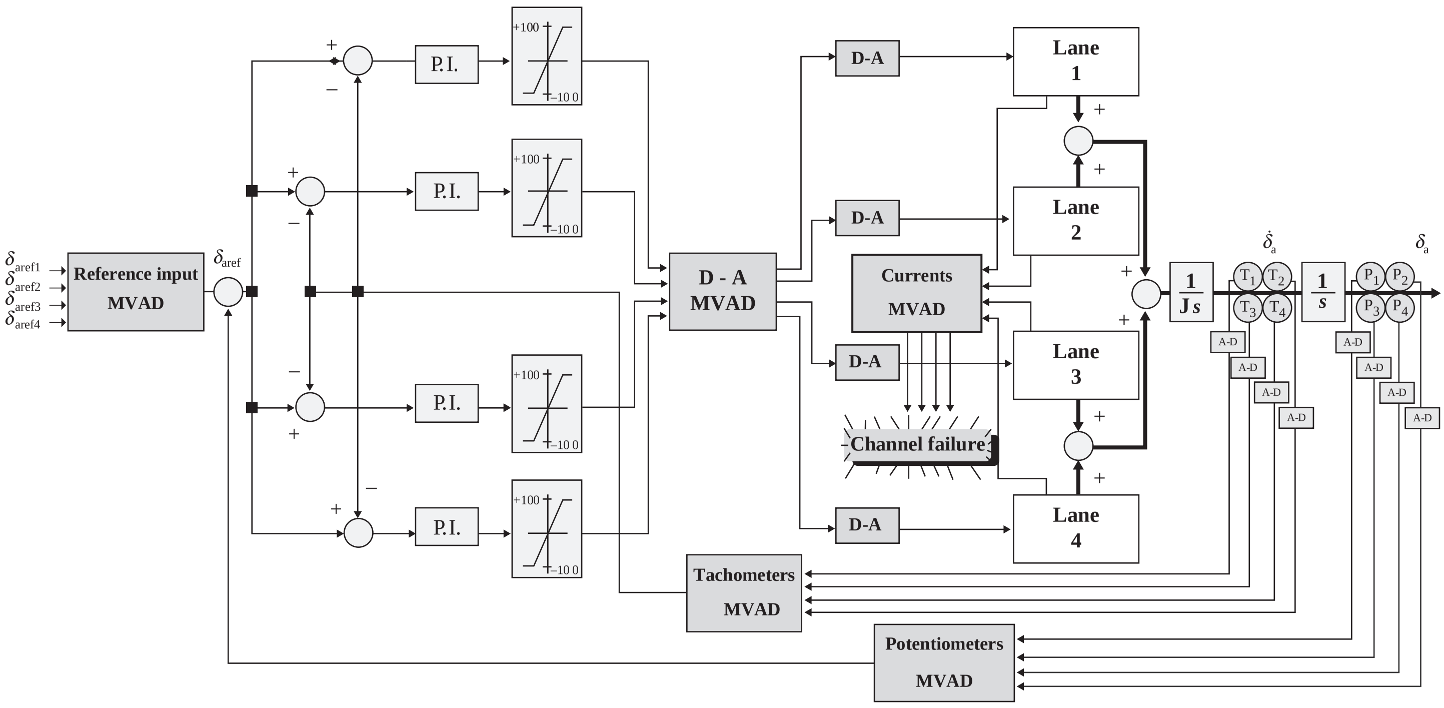

Figure 5.4 Torque summing architecture

average signal from the MVAD and the true reading on the actuator shaft (or other lanes) were observed, as shown in Figures 5.5 and 5.6.

Figures 5.5 shows the response to a potentiometer failure that was introduced at 2 s and it is marked as ‘Failed Pot’. Since the signals from the potentiometers are always averaged, the control system will interpret this failure as a constant over travelling, therefore, the lanes will react by decelerating sharply to a constant speed to maintain control. The figure also shows the way in which ‘Other Lanes’ compensate for this failure to keep the averaged value maintained at 18° all the time.

Similarly, Figure 5.6 shows the response when a tachometer fails at time $t = 2$ s, marked as *Failed tachometer*. In this test, the averaged velocity feedback signal (marked as *Average Reading*) is fed back in the control system and the MVAD will interpret this failure as constant over speeding. Therefore, the result will be a decrease in individual lanes and actuator speeds, and a resultant decrease in the output angular displacement.

Chip failures are introduced in a step fashion and will be considered in a later stage.

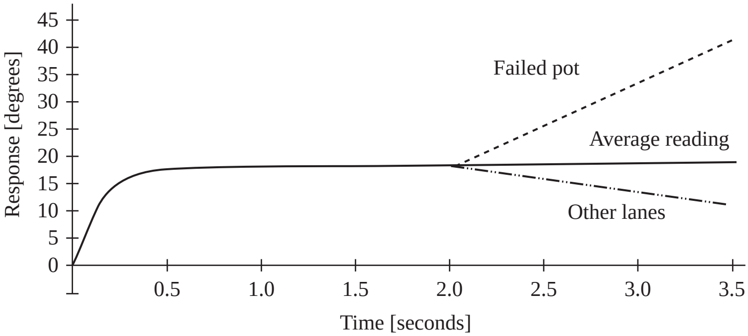

Figure 5.5 Position response to potentiometer failure

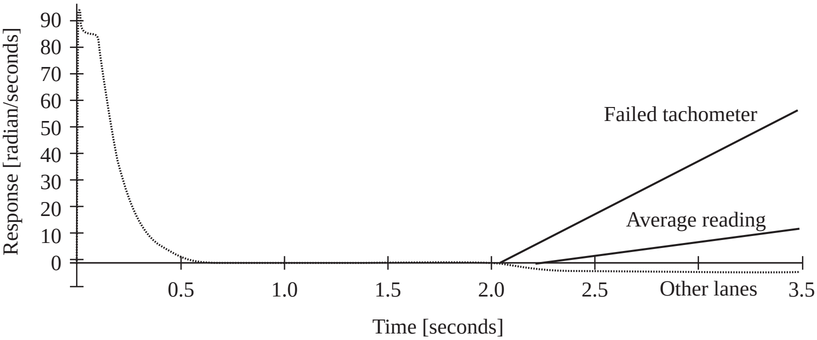

Figure 5.6 Speed response to tachometer failure

5.4 Mismatch between lanes

Another important concept in electromechanical actuation design is the fact that there will always be mismatch between the individual driving lanes. The consequence of this effect is worst in torque summing architecture, where it will lead to the possibility of force fight between mismatched lanes. By adopting good design techniques (such as the inclusion of MVADs), the effect could be reduced so that the most pessimistic case will possibly result in small *dead-zone* regions at low output impedance.

In some applications, the effect of force fight between mismatched lanes could be even highlighted more at regions where the lanes have to provide maximum torques. In the multi-lane actuator case, these regions are where the aerodynamic load is zero. This is because the steady component of the aerodynamic load cancels the variable component at a specific angle of aileron deflection, as shown in Figure 5.7. Thus, the load will be purely inertial and when high frequency fluttering takes place the loads will be maximum. One example is that during low aircraft speed, the angle at which this cancellation take place $\delta_a|_{M=0.2} = -9°$. Thus, designs should be assessed at these regions, with maximum mismatch between lanes. The mismatch is naturally due to variation in lanes parameters and tolerances in feedback sensors.

5.5 A simulation-graphical Monte Carlo thresholds setting method

It is practically impossible to use identical components or feedback transducers, however, depending on the effects of deviations on the overall system behaviour, it is possible to match components with some degree of certainty at the expense of the

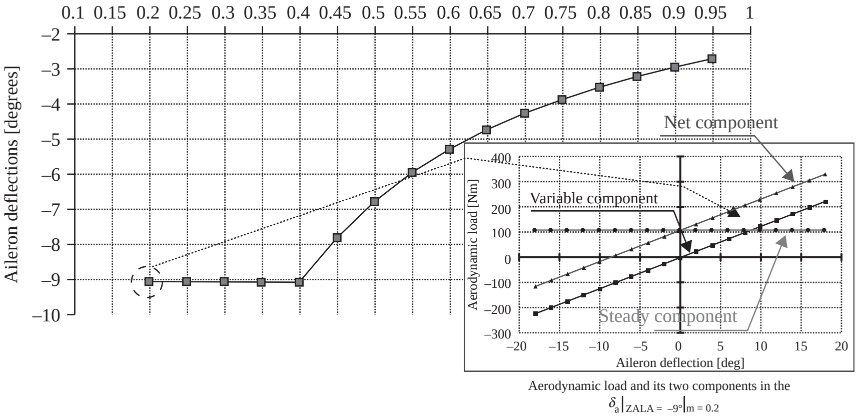

Figure 5.7 Zero aerodynamic load angles regions, with the aerodynamic load and its two components

overall system cost. A system with closely matched components will be more expensive, but it will possess a FDI with lower thresholds. Similarly, a system with poorly matched components will be less expensive with higher thresholds, and thus has a possible poorer overall performance. Therefore, distributions, confidence levels and randomness in components values variations affect the lanes disparities and make the task of threshold setting more complicated. This puts more demand on the FDI design and on the threshold setting technique. Aircraft applications demand a FDI system with a maximum false alarm rate of 1.0E-4. In this book, a SGMC threshold setting technique will be used to calculate the thresholds on the FDI system.

5.5.1 Advantages over other methods

Historical development of Monte Carlo methods along with mathematical background of some relevant Monte Carlo methods can be found in the literature [28–36]. The suitability of this technique compared to Hypothesis Testing (Decision Theory) and Analysis of Variance can be summarised as follows:

***Hypothesis Testing*:** This technique requires knowledge of:

- Distribution of observations in presence or absence of failures.
- Prior probabilities, in presence and absence of failures.
- Cost functions for correct and incorrect decisions.

***Analysis of Variance, ANOVA*:** Problems treated with this method could be set up in different forms depending on the number of control parameters. In quality control, the ANOVA is used to improve cost or efficiency of a particular system by considering different tolerances on randomly varying control parameters. In the multi-lane actuator system, the control parameters could be reduced to the aileron deflection at a specific aircraft speed (for a given set of servos and feedback transducers). Thus, the simplest form of this method is the no-way ANOVA, which does not consider any control parameters. Other higher forms may be conducted depending on the number of control parameters. Regardless of the form used, the method has the following limitations:

- ANOVA methods are linked with the analysis of purely experimental observations, thus the confidence level depends on the confidence level in which the data was obtained. This could be improved by increasing the sample size.
- The complexity of this method is directly related to the number of control parameters associated with the problem.

The proposed Monte Carlo does not suffer from any of the above disadvantages and has the following advantages:

- It can be used with the same ease of application to any distribution and any finite region. The effect of the combination of multi-dimensional variously shaped distributions could easily be handled by the Monte Carlo method, where the domain of the independent variables is represented by *stratified unit d-dimensional square distributions*.

- A simulation-graphical approach is more efficient and utilises small sample simulation tests to calculate peak lane disparities before evaluating the threshold values graphically. To achieve similar degree of accuracy in the ANOVA, much larger samples are required.

5.5.2 Description of the simulation graphical Monte Carlo (SGMC) method

Multi-lane electromechanical systems usually exhibit inherent disparities even in the absence of failures. Generally speaking, most are not linear and include key components with tolerance distributions that are not necessarily Gaussian. Correct setting of the thresholds is critical; if they were to be set too small, then the false alarms or nuisance disconnects will increase; whereas if they were to be set too large, then failures can cause large amplitude disturbances that could affect the systems stability and might even result in structural damages or failures.

In the electromechanical actuation system, although motor parameters and feedback sensors were assumed to randomly vary in a Gaussian distribution, the distribution of the resulting Lane-Disparities 'Δ' is difficult to predict. To continuously observe these Lane-Disparities, Ω simulations tests per flight case were randomly generated. The Peak Lane Disparities (Δ_{Peak}) were measured as the actuator responded to step input commands equivalent to maximum authority limits in different flight cases.

Thus there are three data-banks (Ω in size per flight case) of Δ_{Peak} in potentiometer, tachometer and current readings. If scheduled threshold setting is adapted, then sets of data-banks that include these maxima (as the aircraft speed and the aileron deflection are varied) are considered. If the thresholds were to be unscheduled, then only the data-bank that includes the maxima for all flight cases should be selected for calculating the thresholds.

To explain this further, let's assume that we are testing for low and high aircraft speeds only, i.e. $\text{M} = 0.2$ and $\text{M} = 1$. Let's also assume that we will be testing for maximum, mid range and small deflections only, in each flight case. Therefore, in total, there will be six tests: three for low aircraft speed ($\delta_{\text{a}}|_{\text{M}=0.2} = 0.2°$, $9°$ and $18°$); and three for high aircraft speeds (i.e. $\delta_{\text{a}}|_{\text{M}=1} = 0.2°$, $1°$ and $2°$), where $18°$ and $2°$ are the maximum authority limits for the electromechanical actuator at low and high aircraft speeds, respectively. Therefore, in total there will be six data-banks, one per flight case and may be written as $\Omega_{\delta_{\text{a,M}}}$. In each sample, Lane Disparities in potentiometer, tachometers and motor currents will be monitored and the peak three values will be selected. Therefore, there will be a total of nine peaks disparities: three in pots ($\Delta_{\text{PeakPot}}|\delta_{\text{a,M}}$); three in tachometers ($\Delta_{\text{PeakTacho}}|\delta_{\text{a,M}}$) and three in currents ($\Delta_{\text{PeakCurrent}}|\delta_{\text{a,M}}$). To calculate the threshold value, samples (nine in total) containing these peaks are identified, and the SGMC method is utilised to calculate the scheduled thresholds.

If unscheduled threshold setting is adopted, then the maximum three should be considered, i.e. one for Potentiometer, one for tachometer and one for current monitoring. Of course here, only a nine flight case scenario is assumed, however, in reality global or unscheduled threshold setting will cater for uncountable flight cases.

Having identified the sets that include peak lane disparities, the SGMC method may be applied by following these steps:

- The range over which the data-bank spreads over is divided into intervals.
- Count of the number of events that fall within an interval is observed.
- The cumulative sum over the whole range is then obtained.
- The percentage probability (%Pro) of occurrence is then calculated

$$\%\mathrm{Pro} = 100\,\frac{\text{Cummulative Sum}}{\text{Sample Size}} \qquad\qquad \mathrm{PP}_1 \leq \%\mathrm{Pro} \leq \mathrm{PP}_\mathrm{i}$$

  where PP_1 is the probability of occurance within the 1st interval ≥ 0, and PP_i is the probability of occurrence in the last interval $\cong 100$
- These probabilities are then plotted on probability graph paper (Figure 5.8) with the x-axis representing the percentage probability and the y-axis being the upper interval limit axis.
- The plotted data are then fitted with a graph.
- The graph is then extrapolated to intersect with the y-axis, where the point of intersection marks the maximum lane disparity, which has an occurrence probability of 1.0E-4. The graph fitted to the points will be very close to a straight line if the percentage probabilities are normally distributed. Even with non-linear systems having non-Gaussian probability distributions, a smooth curve is expected, which is then extrapolated to intersect the required false alarm rate probability ordinate.

This technique requires a relatively small sample of simulation tests, in comparison to a simulation-based ANOVA or a purely simulation-based Monte Carlo.

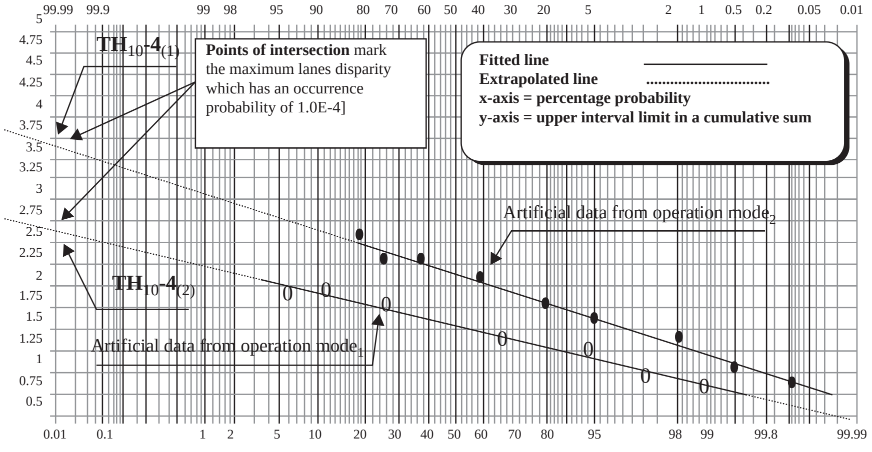

Points of intersection mark the maximum lanes disparity which has an occurrence probability of 1.0E-4]

Figure 5.8 Mean lane disparities $\Omega_{18^\circ,0.2}$ example

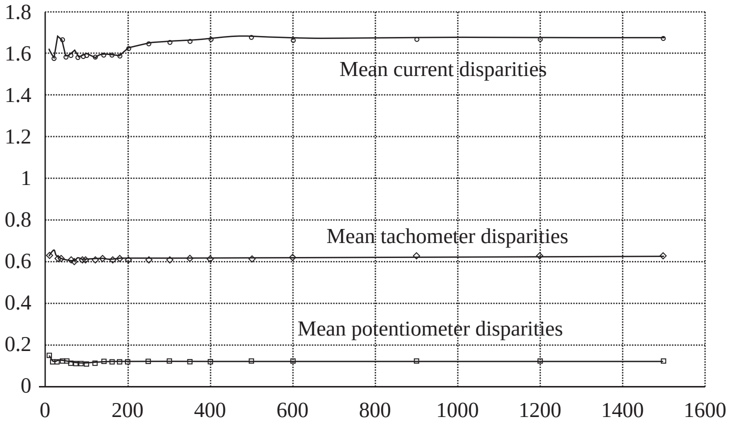

Figure 5.9 Mean lane disparities $\Omega_{18^\circ,0.2}$ *example*

5.5.3 Sample size and confidence

It is difficult to estimate the sample size or the number of simulation tests that covers all probable events that might occur in a real system. It is also difficult to be confident about the shape of the distribution. Naturally, the larger the sample is, the more accurate the representation, however, there will always be an error and events can only be predicted within certain confidence levels.

To achieve a confidence level of 99 per cent, say, then 99 per cent of the time the events will occur in the range $\mu \pm z_c\sigma$, where μ is the mean and σ is the standard deviation. For a known standard deviation and error confidence ε, an estimate of the sample size is given by $\varphi = [\{\mu \pm z_c\sigma\}/\varepsilon]^2$ [37].

Alternatively, a graphical approach could be utilised to determine the sample size by plotting the mean and the standard deviation versus the sample size. Acceptable sample size is identified at points where fluctuations in μ or σ are considered minimal. This approach is inefficient and time consuming, but once the sample size is identified, unnecessary simulation time will be saved.

Figure 5.9 is an example of means disparities in potentiometer, tachometer and current readings for the $\Omega_{18^\circ,0.2}$ flight case in the torque summed architectures, where it clearly reveals the initial fluctuation in small samples before converging to a steady value as the sample size is increased. Thus, in the multi-lane actuator, a sample of 1500 tests was considered sufficient for an accurate representation.

In the next chapters this approach will be implemented in hardware and digital cross monitoring.

Chapter 6

Hardware cross monitoring

Fault tolerance is achieved through hardware redundancy in repeated hardware elements to provide protection against localised damage in safety-critical systems. Examples of such systems include aircraft, space vehicles, nuclear power plants and plants handling dangerous chemicals. One method in achieving fault detection and fault isolation is through hardware cross monitoring, where the performance of the repeated components is continuously assessed and compared. This technique is simple to apply and is widely used. The drawbacks include the extra hardware cost and the additional space required to accommodate the duplicated equipment.

In this chapter, this technique will be presented to calculate the threshold values on a multi-lane actuator in torque and velocity summed architectures. The brushless dc motors in both architectures will be represented by their lumped models. The FDI system (discussed in Chapter 5) will be implemented to monitor the actuator for failures in feedback transducers as well as the currents in each lane.

6.1 Peak lane disparities

In redundant systems, it is inevitable to have inherent parameters variations in repeated hardware and inherent fluctuation in duplicated feedback transducers, which will result in peak disparities over various operating points. Therefore, thresholds have to cater for such inherent disparities.

In the multi-lane electromechanical system, it is natural to observe such disparities over the flight envelope. Therefore, to set the thresholds and to cater for these disparities, peak lanes disparities in discrete flight cases were observed by monitoring over sets of 1500 discrete simulations for a particular flight case. Here, a flight case refers to a set of aircraft speeds ($0.2 \leq \mathrm{m} \leq 1.0$) and aileron reference inputs ($0 \leq \delta_\mathrm{a} \leq$ maximum authority limit) as shown in Table 6.1. The table lists observed peak lane disparities in velocity and torque summed architectures (for the two extreme cases $\delta_\mathrm{a} = 18°$, $\mathrm{m} = 0.2$; and $\delta_\mathrm{a} = 2°$, $\mathrm{m} = 1.0$). The results are based on data supplied by Inland Motors [23], where parameters such as the resistance, inductance, torque constant and voltage constants in the brushless dc motors varied by ±12, ±30, ±10 and ±10 per cent, respectively. Position and velocity feedback transducers were assumed to vary by ±10 per cent.

Table 6.1 Peak lane disparities in velocity and torque summed architectures

δ_a^o	Low aircraft speed						High aircraft speed					
	Potentiometer Reading × 10^{-3} [deg]		**Tachometer Reading [deg/s]**		**Current Reading [A]**		**Potentiometer Reading [deg]**		**Tachometer Reading [deg/s]**		**Current Reading [A]**	
	V-Sum	**T-Sum**	**V-Sum**	**T-Sum**	**V-Sum**	**T-Sum**	**V-Sum**	**T-Sum**	**V-Sum**	**T-Sum**	**V-Sum**	**T-Sum**
0.2	3.54	3.54	1.55	0.0265	0.21	0.298	3.54	3.53	11.88	0.2495	1.97	3.7126
0.5	8.84	8.84	2.11	0.0739	0.34	0.746	8.84	8.84	12.90	0.2132	1.86	3.3986
1.0	17.68	17.68	4.21	0.1685	0.76	1.492	17.68	17.68	12.81	0.1598	1.72	2.8752
1.5	26.52	26.52	6.41	0.2631	1.17	2.238	26.52	26.52	13.24	0.2086	1.77	2.3519
2.0	35.36	35.36	8.86	0.3577	1.58	2.984	35.36	35.36	13.95	0.2574	1.91	2.9842
3.0	53.05	53.10	13.83	0.5469	2.39	4.476						
6.0	106.09	106.13	21.79	0.9364	3.81	6.5591						
9.0	159.14	159.14	23.13	1.2492	3.22	5.786						
12.0	212.19	212.20	26.32	1.4782	2.95	4.974						
15.0	265.23	265.23	26.69	1.7165	2.95	4.974						
18.0	318.28	318.30	25.06	1.7165	2.95	4.974						

6.2 Scheduled threshold setting, STS – failure transients and aircraft response

The above example assumed a 3σ confidence level, which does not meet the full FDI system criteria, however, the designer may consider threshold scheduling for different flight cases to develop an idea about the feasibility of the design. In this particular example, the multi-lane actuator was examined for potentiometer, tachometer and current failures, for both architecture configurations. The results of the simulations are listed in Appendix 1 as Figures 6.1–6.32, where:

- Figures 6.1–6.5 and 6.6–6.11 are velocity summing tests at low and high aircraft speeds, respectively.
- Figures 6.12–6.17 and 6.18–6.23 are torque summing tests at low and high aircraft speeds, respectively.
- Figures 6.24–6.29 are repeated torque summing tests.

In these tests:

- Various step input commands at low and high aircraft speeds were considered.
- Potentiometer and tachometer failures were introduced artificially and were assumed to grow in a *ramp fashion*, however, chip failures were assumed to be sudden failures.
- All failures were introduced at time $t = 2$ s.
- Thresholds on the MVADs were scheduled as calculated in Table 6.1.

Careful examination reveals that:

- Larger failure transients occurred at high aircraft speeds due to the presence of high aerodynamic loads.
- Both architectures were equal in robustness to both motor and potentiometer failures, however, as might be predicted, torque summing showed more robustness than velocity summing to tachometer failures.

Further tests were carried out to examine the effect of repeated failures on the torque summed architecture, at high speed. The system response was examined for two consecutive potentiometer, tachometer and motor drive chip failures, where failures were introduced in sequence at $t = 2.0$ and 3.5 s. The results of these tests are shown in Figures 6.24–6.29, Appendix 1. Although current failures are likely to induce the largest failure transient, the reader should also check and verify the effect of combined failures on the response.

In some applications, dormant failures are also possible; therefore, it is important to test for their possibility of occurrence and their effect. A good example of this is a chip failure to 0.0 or 100 V, Figure 6.30. These failures go unnoticed until there is a change in manoeuvre. For example, a failure at $t = 2$ s remains dormant until the forced change $\delta^{\mathrm{o}}_{18\to 0}|_{2.1,2.11}$ in the input command takes place (where, $\delta^{\mathrm{o}}_{\mathrm{a}\to\mathrm{b}}|_{\mathrm{t}_1,\mathrm{t}_2}$ defines a pulse with a rising edge that changes from $\delta^{\mathrm{o}}_{\mathrm{a}}$ to $\delta^{\mathrm{o}}_{\mathrm{b}}$ at $t = t_1$ s, and a falling edge that changes from $\delta^{\mathrm{o}}_{\mathrm{b}}$ to $\delta^{\mathrm{o}}_{\mathrm{a}}$ at $t = t_2$ s). The lanes respond

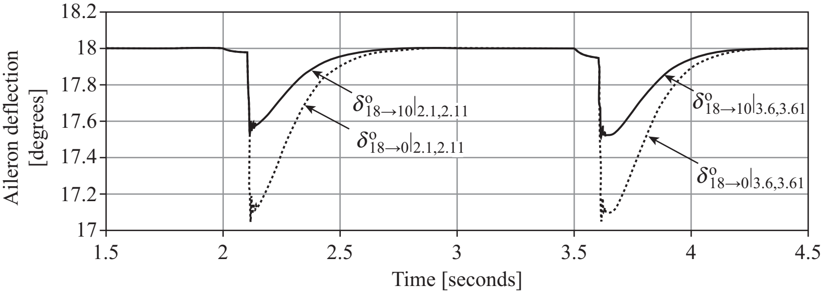

Figure 6.30 Repeated current failures [M = 0.2 in the torque summing architecture]

to this change in manoeuvre and current disparities between the failed lane and the other active lanes keeps on increasing until the threshold is exceeded and the faulty lane is isolated. Similarly, when a second failure is introduced at time $t = 3.5$ s, it remains undetected until a similar manoeuvre ($\delta^{o}_{18\to0}|_{3.6,3.61}$) takes place. Dormant failures can also be eliminated with smaller manoeuvres (e.g. $\delta^{o}_{18\to10}|_{2.1,2.11}$ and $\delta^{o}_{18\to10}|_{3.6,3.61}$), thus the size of the earlier resulting failure transients is fairly pessimistic.

The dormant failure itself does not affect the performance of the actuator, however, its detection and isolation is important to avoid a second repeated failure. To explain this, let I_{12}, I_{13}, I_{14}, I_{23}, I_{24} and I_{34} be the disparities in current measurements between $\text{Lanes}_{1,2}$, $\text{Lanes}_{1,3}$, $\text{Lanes}_{1,4}$, $\text{Lanes}_{2,3}$, $\text{Lanes}_{2,4}$ and $\text{Lanes}_{3,4}$, respectively. If Lane_1 (say) fails and this failure went unnoticed, then current disparities I_{12}, I_{13}, and I_{14} will be less than the set threshold. If another lane (say Lane_2) fails before change in input, then this second failure will also remain unnoticed, since the current disparities I_{23} and I_{24} are also less than the set threshold. If a change in input follows, both failures will not be detected by the FDI system, because immediately after an input is changed I_{13}, I_{14}, I_{23} and I_{24} start to increase and exceed the threshold, however, I_{12} remains below the threshold. Thus, the present FDI law will fail to trigger an alarm and isolation will not be possible. This is, however, only true for the proposed MVAD structure.

The occurrence of an unnoticed dormant failure is a highly unlikely event and it could be overcome by using simple in-time monitoring based upon reasonableness testing. For example, if any of the phase currents is constant for more than 10 micro-processor cycles, then an amber warning is declared.

Failure transients will act as disturbances to the aircraft, and may be approximated by pulses with amplitude that last over a certain period of time. In this application the largest transients were due to repeated current failures at low and high aircraft speeds with 18° and 2° aileron deflections, as shown in Figures 6.30 and 6.31.

The aircraft response in roll due to an aileron pulse disturbance (simulating a failure transient envelope) was tested on a small combat aircraft fighter model [38].

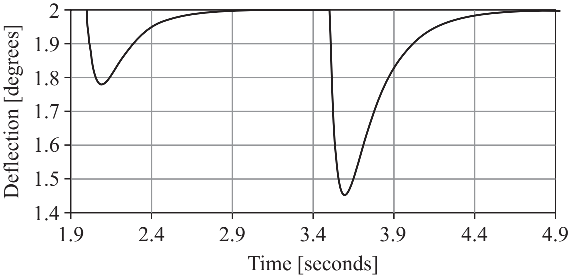

Figure 6.31 Repeated chip failures at high speed utilising torque summing

According to military standards, the allowable roll rate $\rho \leq 5^\circ\ \mathrm{s}^{-e}$ and the maximum bank angle $\emptyset \leq 3^\circ$ [39, 40]. The aircraft model is given by

$$\frac{\rho}{\delta_a}(s) = \frac{(s^2 + 2\xi_\rho\omega_\rho s + \omega_\rho^2)sA_\rho}{(s + T_{sr})(s + T_{rr})(s^2 + 2\xi_D\omega_D s + \omega_D)}$$

$$\frac{\rho}{\delta_a}(s) = \frac{(s^2 + 2\xi_\rho\omega_\rho s + \omega_\rho^2)sA_\rho}{s^4 + \kappa_1 s^3 + \kappa_2 s^2 + \kappa_3 s + \kappa_4}$$

$$\frac{\phi}{\delta_a}(s) = \frac{1}{s}\frac{\rho}{\delta_a}(s)$$

where δ_a, is the aileron deflection,

$$\kappa_1 = 2\xi_D\omega_D + \varrho_1, \qquad \kappa_2 = 2\xi_D\omega_D\varrho_1 + \omega_D^2 + \varrho_2$$

$$\kappa_3 = 2\xi_D\omega_D\varrho_2 + \omega_D^2 + \varrho_1, \quad \kappa_4 = \omega_D^2\varrho_2$$

$$\varrho_1 = T_{rr} - r_{sr},\ \text{and} \qquad \varrho_2 = -T_{rr}T_{sr}$$

At Mach Number 0.9:

$$T_{sr} = -8.7 \times 10^{-3}, \quad T_{rr} = 2.13, \quad \xi_D = 0.184, \quad \omega_D = 3.29,$$

$$\xi_p = 0.0635, \quad A_p = 10.71, \quad \omega_p = 2.87$$

At Mach Number 0.2:

$$T_{sr} = 6.76 \times 10^{-4}, \quad T_{rr} = 1.38, \quad \xi_D = 0.055, \quad \omega_D = 2.13,$$

$$\xi_p = 0.1, \quad A_p = 3.72, \quad \omega_p = 1.674$$

The aircraft was subjected to a disturbance pulse of magnitude 1° and a period of 1 s approximately. This is the largest failure transients ($\delta^o_{18\to 0}|_{2.1,2.11}$ or $\delta^o_{18\to 0}|_{3.6,3.61}$) in Figure 6.30. The aircraft response in roll to this pulse was a peak roll rate of $1.5^\circ\mathrm{s}^{-e}$ and a bank angle of 2° approximately, as shown in Figure 6.32. Then the aircraft was subjected to a pulse of magnitude 0.55° lasting over a period of 1.4 s. This is the second failure transient ($\delta^o_{18\to 0}|_{3.6,3.61}$) in Figure 6.31. This resulted in an aircraft

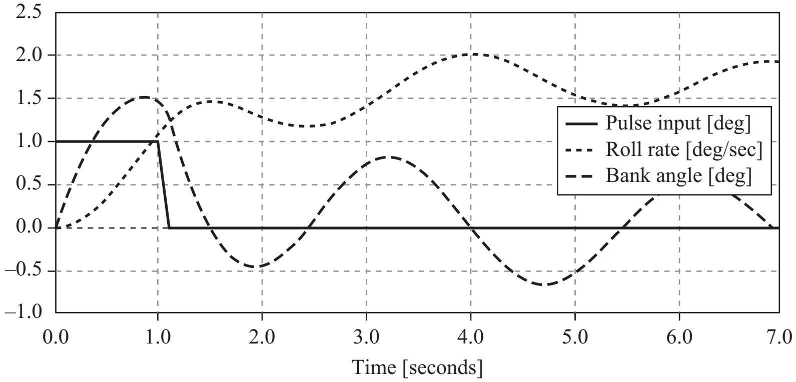

Figure 6.32 Low speed aircraft response in roll

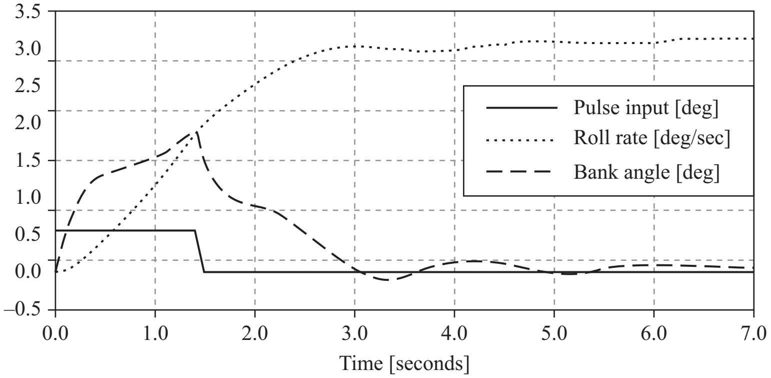

Figure 6.33 High speed aircraft response in roll

peak roll rate of 2°s^{-e} and a bank angle of 3°, as shown Figure 6.33. Therefore, higher disturbances were caused by the second failure transient, thus it is important to check for aircraft disturbances across different flight envelopes. Still, in this particular case, the current design meets the aircraft response in roll specification with two channels isolated.

6.3 Unscheduled threshold setting (UTS) – a simulation graphical Monte Carlo (SGMC) approach

In the previous section, scheduled threshold setting was considered and the largest failure transient was simulated as a pulse input to an aircraft model. It was shown that the current design meets the aircraft response in roll with two channels isolated. By considering a FDI system with this configuration the following should be noted:

- It is difficult to predict the false alarm rate with sufficient confidence, however, for a large sample of normally distributed observations (of peak lane disparities) an approximate estimation of the false alarm rate could be made:
  - The peak lane disparities were obtained with a 3σ confidence levels in parameters variation. Therefore, the probability of producing an observation within this range is ≤ 99.73 per cent.
  - If the thresholds are scheduled to the values of the maximum peak lane disparity, as flight cases change, then the probability of inducing an inherent peak lane disparity which is greater than the maximum peak lane disparity is 0.27 per cent.
  - Since the probability of inducing an inherent peak lane disparity that is greater than the maximum peak lane disparity will trigger a false alarm. Therefore, the probability of a false alarm is 0.27 per cent or 2.7E-4, which does not satisfy the 1.0E-4 false alarm rate.
- With scheduled thresholds setting, the FDI will require information about the aircraft speed and atmospheric pressure to schedule the thresholds. This could raise the question of the reliability of such information and could increase the complexity of the FDI system.

To overcome such problems, unscheduled threshold setting is proposed for the electromechanical actuator in its torque summed architecture. Table 6.1 shows

Table 6.2 Peak failure probability rate

Potentiometer [deg]				**Tachometer [deg/s]**				**Current [A]**			
Int.	**Cnt.**	**C.S.**	**Prob.**	**Int.**	**Cnt.**	**C.S.**	**Prob.**	**Int.**	**Cnt.**	**C.S.**	**Prob.**
0	7	7	0.47	−0.0625	1	1	0.067	0	1	1	0.07
0.025	85	92	6.13	0.0625	43	44	2.93	0.5	88	89	5.93
0.05	186	278	18.53	0.1875	132	176	11.73	1	244	333	22.2
0.075	262	540	36	0.3125	215	391	26.07	1.5	340	673	44.9
0.1	280	820	54.67	0.4375	237	628	41.87	2	275	948	63.2
0.125	248	1068	71.2	0.5625	298	926	61.73	2.5	234	1182	78.8
0.15	175	1243	82.87	0.6875	217	1143	76.2	3	134	1316	87.7
0.175	145	1388	92.53	0.8125	167	1310	87.33	3.5	89	1405	93.7
0.2	54	1442	96.13	0.9375	114	1424	94.93	4	49	1454	96.9
0.225	30	1472	98.13	1.0625	38	1462	97.47	4.5	29	1483	98.9
0.25	18	1490	99.33	1.1875	23	1485	99	5	6	1489	99.3
0.275	8	1498	99.87	1.3125	9	1494	99.6	5.5	5	1494	99.6
0.3	2	1500	100	1.4375	3	1497	99.8	6	4	1498	99.87
0.325	0	1500	100	1.5625	1	1498	99.87	6.5	1	1499	99.93
				1.6875	1	1500	100				

Int is Interval, Cnt is counts per interval, CS is Cumulative Sum and Prob is percentage probability.

that the maximum peak lane disparities in potentiometer, tachometer and current readings occurred in $\delta_{\mathrm{a}}|_{18^{\circ},0.2}$, $\delta_{\mathrm{a}}|_{18^{\circ},0.2}$ and $\delta_{\mathrm{a}}|_{6^{\circ},0.2}$ flight cases, respectively. Therefore, if unscheduled thresholds are to be considered only data-banks from the above flight cases should be considered.

To implement the SGMC approach:

- First the data-bank has to be divided into intervals.
- The number of counts per each interval is observed.
- A cumulative sum of the counts is then obtained.
- Finally the percentage probability of occurrence is calculated, as listed in Table 6.2.

The percentage probabilities in each interval are then plotted on the probability graphs as shown in Figures 6.34–6.36, where the x-axis represents the percentage

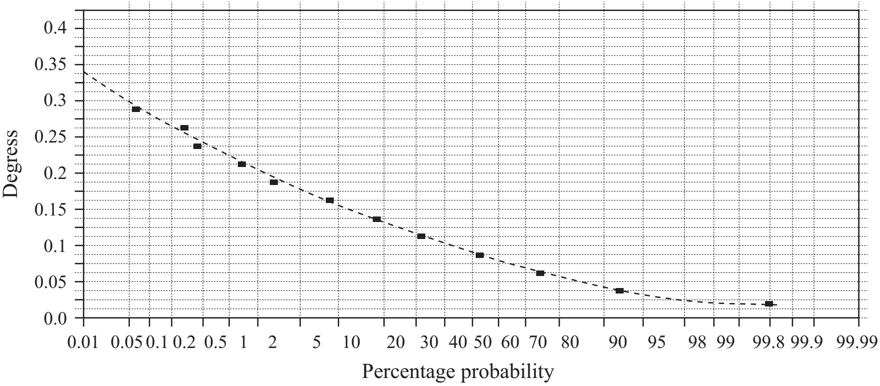

Figure 6.34 Peak disparity percentage probability rate in potentiometer readings

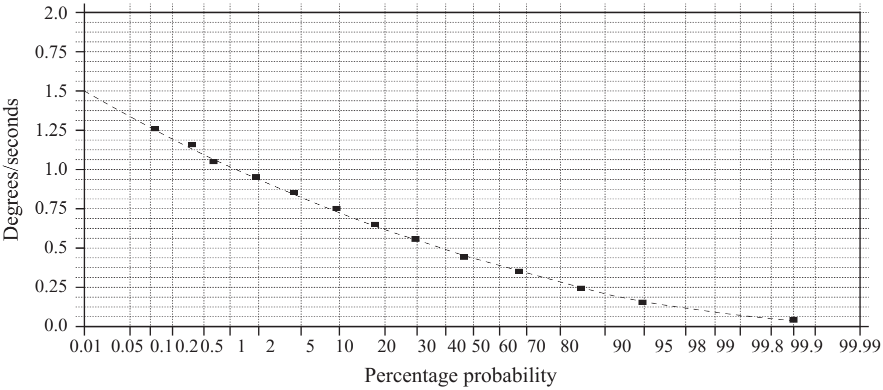

Figure 6.35 Peak disparity percentage probability rate in tachometer readings

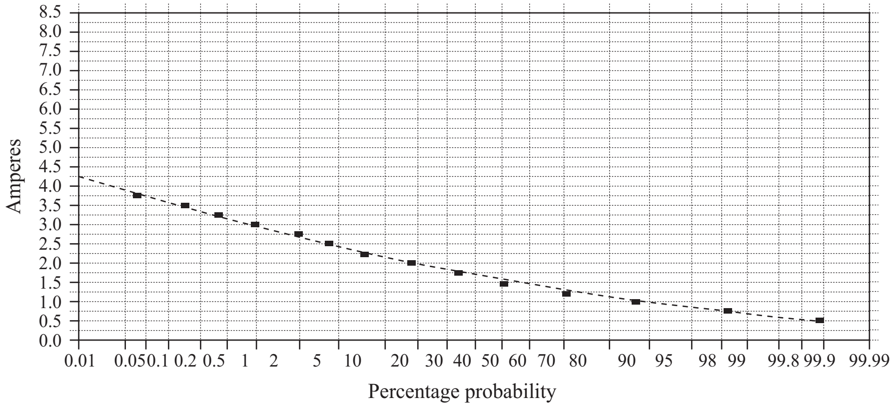

Figure 6.36 Peak disparity percentage probability rate in current reading

probability rate and the y-axis represents the cumulative sum in peak lane disparities. The plotted graph is then extrapolated to intersect the y-axis at a value that represents a threshold value with a 1.0E-4 likelihood of occurrence. In this particular example, the potentiometer, tachometer and current thresholds were found to be 0.375°, $1.5°s^{-1}$ and 4.25 A.

When the thresholds values on the MVADs were set, and failure transients due to potentiometer, tachometer and current failures were observed, it was found that:

- Failure transients due to potentiometer and tachometer failures are larger than those produced earlier (in scheduled threshold setting), due to the fact that: larger threshold values are implemented; and failures were allowed to progress in a ramp fashion.
- Failure transients due to chip failures remain to be the largest.
- There was no change in the size of the failure transients due to chip failures, thus in this particular application a similar aircraft response will be achieved, however, with the current threshold setting, the false alarm rate is reduced to a maximum of 1.0E-4.

Chapter 7

Digital cross monitoring

The previous chapter presented hardware cross monitoring in both architectures, and showed that the largest failure transients were motor failures related. Although the design met the aircraft response in roll, repeated hardware components in hardware cross monitoring necessitates for larger installation compartments. Therefore, this chapter proposes and compares digital cross monitoring (with a minimum of two lanes of repeated hardware) to hardware cross monitoring. Here, the hardware will be represented by three-phase equivalents and the digital mathematical model will be represented by the lumped model equivalent. The three-phase hardware representation allows for detailed response examination in the presence of torque ripples contributed by the individual lanes. The Simulation Graphical Monte Carlo (SGMC) method will be implemented in this chapter too as a threshold setting technique.

7.1 Hardware cross monitoring

This approach has already been presented in the previous chapter, with lumped motors representation. Here, three-phase model equivalents will be used. The MVADs will perform the same operations described in the previous chapter, with the MVAD input signals modified to cater for motor and switching drive failures. To achieve this, the signals are represented by the sum of the absolute values of the filtered measurements of the individual phase currents, as shown in equation 7.1. This modification eliminates the need for motor alignment, which is practically undesirable. The time constant (T) should be chosen so that an acceptable smooth response is obtained (Figure 7.1).

$$\mathrm{I_{Fp}} = \sum_{q=1}^{3} |\mathrm{I_{Fpq}}| \tag{7.1}$$

where

$$\frac{\mathrm{I_{Fpq}}}{\mathrm{I_{pq}}}(\mathrm{s}) = \frac{1}{1 + \mathrm{Ts}} \tag{7.2}$$

$\mathrm{I_{pq}}$ is the computed phase currents and $\mathrm{I_{Fpq}}$ is the filtered lane current, with p and q refer to channel and phase numbers.

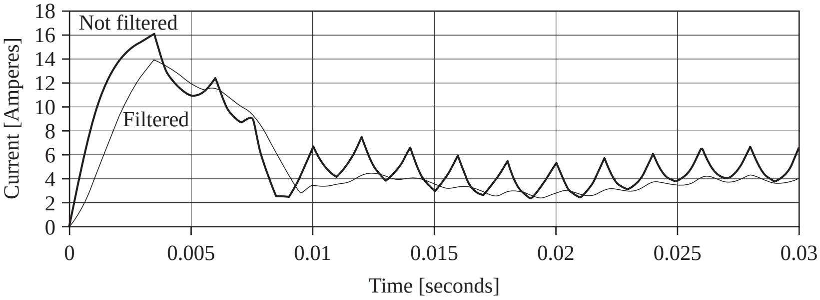

Figure 7.1 Phase current measurement smoothing

In this chapter too, transducer failures were introduced in a ramp fashion and motor failures were introduced as sudden failures. In some cases, current failures were not detected and isolated immediately and remained dormant until there was a change in manoeuvre. To illustrate this, assume that the system is stable with all lanes driven at the Commutation-State$_1$, i.e. $V_{A_{1\sim4}} = V_{SP}$, $V_{B_{1\sim4}} = 0$ and $V_{C_{1\sim4}} = V_{SP}$, where, V_{SP} is the Supply Voltage.

Assuming that a failure will develop in Lane$_1$, it follows that a short circuit between V_{A_1} and V_{C_1} (i.e. both nodes are sitting at the V_{SP} level) will not be detected as a failure, unless a change in input command takes place. Dormant failures are highly unlikely events and (as was mentioned earlier on) could be eliminated by simple in-time monitoring based upon reasonableness testing.

7.1.1 Unscheduled threshold settings (UTS)

UTS was proposed in the earlier chapter to overcome problems associated with STS that required the FDI system to continuously update information about the aircraft speed and atmospheric pressure. To achieve UTS, the SGMC approach utilises data of flight cases that gave maximum peak lane disparities in potentiometer, tachometer and current readings.

In this chapter, three-phase models were considered to calculate inherent peak lane disparities (due to random variation in parameters and random fluctuation in feedback transducers) in 1500 tests for different flight cases. Just as in the previous chapter, the results are categorised in data-banks and maximum peak lane disparities were observed over a range of flight cases. Table 7.1 lists the two extreme flight cases only, which have similar characteristics to those of the lumped model with the exception that the currents are represented by the sum of the absolute values of the filtered phase currents.

If the FDI system is to have MVADs with unscheduled thresholds, then only flight cases yielding maximum peak lane disparities should be considered. Table 7.1 shows that the maximum peak lane disparities in potentiometer, tachometer and current readings occur at the $\delta_a = 18°$-low aircraft speed flight case. Therefore, data-banks from this particular flight case were considered, and peak disparities obtained from the 1500 simulations were interpreted in terms of percentage probability of occurrence within certain intervals. Table 7.2 lists the

Table 7.1 The three phase peak hardware disparities

Low aircraft speed				High aircraft speed			
Aileron deflection [deg]	**Peak lane disparities in**			**Aileron deflection [deg]**	**Peak lane disparities in**		
	Pot reading [deg]	**Tacho reading [deg/s]**	**Current reading [A]**		**Pot reading [deg]**	**Tacho reading [deg/s]**	**Current reading [A]**
0.2	0.003	0.027	0.257	0.2	0.003	0.183	1.871
2	0.033	0.289	1.385	1	0.016	0.161	2.111
9	0.149	1.189	3.862	2	0.032	0.271	2.373
14	0.223	1.258	3.862				
18	0.296	1.258	3.862				

Table 7.2 Peak failure rate probability in hardware cross monitoring

Potentiometer [deg]				Tachometer [deg/s^{-1}]				Current [A]			
Int	**Cnt**	**CS**	**Prob**	**Int**	**Cnt**	**CS**	**Prob**	**Int**	**Cnt**	**CS**	**Prob**
−0.0125	3	3	0.2	−0.05	2	2	0.13	0.25	3	3	0.2
0.0125	114	117	7.8	0.05	72	74	4.93	0.5	30	33	2.2
0.0375	259	376	25.07	0.15	155	229	15.27	0.75	134	167	11.13
0.0625	346	722	48.13	0.25	259	488	32.53	1	236	403	26.87
0.0875	293	1015	67.67	0.35	299	787	52.47	1.25	306	709	47.27
0.1125	218	1233	82.2	0.45	256	1043	69.53	1.5	237	946	63.07
0.1375	130	1363	90.87	0.55	194	1237	82.47	1.75	211	1157	77.13
0.1625	92	1455	97	0.65	114	1351	90.07	2	159	1316	87.73
0.1875	25	1480	98.67	0.75	83	1434	95.6	2.25	76	1392	92.8
0.2125	13	1493	99.53	0.85	38	1472	98.13	2.5	47	1439	95.93
0.2375	2	1495	99.67	0.95	17	1489	99.27	2.75	35	1474	98.27
0.2625	4	1499	99.93	1.05	5	1494	99.6	3	15	1489	99.27
0.2875	1	1500	100	1.15	4	1498	99.87	3.25	6	1495	99.67
				1.25	2	1500	100	3.5	4	1499	99.93
								3.75	1	1500	100

Note: Cnt is counts per interval; CS is cumulative sum; and Prob is percentage probability.

inherent percentage probability in peak lane disparities, with the 1st, 5th and 9th columns being the intervals at which the probabilities of these rates were calculated. The 2nd, 6th and 10th columns list the counts per interval. The 3rd, 7th and 11th columns list the cumulative sums of counts, while the 4th, 8th and 12th columns show the percentage probabilities of the cumulative sums.

The percentage probabilities of the cumulative sums were plotted on probability graph paper (Figures 7.2–7.4) and were then extrapolated to cross the y-axis at points that represent maximum peak lane disparities with 1.0E-4 probabilities of occurrence. Therefore, the thresholds on the MVADs in the FDI system are 0.4°, 1.875°s^{-1} and 8.0 A. The figures show and compare the threshold values due to the lumped and three-phase models. Clearly there is a close correlation between potentiometer and

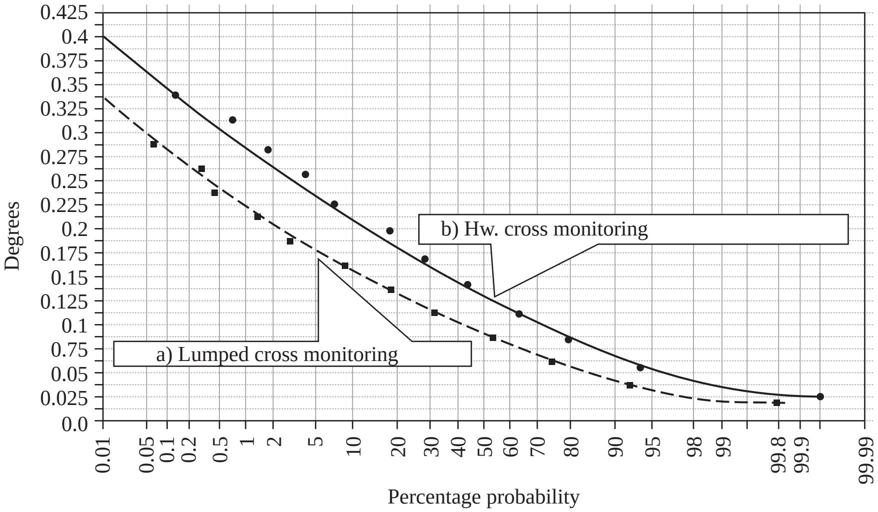

Figure 7.2 Peak disparity percentage probability rate in potentiometer reading

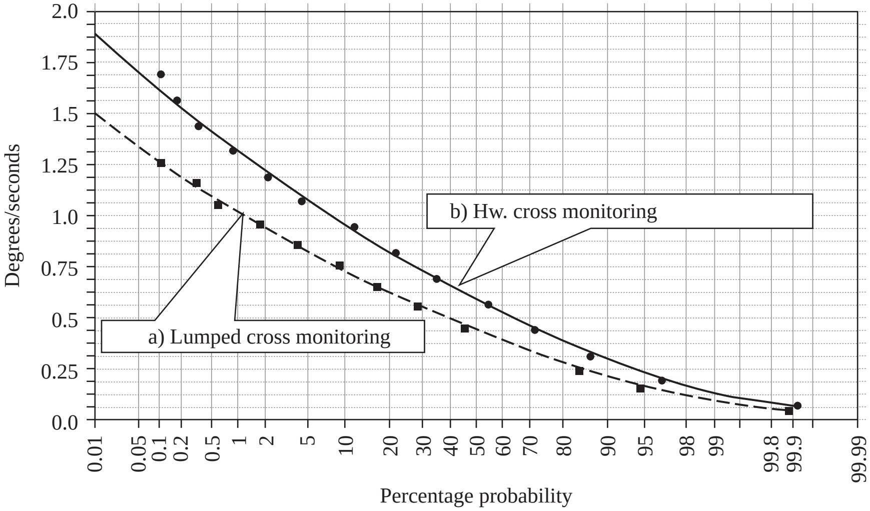

Figure 7.3 Peak disparity percentage probability rate in tachometer reading

tachometer threshold values. However, the current threshold is considerably different (nearly doubled), which is due to the peak lane disparities in current representation.

7.1.2 Failure transients and aircraft response

Unscheduled threshold monitoring was implemented with the above calculated thresholds. In the event of a feedback transducer failure, the failed transducer will be isolated, however, if a lane is failed, then the entire lane will be energised and isolated.

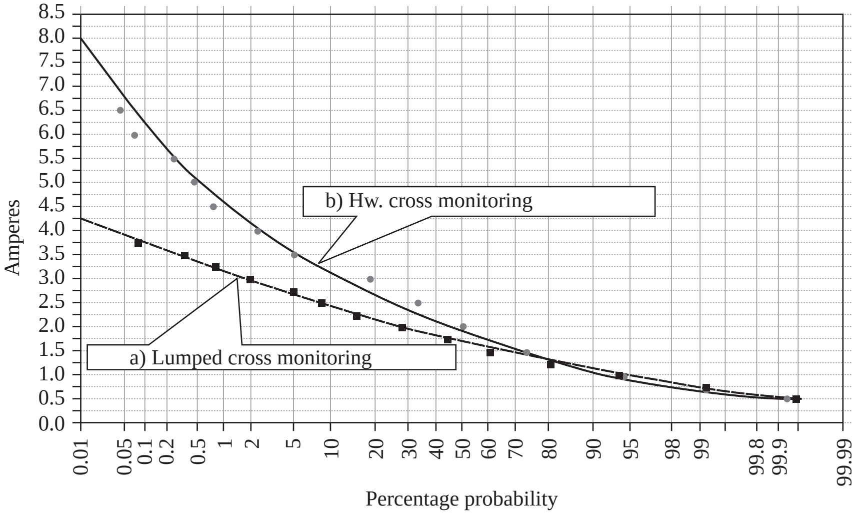

Figure 7.4 Peak disparity percentage probability rate in current reading

Failures were introduced at a sequence of 1.0 and 2.0 s and the resulting failure transients were examined for various flight cases, as shown in Appendix 2 (Figures 7.5–7.13). It was found that the maximum failure transients were due to motor failures, with the largest failure transient envelope (occur at $\delta_a = 18^\circ|_{\text{low aircraft speed case}}$) has an amplitude of 1° and lasts over a period of 0.8 s. In the $\delta_a = 2^\circ|_{\text{high aircraft speed case}}$, the largest failure transient has an amplitude of 0.3° decaying over a period of 0.7 s. When simulated as aileron pulse disturbances to the aircraft model, the aircraft response revealed that the current design meets the aircraft response in roll with two channels isolated, as shown in Figures 7.14 and 7.15.

7.2 Digital cross monitoring (DCM)

An alternative strategy for monitoring is to cross monitor a reduced number of repeated hardware components against an incorporated lumped digital math model. Figure 7.16 shows a possible architecture that implements such DCM scheme. Here, a four-lane assembly was assumed with each lane having its own embedded digital model. The individual and overall responses of the actuator were evaluated in each processor. The generated outputs of the microcomputers are then voted to calculate the currents in each lane and to provide a unified speed and position feedback. These calculated values are then compared with those obtained from the sensor readings, the microcomputers will then return the averaged sensor readings as feedback signals. In the event of a failure, the faulty sensor or channel will be isolated and the feedback signals will be the average value of the active signals only.

To implement this technique, four additional comparators must be introduced to the MVADs to compute the difference between the math model parameters and

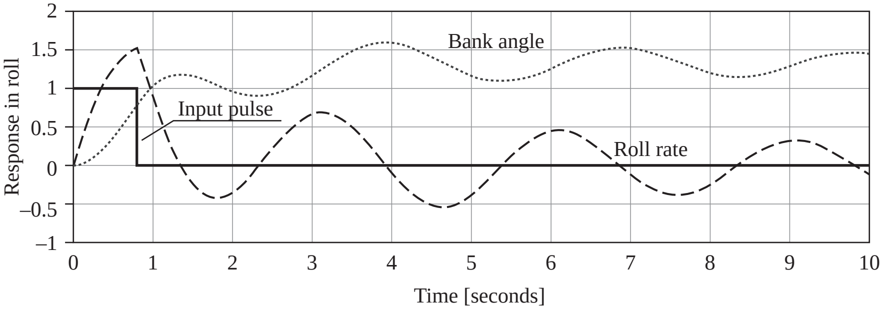

Figure 7.14 Low aircraft speed response in roll

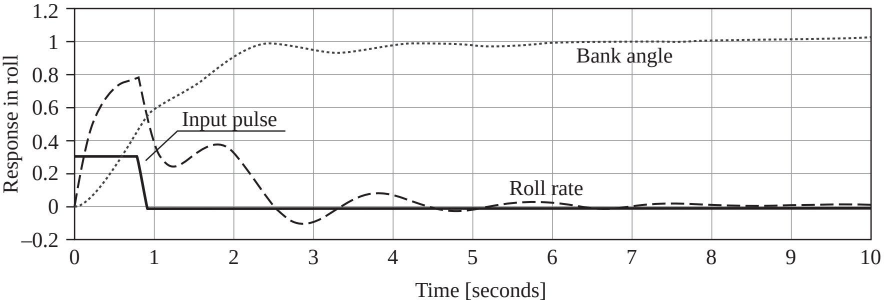

Figure 7.15 High aircraft speed response in roll

the hardware measured readings. If the calculated parameters from the math model are denoted by S_m, then the difference signals between a lane (from $\text{Lanes}_{1\sim4}$) and the math model are denoted by $\Delta_{s_{mp}}$, where p being the lane number (p = 1, 2, 3 or 4). Also, denoting $\Delta_{s_{pq}}$ as the disparity signal between lanes p and q. Thus, $\Delta_{s_{m1}}$ describes the difference between the math model and lane_1; and $\Delta_{s_{13}}$ is the signal that describes the disparity between lanes 1 and 3. In this architecture, to check for failures, both $\Delta_{s_{mp}}$ and $\Delta_{s_{pq}}$ must simultaneously be used to calculate the thresholds, where: the thresholds due to lane disparities (i.e. $\Delta_{s_{pq}}$) are the same as those calculated earlier on; and thresholds due to disparities between the math model and the lanes (i.e. $\Delta_{s_{mp}}$) are to be calculated next.

7.2.1 Unscheduled threshold setting

Table 7.3 lists the maximum peak hardware-digital model disparities in position, speed and current readings. These values are higher than those of $\Delta_{s_{pq}}$, which could be explained by examining the nominal responses of the hardware and the digital model, Figures 7.17–7.19. The figures show that the nominal peak differences in position and speed measurements were 0.9° and $38.7°\text{s}^{-e}$, for the $\delta_a = 18°$ at low aircraft speed, and the nominal peak difference in current measurement was 6.3 A, for the $\delta_a = 9°$ at low aircraft speed. The parameters in the controllers of the lumped

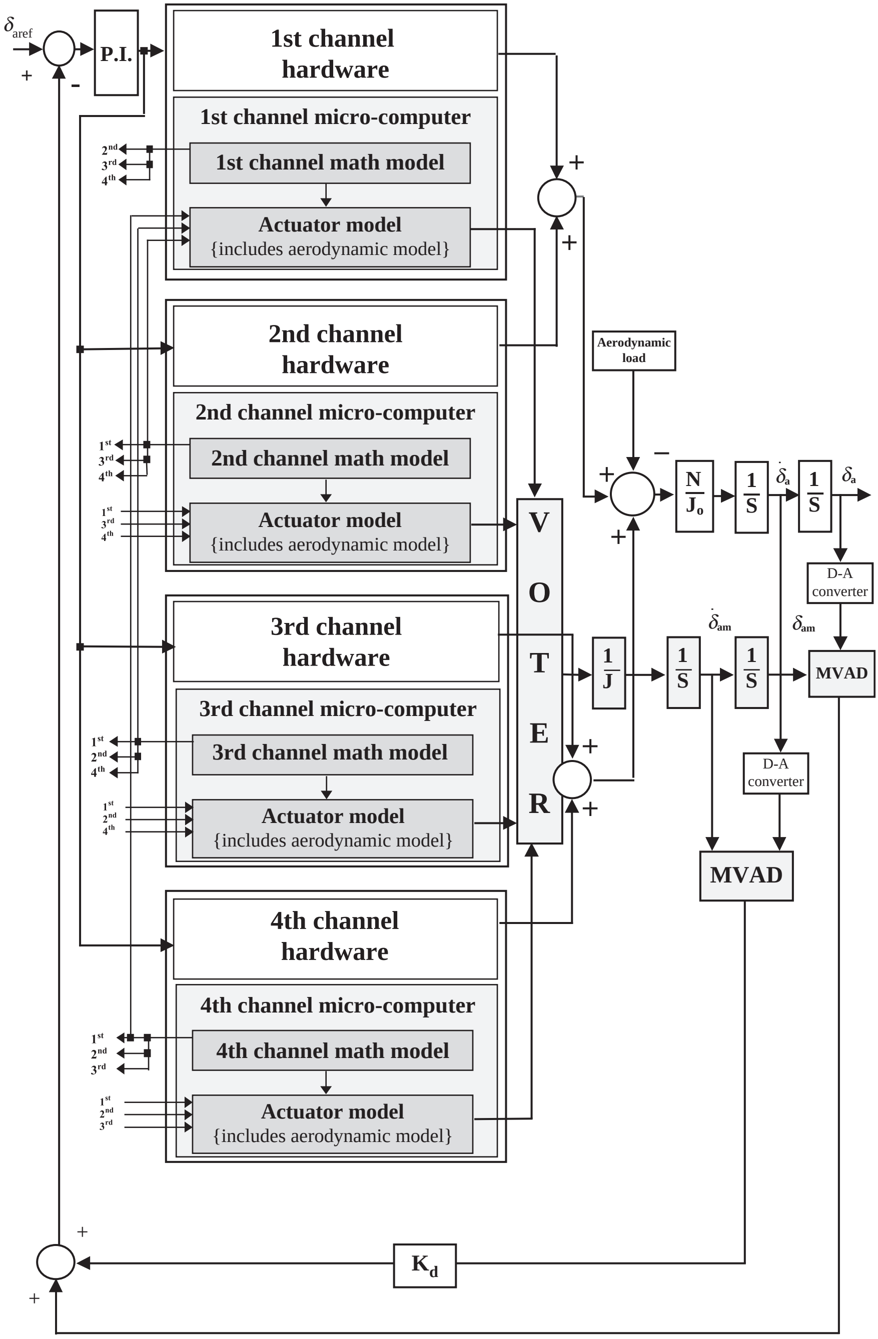

Figure 7.16 Hardware-digital math model FDI system configuration

Table 7.3 The three-phase peak lane disparities, utilising a math model

Low aircraft speed				High aircraft speed			
Aileron deflection [deg]	**Peak lane disparities in**			**Aileron deflection [deg]**	**Peak lane disparities in**		
	Potentiometer reading [deg]	**Tachometer reading [deg/s]**	**Current reading [A]**		**Potentiometer reading [deg]**	**Tachometer reading [deg/s]**	**Current reading [A]**
2	0.02	4.71	3.67	1	0.015	3.46	3.26
9	0.10	33.63	10.35	2	0.03	5.37	4.38
14	0.65	34.55	9.00				
18	2.0	46.76	9.44				

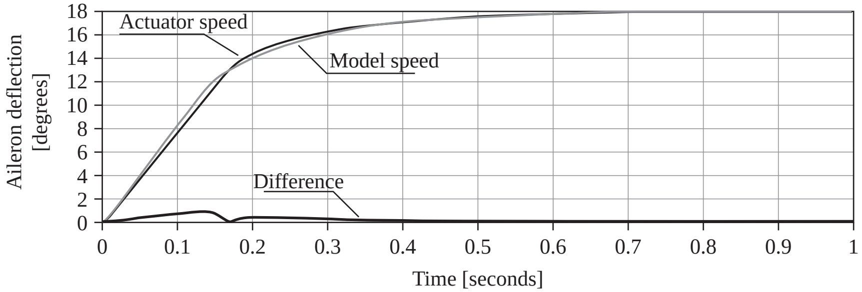

Figure 7.17 Actuator and math model position response

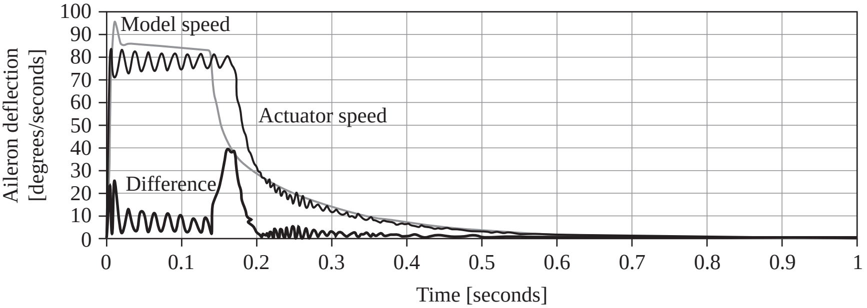

Figure 7.18 Actuator and math model speed response

and three-phase models were adjusted to minimise the differences between the two responses, however, the wide range of flight cases (in this particular application) and load nonlinearity distribution limited these efforts.

Table 7.4 lists the intervals, the counts per interval, the cumulative sums and the percentage probabilities of the cumulative sums. The cumulative sums were plotted and the graphs were extrapolated to calculate the maximum peak lane disparities, with 1.0E-4 probability rate of occurrence, as shown in Figures 7.20–7.22. Therefore, the MVAD threshold values are 2.0°, $47^{\circ}\mathrm{s}^{-e}$ and 10.75 A.

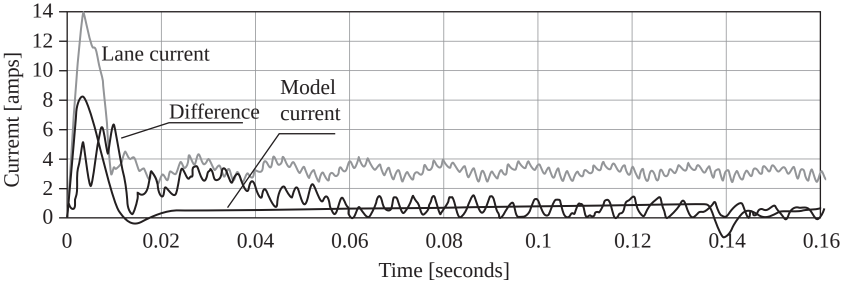

Figure 7.19 Actuator and math model currents

Table 7.4 Peak failure rate probability in cross monitoring against a math model

Potentiometer [deg]				Tachometer [deg/s^{-1}]				Current [A]			
Int	**Cnt**	**CS**	**Prob**	**Int**	**Cnt**	**CS**	**Prob**	**Int**	**Cnt**	**CS**	**Prob**
0.7	1	1	0.067	33.5	3	3	0.2	6.0	2	2	0.133
0.8	627	628	41.87	34.5	12	15	1	6.25	2	4	0.27
0.9	527	1155	77	35.5	18	33	2.2	6.5	7	11	0.73
1	12	1167	77.8	36.5	6	39	2.6	6.75	48	59	3.93
1.1	13	1180	78.67	37.5	18	57	3.8	7.0	132	191	12.73
1.2	21	1201	80.07	38.5	147	204	13.6	7.25	178	369	24.6
1.3	18	1219	81.27	39.5	811	1015	67.67	7.5	256	625	41.67
1.4	30	1249	83.27	40.5	182	1197	79.8	7.75	232	857	57.13
1.5	100	1349	89.93	41.5	59	1256	83.73	8.0	197	1054	70.27
1.6	79	1428	95.2	42.5	44	1300	86.67	8.25	164	1218	81.2
1.7	67	1495	99.67	43.5	53	1353	90.2	8.5	137	1355	90.33
1.8	4	1499	99.93	44.5	50	1403	93.53	8.75	76	1431	95.4
1.9	1	1500	100	45.5	87	1490	99.33	9.0	35	1466	97.73
2	0	1500	100	46.5	10	1500	100	9.25	18	1484	98.93
								9.5	9	1493	99.53
								9.75	4	1497	99.8
								10.0	2	1499	99.93
								10.25	1	1500	100

Note: Int is Interval, Cnt is counts per interval, CS is cumulative sum and Prob is percentage probability.

7.2.2 Failure transients

The thresholds on the MVADs were set to the above calculated values, and simulations were carried out to examine the actuator response to a sequence of failures at $t = 1$ and 2 s.

Repeated potentiometer failures

The failed potentiometer measurements were assumed to increment in a ramp fashion at a similar rate of 20 deg/s slope. Figures 7.23 and 7.24 show the low and high aircraft speeds failure transients. The transients had magnitudes of 0.15° and 0.23°, decaying over a period of 0.8 s. These are much higher than those induced by hardware cross monitoring, indicating the effect of the higher threshold.

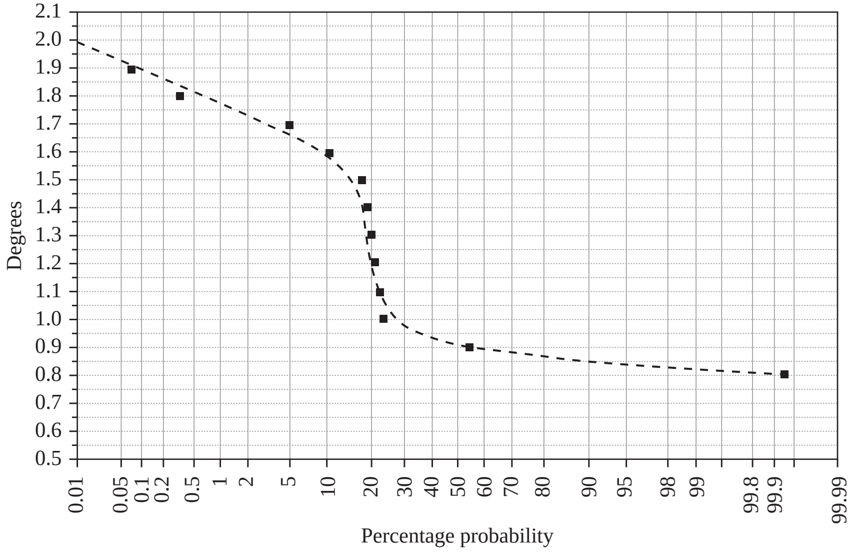

Figure 7.20 Peak disparity percentage probability rate in potentiometer readings

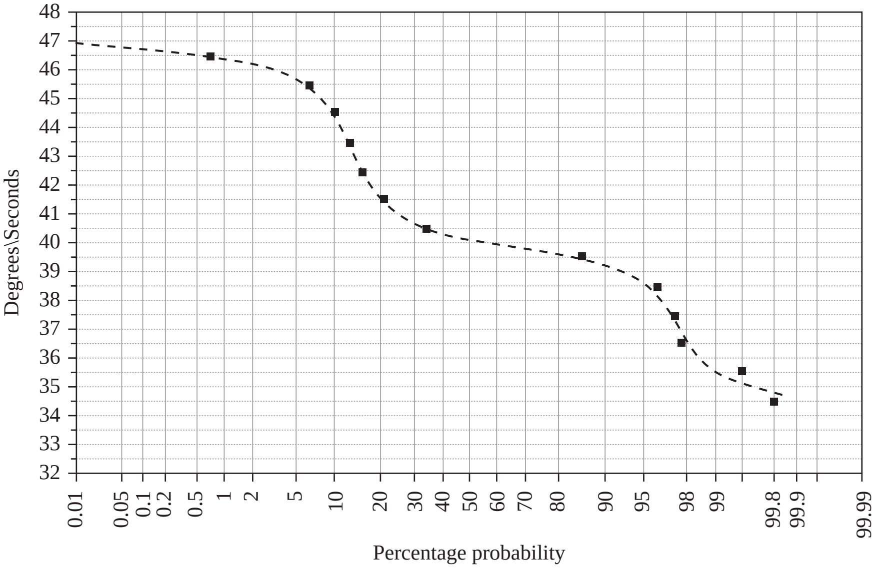

Figure 7.21 Peak disparity percentage probability rate in tachometer readings

Repeated tachometer failures

The failed tachometer measurements were also assumed to increment in a ramp fashion of 100 deg/s^2 slope. The maximum failure transient was due to the second failures in Figures 7.25 and 7.26, and had amplitude of 1.6° decaying over a period

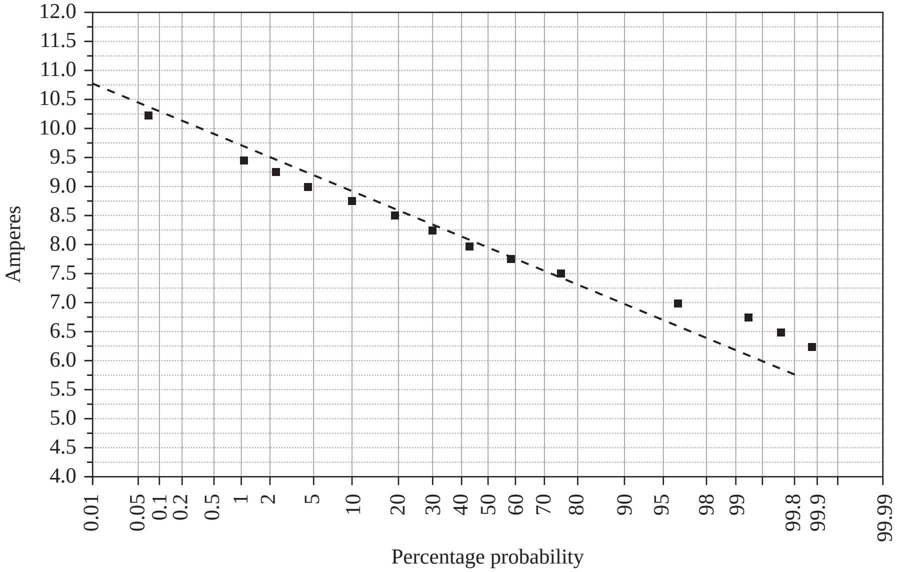

Figure 7.22 Peak disparity percentage probability rate in current readings

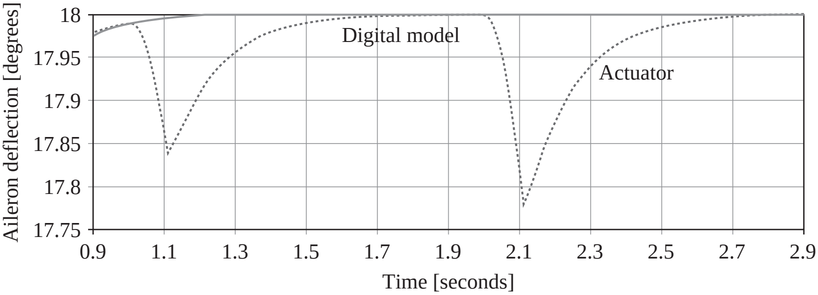

Figure 7.23 Repeated potentiometer failures in digital cross monitoring [torque summing architecture at low aircraft speed]

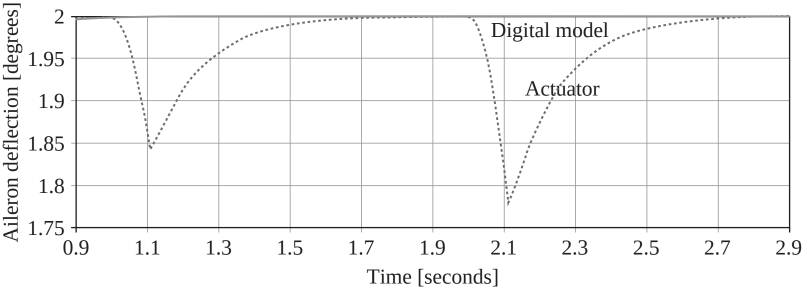

Figure 7.24 Repeated potentiometer failures in digital cross monitoring [torque summing architecture at high aircraft speed]

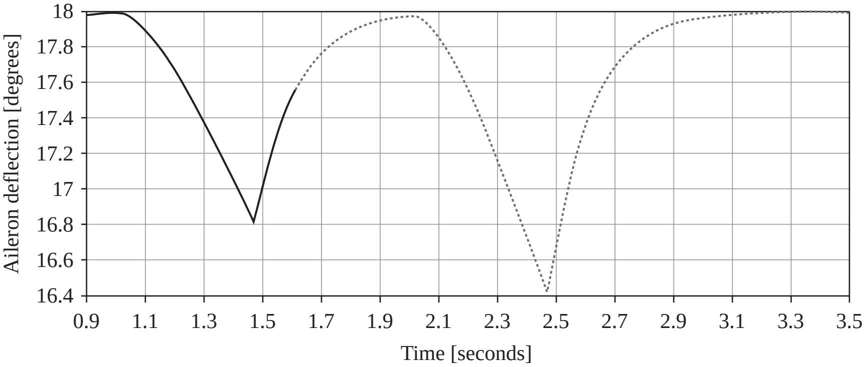

Figure 7.25 Repeated tachometer failures in digital cross monitoring [torque summing architecture at low aircraft speed]

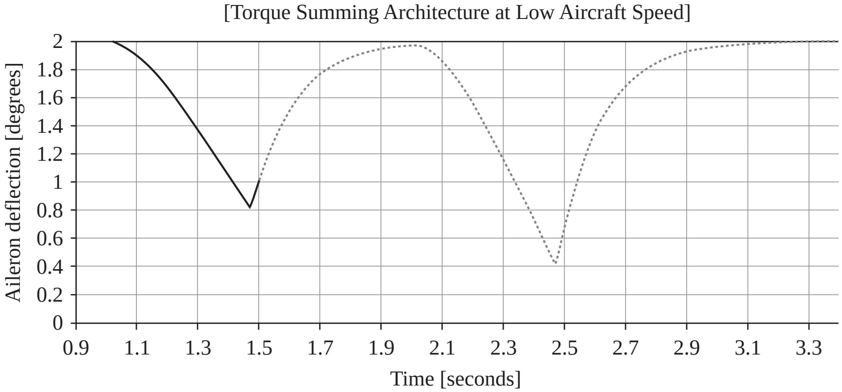

Figure 7.26 Repeated tachometer failures in digital cross monitoring [torque summing architecture at high aircraft speed]

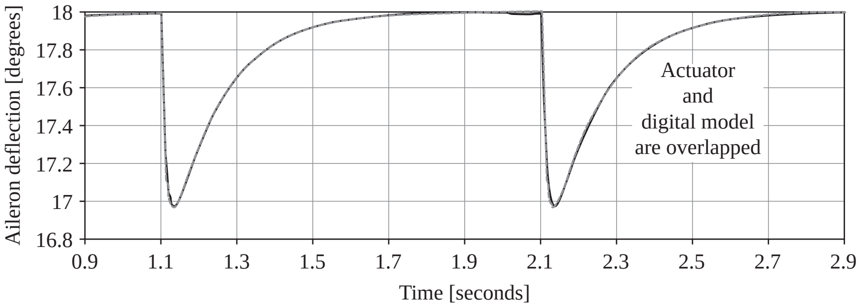

Figure 7.27 Repeated motor failures in digital cross monitoring [torque summing architecture at low aircraft speed]

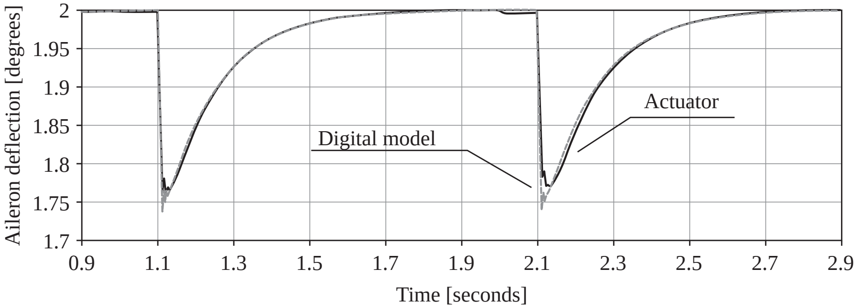

Figure 7.28 Repeated motor failures in digital cross monitoring [torque summing architecture at high aircraft speed]

of 1.2 s. The first failure transient had amplitude of 1.2° decaying over a period of 1.0 s.

Repeated current failures

Just as in hardware cross monitoring dormant failures might be possible, Figure 7.27 and 7.28. The size of the maximum failure transients were found to be 1.0° lasting over a period of 0.8 s at low aircraft speed, and 0.25° lasting over periods of 0.8 s at high aircraft speed transients.

7.2.3 Hardware versus digital cross monitoring

Clearly that when compared, digital cross monitoring has no special advantages over hardware cross monitoring apart from reducing the number of lanes of hardware. Some of the limitations include accurate modeling of the hardware, which might increase the disparities, thus increasing the thresholds.

Appendix 1

Hardware cross monitoring

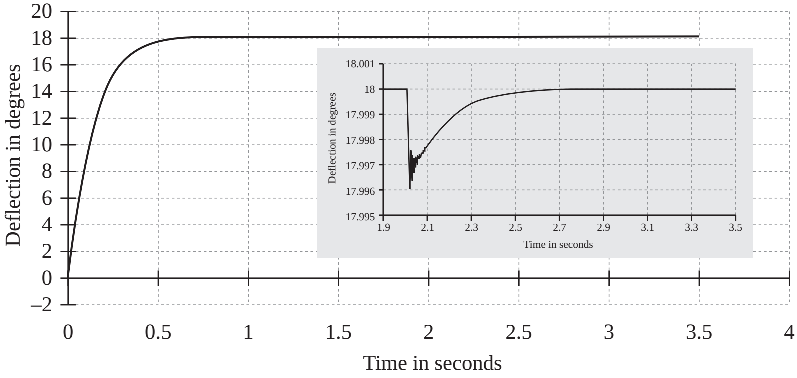

Figure 6.1 Potentiometer failure at low speed [velocity summing]

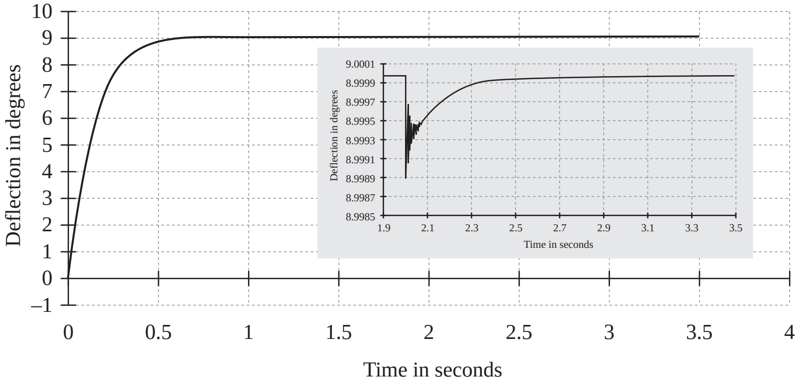

Figure 6.2 Potentiometer failure at low speed [velocity summing]

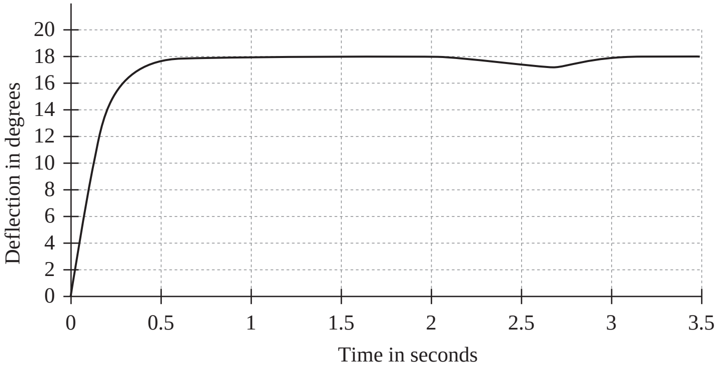

Figure 6.3 Tachometer failure at low speed [velocity summing]

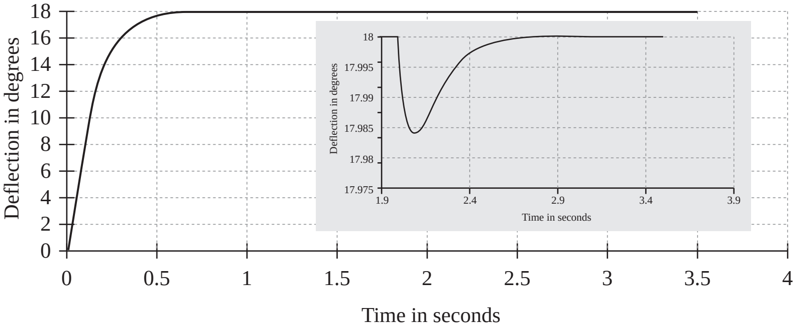

Figure 6.4 Motor failure at low speed [velocity summing]

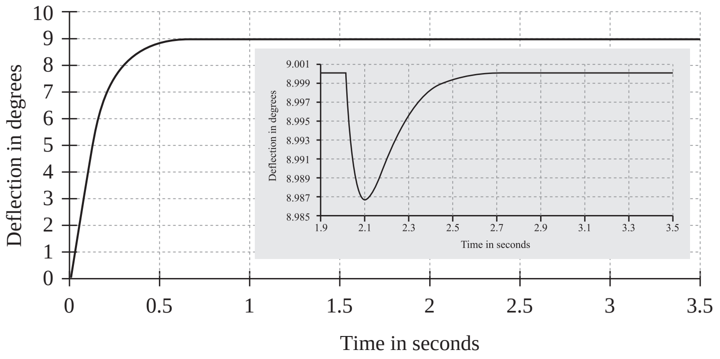

Figure 6.5 Motor failure at low speed [velocity summing]

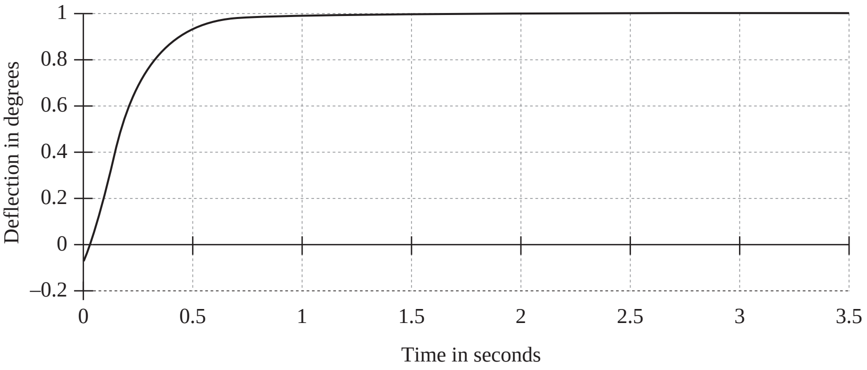

Figure 6.6   Potentiometer failure at high speed [velocity summing]

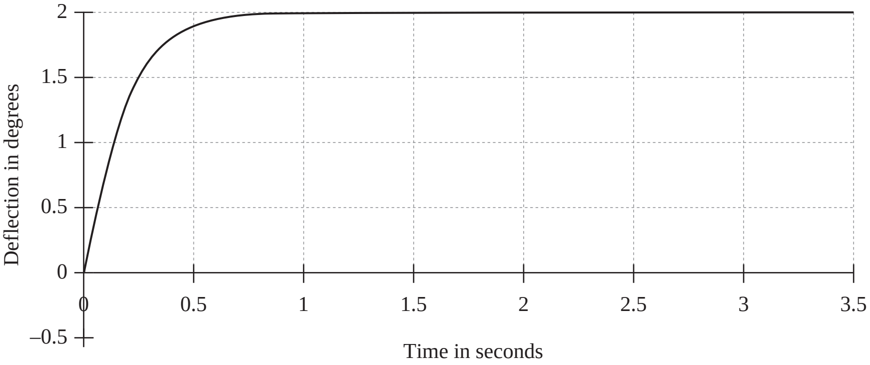

Figure 6.7   Potentiometer failure at high speed [velocity summing]

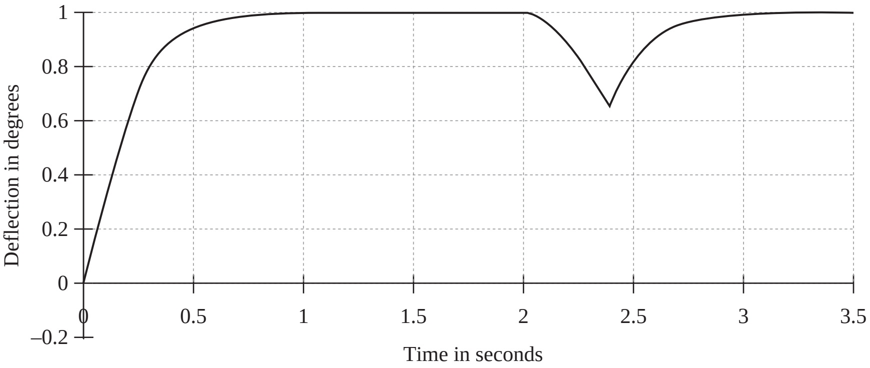

Figure 6.8   Tachometer failure at high speed [velocity summing]

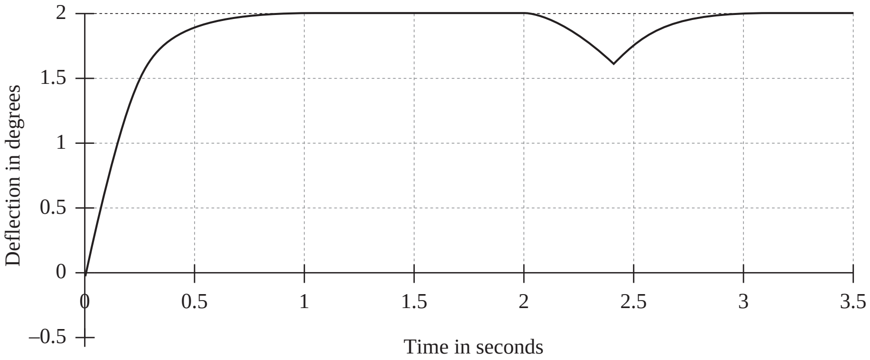

Figure 6.9 Tachometer failure at high speed [velocity summing]

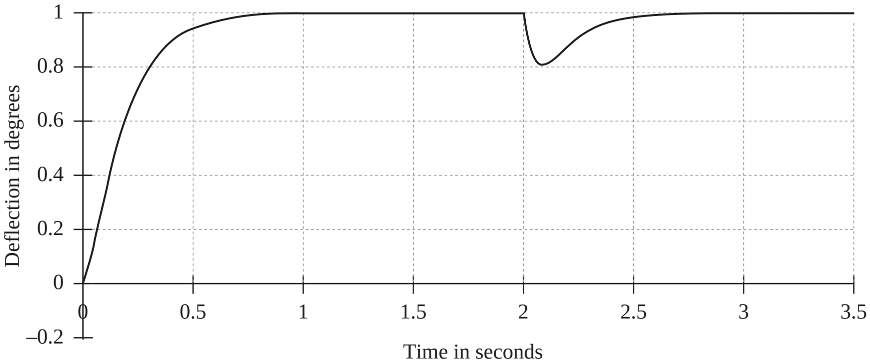

Figure 6.10 Motor failure at high speed [velocity summing]

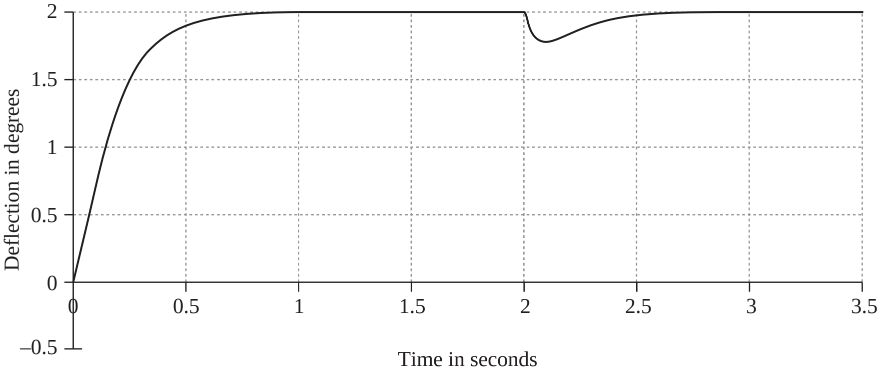

Figure 6.11 Motor failure at high speed [velocity summing]

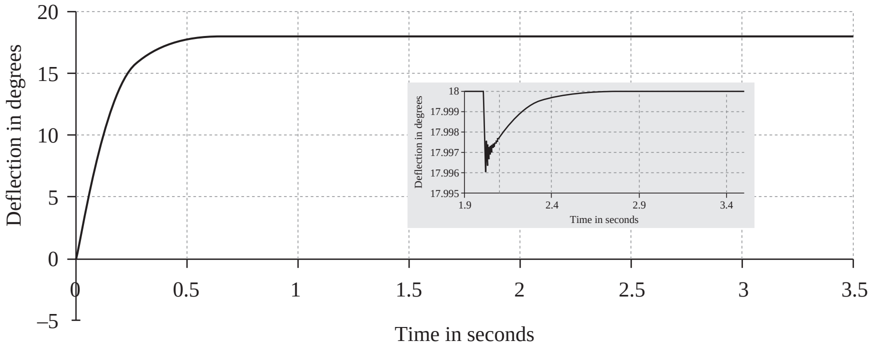

Figure 6.12 Potentiometer failure at low speed [torque summing]

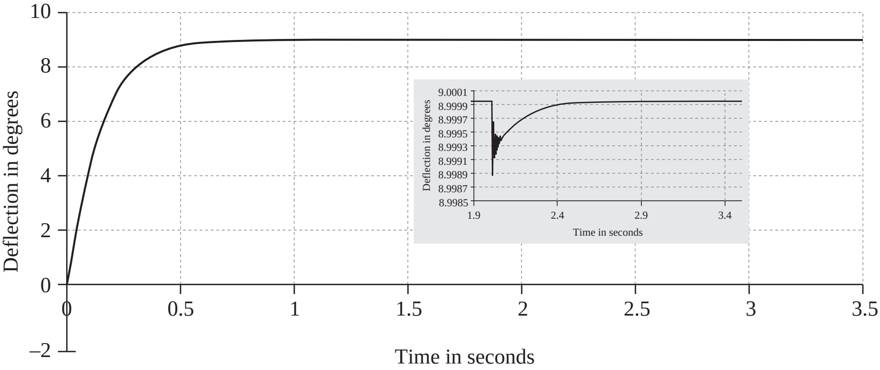

Figure 6.13 Potentiometer failure at low speed [torque summing]

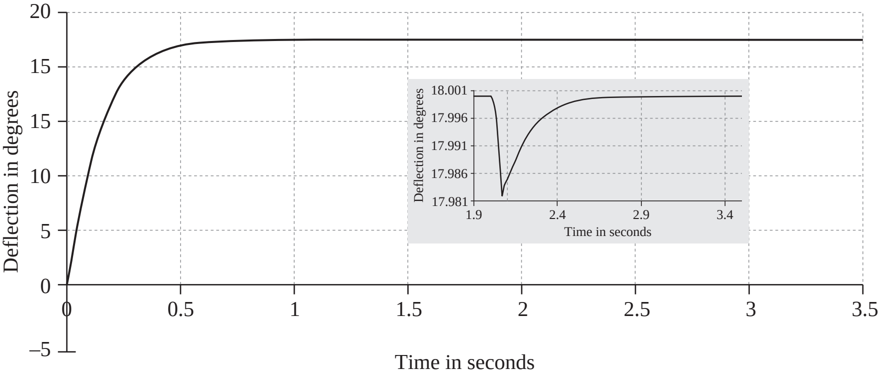

Figure 6.14 Tachometer failure at low speed [torque summing]

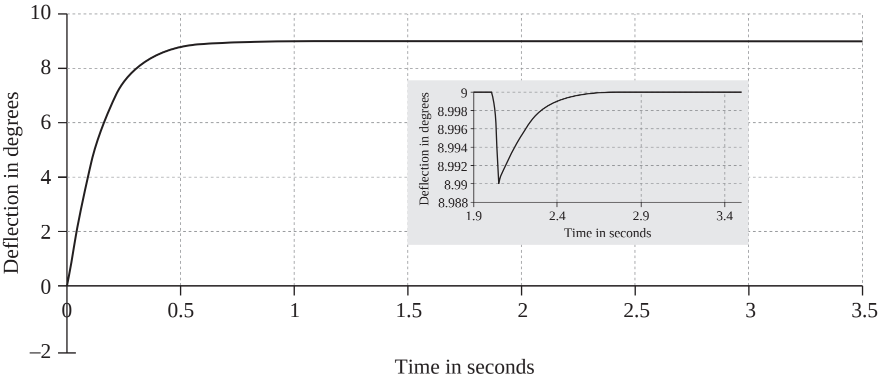

Figure 6.15 Tachometer failure at low speed [torque summing]

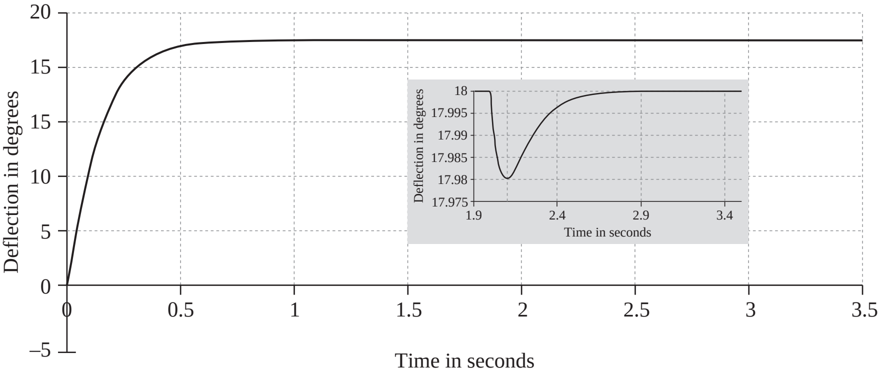

Figure 6.16 Motor failure at low speed [torque summing]

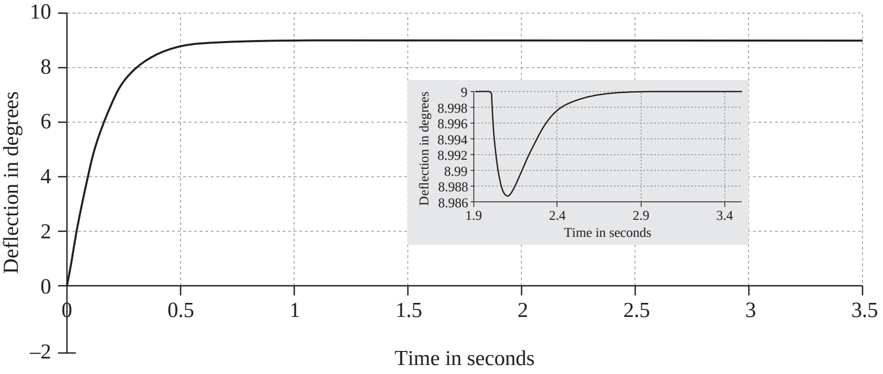

Figure 6.17 Motor failure at low speed [torque summing]

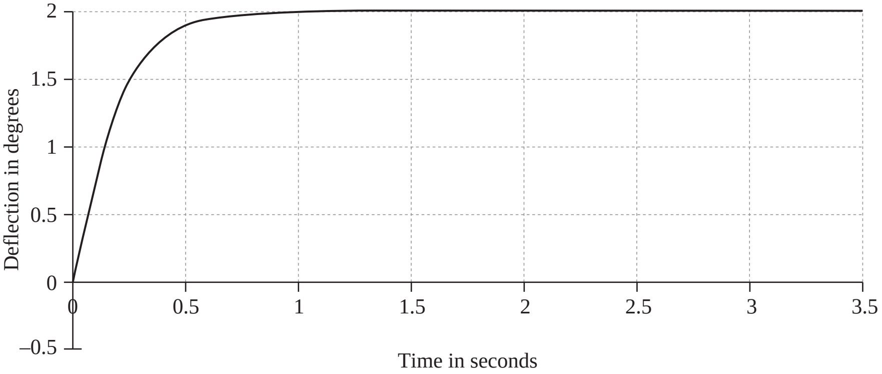

Figure 6.18 Potentiometer failure at high speed [torque summing]

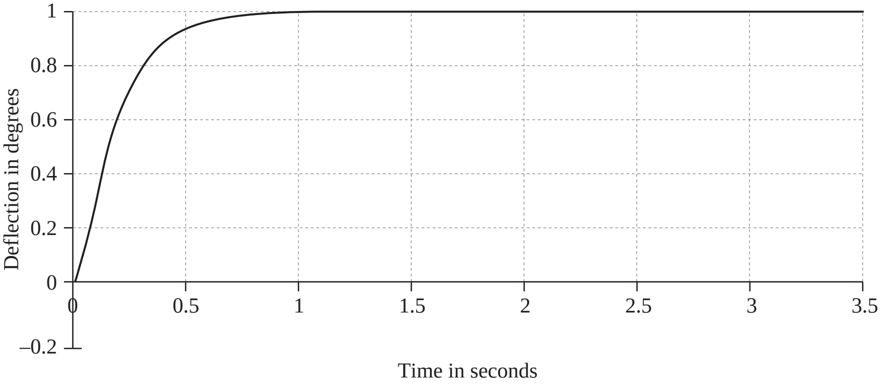

Figure 6.19 Potentiometer failure at high speed [torque summing]

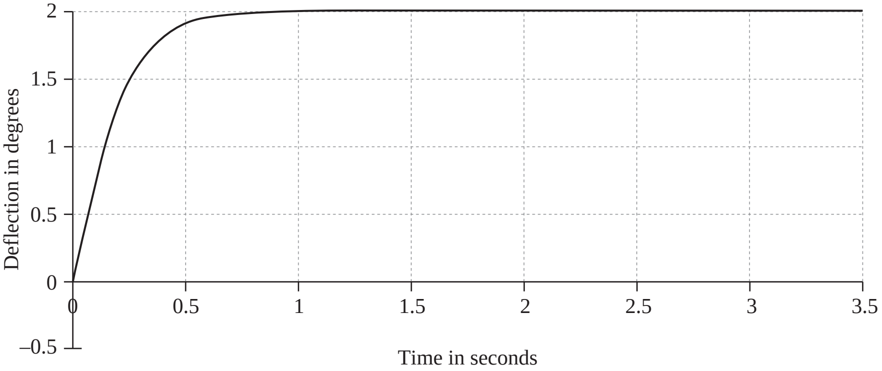

Figure 6.20 Tachometer failure at high speed [torque summing]

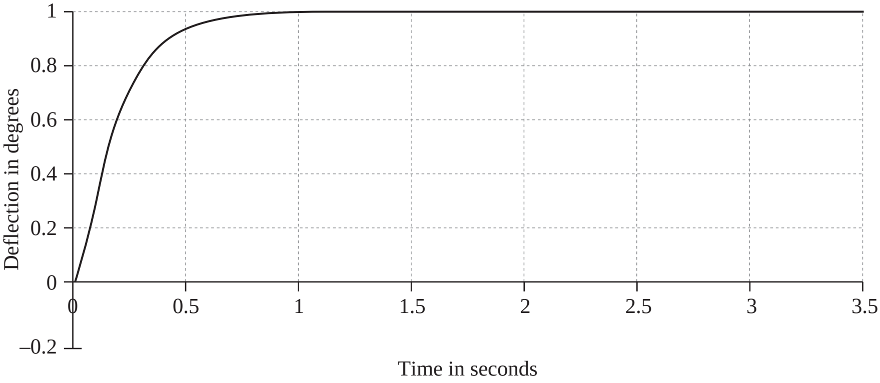

Figure 6.21 Tachometer failure at high speed [torque summing]

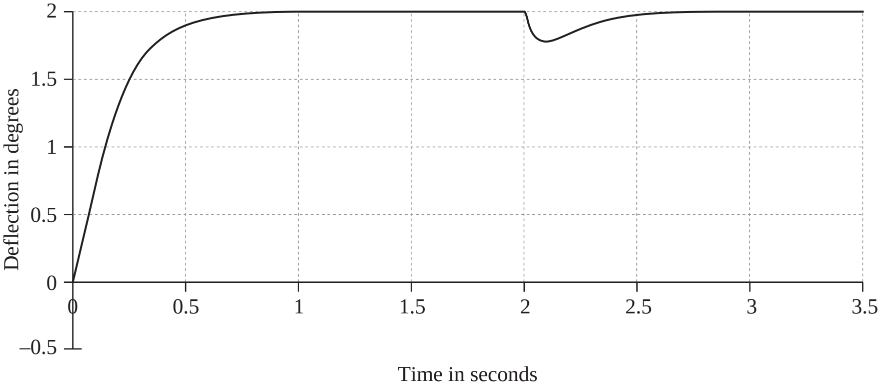

Figure 6.22 Motor failure at high speed [torque summing]

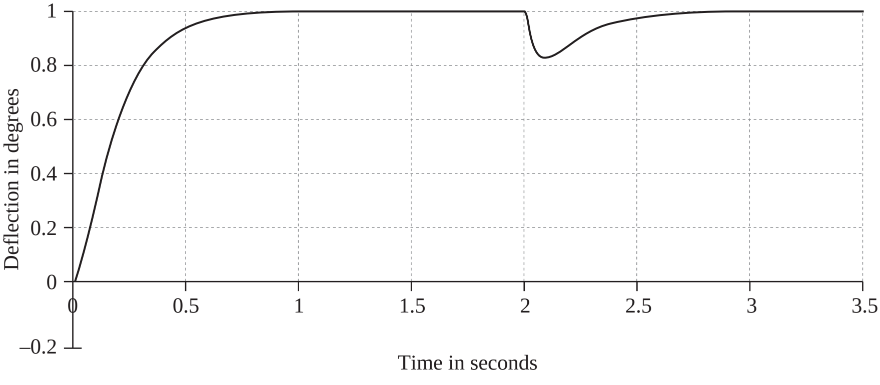

Figure 6.23 Motor failure at high speed [torque summing]

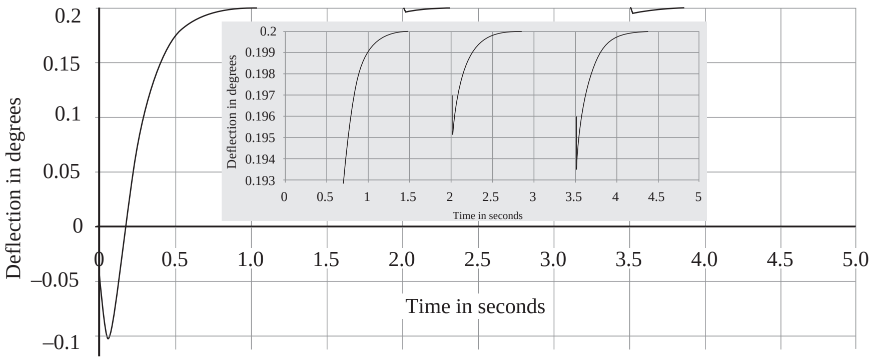

Figure 6.24 Repeated potentiometer failures [torque summing]

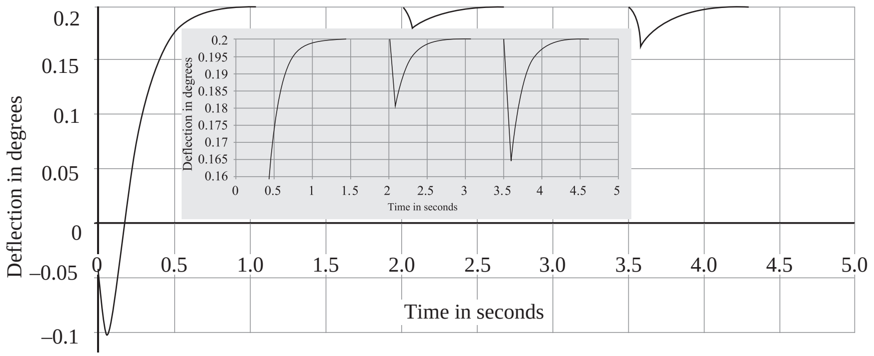

Figure 6.25 Repeated tachometer failures [torque summing]

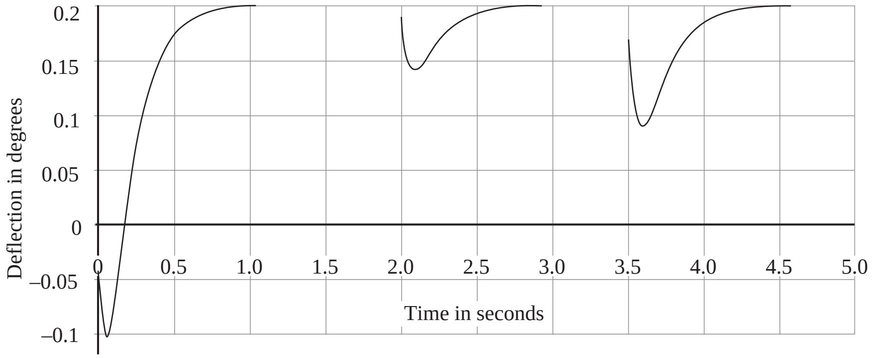

Figure 6.26 Repeated motor failures [torque summing]

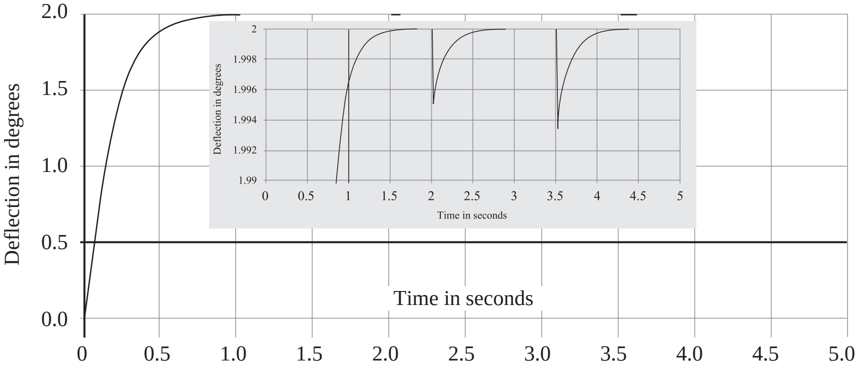

Figure 6.27 Repeated potentiometer failures [torque summing]

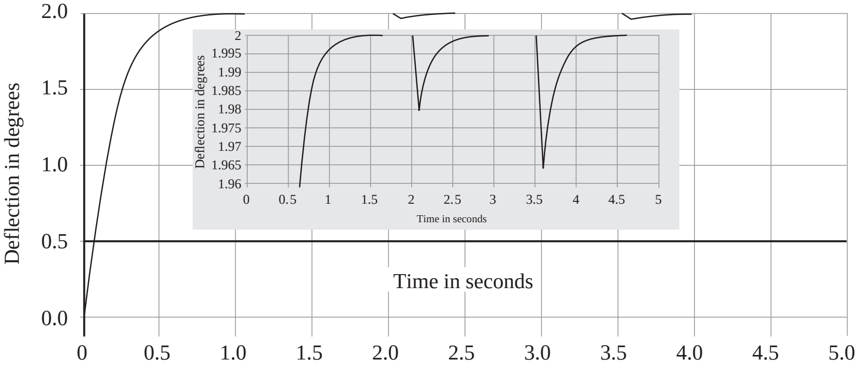

Figure 6.28 Repeated tachometer failures [torque summing]

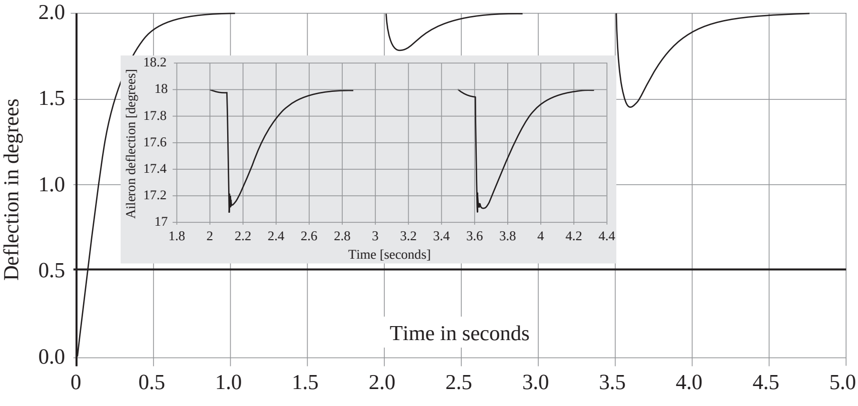

Figure 6.29 Repeated motor failures [torque summing]

Appendix 2

Digital cross monitoring

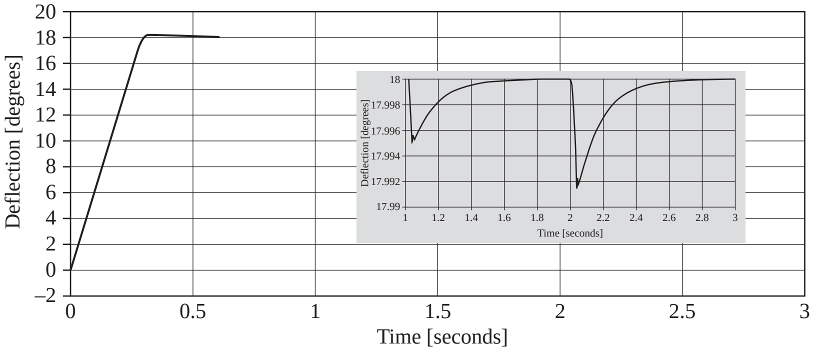

Figure 7.5 Repeated potentiometer failures [low-aircraft speed hardware cross monitoring]

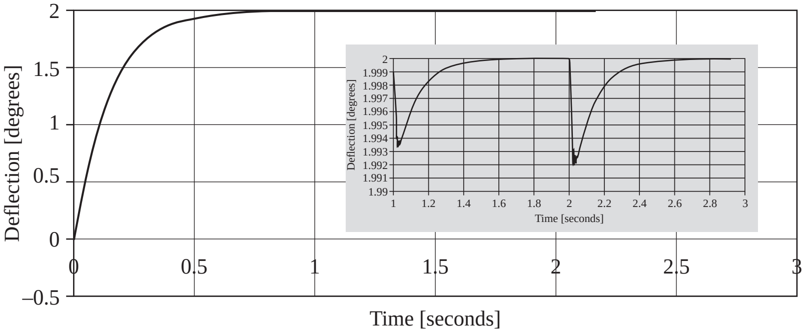

Figure 7.6 Repeated potentiometer failures [high-aircraft speed hardware cross monitoring]

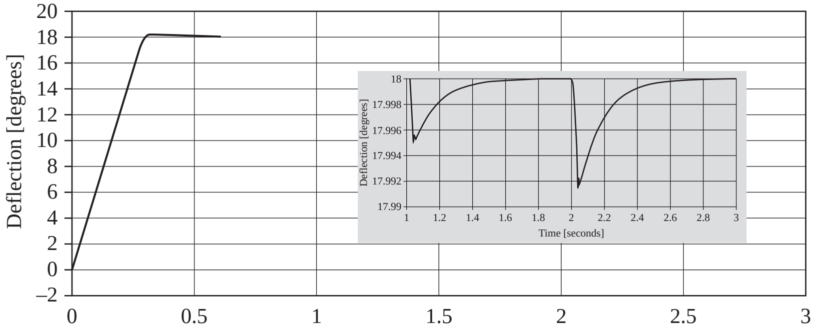

Figure 7.7 *Repeated tachometer failures [low-aircraft speed hardware cross monitoring]*

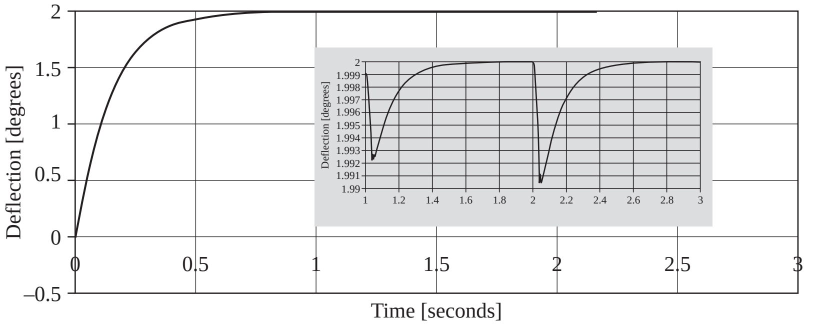

Figure 7.8 *Repeated tachometer failures [high-aircraft speed hardware cross monitoring]*

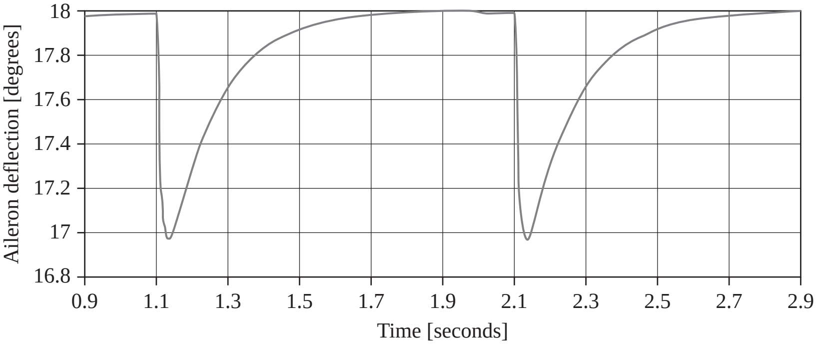

Figure 7.9 *Repeated motor failures [low-aircraft speed hardware cross monitoring]*

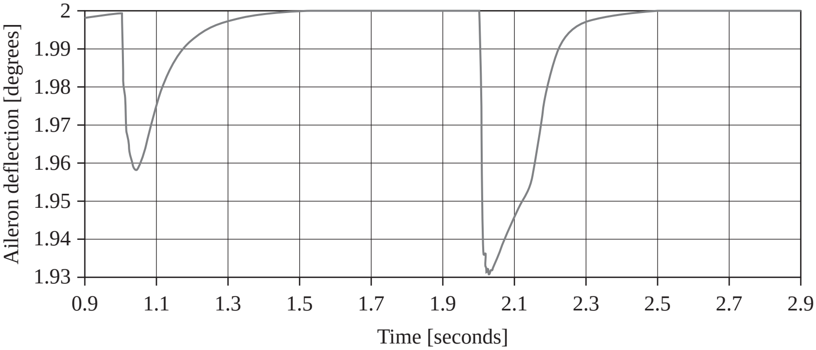

Figure 7.10 *Repeated open-circuit phase motor failures [high-aircraft speed hardware cross monitoring]*

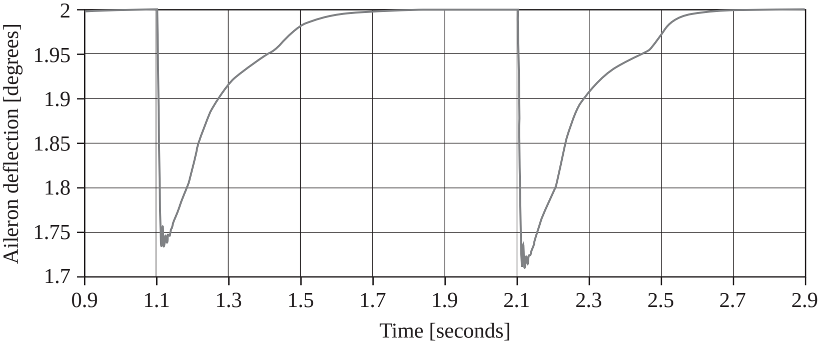

Figure 7.11 *Repeated phase motor (a node is short circuited to zero or supply) failures [high-aircraft speed hardware cross monitoring]*

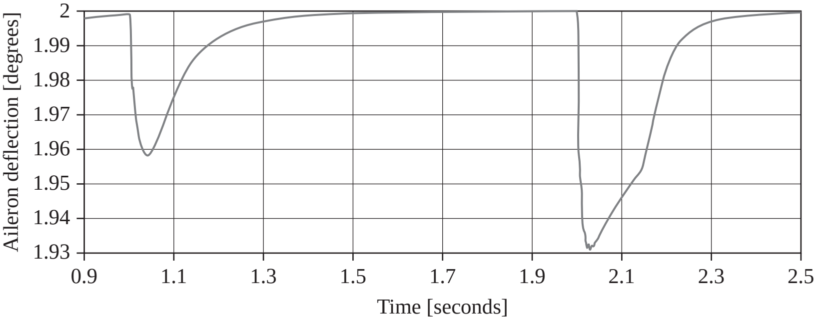

Figure 7.12 *Repeated phase motor (all nodes shorted to supply) failures [high-aircraft speed hardware cross monitoring]*

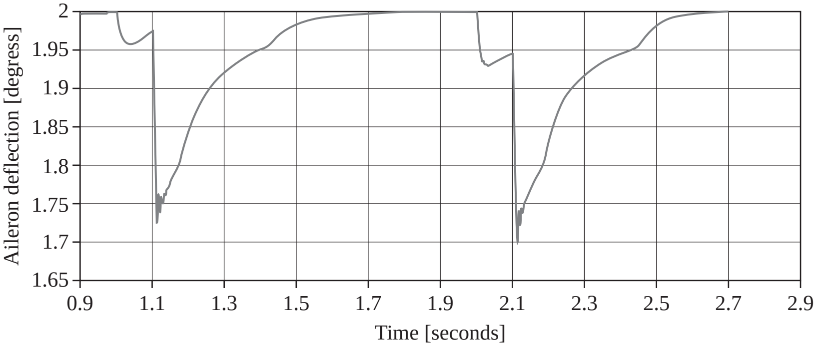

Figure 7.13 Repeated phase motor drives at 6th commutation failures [high-aircraft speed hardware cross monitoring]

References

[1] Hair K.A. 'Electromechanical actuation reliability and survivability'. *NAECON*. 1983, p. 74.

[2] Ward D. 'The all-electric helicopter'. *NAECON*. 1983, p. 104.

[3] Whitaker R., Harmon A., Haynes L. 'A survivable fly-by-wire spoiler actuation system featuring non-flammable fluid, 8000 psi hydraulics and direct drive valves'. *NAECON*. 1985, p. 633.

[4] Holmdahl M. 'Putting all new electric technology development to the test'. *NAECON*. 1983, p. 74.

[5] Leonard J.B. 'A system look at the electromechanical actuation for primary flight control'. *NAECON*. 1983, p. 80.

[6] Thompson K., Eitenmiller K., Hunter L. 'Demonstration of electromechanical actuation technology for military air cargo transport'. *NAECON*. 1983, p. 87.

[7] Thompson K., Alden R., Hunter L. 'Lockheed-Georgia and electric primary flight control systems'. *NAECON*. 1985, p. 588.

[8] Thompson K. 'Notes on the electric control of large aeroplanes'. *NAECON*. 1987, p. 595.

[9] Bradbury G. 'Development of an advanced primary flight control electromechanical actuator'. *NAECON*. 1987, p. 602.

[10] Demerdash N.A., Nehl N.H. 'Dynamic modelling of brushless dc motor-power conditioner unit for electromechanical actuator application'. *IEEE Transaction on Industry Application*. 1979.

[11] Demerdash N.A., Nehl N.H. 'Dynamic modelling of brushless dc motors for aerospace actuation'. *IEEE Transaction on Industry Application*. 1980.

[12] Demerdash N.A., Nehl N.H., Maslowski E. 'Dynamic modelling of brushless dc motors in electric propulsion and electromechanical actuation by digital techniques'. *IEEE Transaction on Industry Application*. 1980.

[13] Pond C.L., Wyllie C.E. 'Test results of a unique high power electric motor actuator designed for space shuttle applications'. *IEEE*. 1983.

[14] Steed D.J. *Dowty* 'Aerospace Wolverhampton, Aerospace Hydraulics and System International Conference'. *Proceedings of the Institute of Mechanical Engineers*, 1993-6, p. 17.

[15] Schaefer W.S., Inderhees L.J., John F. Moynes, 'Moog Incorporated and Northrop Corporation, Aerospace Hydraulics and System International Conference'. *Proceedings of the Institute of Mechanical Engineers*, 1993-6, p. 23.

[16] McCormick M. 'Inland Motors, A primer of brushless dc motors'. *Mechanical Engineering*. February 1988, p. 52.

[17] Electro-craft corporation, USA. *DC Motors Speed Controls Servo Systems, An Engineering Handbook*. Pergamon Press; 1977.

[18] Taft C.K., Gauthier R. 'Brushless motor torque speed curves'. *IMCS*. June 1985.

[19] Taft C.K., Huard S.R. 'Brushless motor torque-curves for open drives'. *IMCS*. June 1988.

[20] Karunadasa J.P., Renfrew A.C. 'Brushless dc motor drive system simulation'. *Proceedings of 25th Universities Power Engineering Conference*, Aberdeen, pp. 17–100, UK; 1993.

[21] Wallace A.K., Spee R. 'The effects of motor parameters on the performance of the brushless dc drives'. *IEEE*. 1987.

[22] Murugesan S. 'An overview of electric motors for space applications'. *IEEE Transaction on Industrial Electronics and Control Instrumentation*. 1981; **IECI-28**(4), November.

[23] Inland Motors, Kollmorgen Corporation, *Brushless dc motors and servo amplifiers*, 1989.

[24] Richards R.J. *An Introduction to Dynamics and Control*. London and New York: Longman Group Ltd.; 1979.

[25] Motorola Semiconductor Technical Data. 'M33035, brushless dc motor controller'. *Technical Literature*, Supplied by Jermyn Distributions.

[26] Ogata K. *Modern Control Engineering*. Prentice-Hall International Editions; 1970.

[27] Miller T.J.E. *Brushless Permanent-Magnet and Reluctance Motor Drives*. Oxford Science Publications; 1989.

[28] Chambers J.M., Cleveland W.S., Kleiner B., Tukey P.A. *Graphical Methods for Data Analysis*. California: Wadsworth International Group, Boston: Duxbury Press; 1983.

[29] Ermakov J.M. 'Monte Carlo methods and related questions'. 1976.

[30] ESDU Engineering Data. *Controls and Flaps, Control-hinge moment*. 5b, August 1989.

[31] Hammersley J.M., Handscomb D.C. *Monte Carlo Methods*. London: Methuen & Co. Ltd. New York: John Wiley & Sons Inc.; 1964.

[32] Kalos M.H., Whitlock P.A. *Monte Carlo Methods*. Vol. 1. John Wiley & Sons Inc.; 1986.

[33] Ross P.J. *Taguchi Techniques for Quality Engineering*. McGraw-Hill Book Company; 1989.

[34] Rubinstein R.Y. *Simulation and the Monte Carlo Method*. John Wiley & Sons Inc.; 1981.

[35] Sage A.P., Melsa J.L. *Estimation Theory with Applications to Communications and Control*. New York: McGraw-Hill Book Company; 1971.

[36] Snell J.L. *Introduction to Probability*. 1st edn. New York: Random House; 1988.

[37] Spiegel M. *Schaum’s Outline Series Theory and Problems of Statistics*. McGraw-Hill Book Company; 1961.

[38] Teper G.L. ‘Aircraft stability and control data, STI Technical Report 176-1’. *Ames Research Center*. April 1969.

[39] Mil-C-18244. ‘Control and stabilisation systems, automatic, piloted aircraft’. 1970.

[40] Mil-F-83300. ‘Flying qualities of piloted VSTOL aircraft’. 1970.

Index

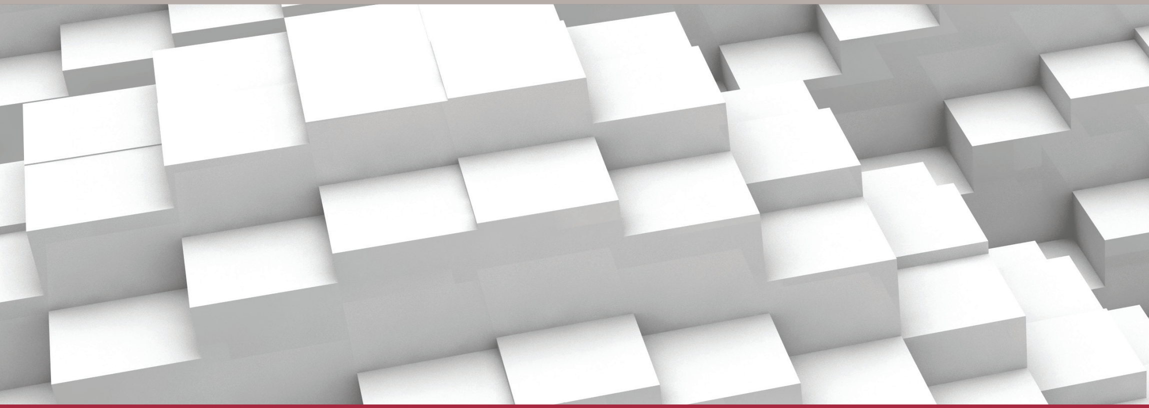

Design and Development of Multi-Lane Smart Electromechanical Actuators

The unavoidable element in the development of flight control systems (to date) has been in hydraulic actuators. This has been the case primarily because of their proven reliability and the lack of alternative technologies. However, the technology to build electromechanically actuated primary flight control systems is now available, which may mark the end of the hydraulic actuation systems - an important step for the development of the future 'all-electric' aircraft.

Design and Development of Multi-Lane Smart Electromechanical Actuators describes design concepts in electromechanical actuators by considering an actuator that has the capability to drive the aerodynamic and inertial loads of an aileron control surface similar to that of the Sea Harrier. It provides the necessary theoretical background to design smart multi-lane electromechanical actuation systems, and provides a general methodology that engineers (electrical, mechanical, mechatronic, aerospace or chemical) will find useful.

Fawaz Yahya Annaz is a Professor at the Electrical Engineering Department, Institute Technology Brunei. He has served as a lecturer in Singapore, a fellow to the Institute of Mechanical Engineering in Japan, and as an Associate professor to the Electrical and Electronic Engineering Department in the University of Fukui, Japan, and the University of Nottingham (Malaysia Campus). His main research interests are development of high integrity systems and robotics.

ISBN 978-1-84919-655-0

9 781849 196550

The Institution of Engineering and Technology
www.theiet.org
978-1-84919-655-0